UNIVERSITY of CALIFORNIA
SANTA CRUZ

A STUDY OF SINGLE AND MULTI-PHOTON EVENTS IN e^+e^- COLLISIONS AT CENTER-OF-MASS ENERGIES OF 161 GEV AND 172 GEV

A dissertation submitted in partial satisfaction of the
requirements for the degree of

DOCTOR OF PHILOSOPHY

in

PHYSICS

by

James H. Dann

June 1998

The dissertation of James H. Dann is approved:

Professor Robert Johnson, Chair

Professor Alan Litke

Professor Michael Dine

Dean of Graduate Studies

Abstract

A STUDY OF SINGLE AND MULTI-PHOTON EVENTS IN $\mathbf{e^+e^\perp}$ COLLISIONS AT CENTER-OF-MASS ENERGIES OF 161 GEV AND 172 GEV

by

James H. Dann

Events from electron-positron collisions where photons are the only particles detected in the final state are studied using the data collected by the ALEPH detector at LEP. The data consist of 11.1 $\mathrm{pb}^{\perp 1}$ at $\sqrt{s}$ = 161 GeV, 1.1 $\mathrm{pb}^{\perp 1}$ at 170 GeV and 9.5 $\mathrm{pb}^{\perp 1}$ at 172 GeV. The $\mathrm{e^+e^\perp} \to \nu\bar{\nu}\gamma(\gamma)$ and $\mathrm{e^+e^\perp} \to \gamma\gamma(\gamma)$ cross sections are measured. The data are in good agreement with predictions based on the Standard Model, and are used to set upper limits on anomalous photon production. Searches for supersymmetric particles in channels with one or more photons and missing energy have been performed. Cross-section upper limits are derived for two different Supersymmetry models. A lower limit of 71 GeV/c^2 at 95% C.L. is set on the mass of the lightest neutralino χ_1^0 ($\mathrm{M}_{\tilde{\mathrm{e}}_\mathrm{R}} = 1.5\mathrm{M}_{\chi_1^0}$ and $\tau_{\chi_1^0} \leq 3$ ns) for the Gauge-Mediated Supersymmetry Breaking model. Constraints on compositeness models and excited electrons are studied using the differential cross section for $\mathrm{e^+e^\perp} \to \gamma\gamma(\gamma)$ events.

Contents

List of Figures

List of Tables

A l'amour de ma vie,

Gabriela Morales,

le bonheur est toujour avec nous.

Acknowledgements

First and foremost I thank my advisor Alan Litke for being a true mentor to me. Without Alan's guidance this work would never have been possible. Although Alan is one of the busiest people I know, he always made as much time as I needed to guide me through my research and, even more impressive, to talk about my future plans. Alan's unending supply of good ideas, constant support and drive to perfection made it a true honor to be his student. I owe Gary Taylor a debt of gratitude I can never repay. Gary answered all of my many questions with clarity and patience. In addition, Gary gave me good advice on the perils inherent in a 400 person collaboration. I especially want to thank Gary for a pep talk he gave me November 1996. Michael Schmitt defended my analysis the first time I presented it. Throughout my last two years in ALEPH Michael was an important contributor of ideas and a big supporter within the collaboration. For all this I thank him.

I thank Robert Johnson for getting me started in ALEPH and for being the chair of my thesis committee. Michael McNeil and Hwi Kim receive my gratitude for their valuable help in the beginning. I thank Simon Black for being a great office mate for four years and for the always interesting physics conversations we had.

Loving thanks goes to my parents, James and Arley Dann, for being the best parents a guy could ever ask for. My brother Michael and sister Rachel were always there for me, especially during the difficult times when I needed someone to talk to. I thank my son Aaron for his patience with me being so far away. Aaron also helped me install my voice recognition software for the first time at CERN.

J'aimerais aussi remercier mon amie Jessica Racordon pour m'enseigner le francias. Sans Cecile, Marc, Jessica, Yvonne et les petits (Dmitri et Lela) mon sejour à Génève et en France auront été incomplète -MERCI! Vous serrez toujour dans mon cœur.

Finally, I thank my future wife Gabriela Morales whose unending support and love carried me through this work. In addition to her patience and understanding, Gabriela deserves credit for her very useful contribution to my thesis. Gabriela generated about 50 Monte Carlo samples and typed probably half of this thesis. On more than one occasion Gabriela came to my rescue by typing in commands on the computer for me so I could generate last minute checks and results the night before a collaboration talk. A toi Gabs, this thesis is dedicated to you.

Chapter 1

Introduction

Two questions have ravaged the curiosity of man since the time of Aristotle. How did we get here? What are we made of?

This thesis will take a few steps forward in the quest to answer these questions at the most fundamental level.

From the point of view of this thesis the question 'How did we get here?' is the question 'How was the universe formed?'. In order to answer this question to the satisfaction of an experimentalist one must recreate the conditions of the very early universe. A hypothesis of how the universe formed is made and then this hypothesis is tested in the laboratory. The experiment either verifies or excludes the hypothesis. Physicists believe the Universe began from a dimensionless point with a tremendous amount of energy and has been expanding at the speed of light ever since (the 'Big Bang Theory' [1, 2]). Answering this grand question will cover thousands, possibly millions, of theses, moreover, recreating the energy present in the very first stages

of the universe may never be possible. However particle accelerators like the LEP accelerator at CERN can create conditions on Earth that have not been seen since well before the first second of the Universe. Studying the data from experiments like ALEPH located in the LEP accelerator can shed light on the very early Universe and on how matter interacts at the particle level. In the study of final states from electron-positron interactions, where photons are the only observed particles, a small contribution is made to the vast pool of knowledge that we hope will someday fully explain how matter interacts at the most fundamental level.

'What are we made of?' is the question 'What are the fundamental building blocks of matter?'. In order to 'see' smaller and smaller objects physicists must go to higher and higher energies. This is obvious through the de Broglie equation $\lambda = h/p \approx h/E$. The smallest object one can see is roughly equal to Planck's constant divided by the energy. The LEP accelerator (with a center-of-mass energy close to 200 GeV) is an ideal place to search for possible substructure contained in currently predicted 'point' particles like the electron.

This thesis describes the study of events from electron-positron collisions where photons are the only particles detected (photon only final states). Through the study of photon only final states at center-of-mass energies 161 and 172 GeV, using the ALEPH experiment at LEP, progress is made in man's quest to understand nature, specifically the two questions presented above.

Utilizing the data obtained from the ALEPH experiment, one can test theoretical models which describe the fundamental laws governing particle interaction. A final

theory describing particle interactions must explain why our universe is composed of matter [3] (as opposed to anti-matter) and how particles obtained mass [4], among many other existing questions. This is because the very early universe (before it cooled enough for atoms to form) was composed solely of particles, many of which we hope are waiting to be discovered. For this reason, a theory describing particle interaction up to a very high energy (for example the Planck Scale at approximately 10^{19} GeV [5, 6]) is desirable not only for understanding the universe around us but also for understanding the origin of our universe. A discovery of new particles supporting current ideas on Supersymmetry, for example, would be an incredible breakthrough and possibly lead to a much deeper understanding of how the universe was formed. Even more intriguing, would be the discovery of the unexpected (events with 10 photons and no charged tracks for example) which would spur new ideas and give greater insight to our universe.

The outline of this chapter is as follows: in Section 1 the current and very successful theory of particle interactions (the Standard Model) is very briefly discussed and a couple of its shortcomings pointed out, in Section 2 two possible extensions to the Standard Model are presented, and in Section 3 concluding remarks and an outline of the remainder of the thesis are given.

1.1 The Standard Model

The Standard Model [7] is possibly the greatest accomplishment of physics in the 20th century. The Standard Model describes the fundamental interactions of nature to an amazing accuracy. The Standard Model predicted the anomalous magnetic moment of the electron correctly to six decimal places. The $W^{\pm}$ and Z boson particles were predicted by the Standard Model and subsequently found.

Of particular interest to this thesis, the Standard Model successfully predicts the cross section for electron-positron collisions which produce events where photons and nothing else is detected. Even more amazing the Standard Model predicts with what energies and at what angles these photons will be produced. For example, at LEP a bunch of electrons are revved up close to the speed of light and are collided into a bunch of positrons (the anti-particle of the electron) also going close to the speed of light. The electron and positron bunches are collided together many times. The Standard Model predicts (on a percentage basis) how often two photons with a certain energy and angle will be produced from these collisions. The Standard Model is truly an exceptional accomplishment.

Photon only final states in $e^{+}e^{\perp}$ collisions can be divided into two classes: events produced through the Electro-Weak interaction and events produced through the Quantum Electrodynamics interaction.

1.1.1 The Electro-Weak Process $e^+e^- \to \nu\bar{\nu}\gamma(\gamma)$

Photonic events from the Electro-Weak interaction of neutrino production accompanied by a bremsstrahlung photon(s) (here after referred to as 'EW events') are the photon events produced through the Feynman diagrams in Figure 1.1. The EW events are simply neutrino, anti-neutrino production with a bremsstrahlung photon. The EW events necessarily have missing energy carried off by the undetected neutrinos (neutrinos interact weakly with matter and therefore cannot be detected except with specially designed experiments). The s-channel Z diagrams easily dominate over the $W^{\pm}$ exchange diagrams for photon energy above 5 GeV.

The EW events are the only measure of the neutrino-anti-neutrino cross section in $e^+e^{\perp}$ collisions above the Z resonance. That is, the only measure of the $e^+e^{\perp} \to \nu\bar{\nu}$ production rate at the never before studied high energies of LEP2 is through the study of events with a bremsstrahlung photon(s) and nothing else detected (with appropriate selection criteria and if no new physics manifests itself, the 'nothing else detected' are the neutrinos). This method of studying neutrinos was first proposed by Ma and Okada in 1978 [8], and called the 'neutrino counting experiment'. In addition, the accurate measurement of the neutrino cross section is a nice existence proof that one can 'see' invisible matter (i.e. weakly interacting matter) through a bremsstrahlung photon. Thus, the neutrino cross-section measurement validates the method of searching for invisible matter using a bremsstrahlung photon.

The missing mass for EW events is expected to peak at the Z mass due to the Z

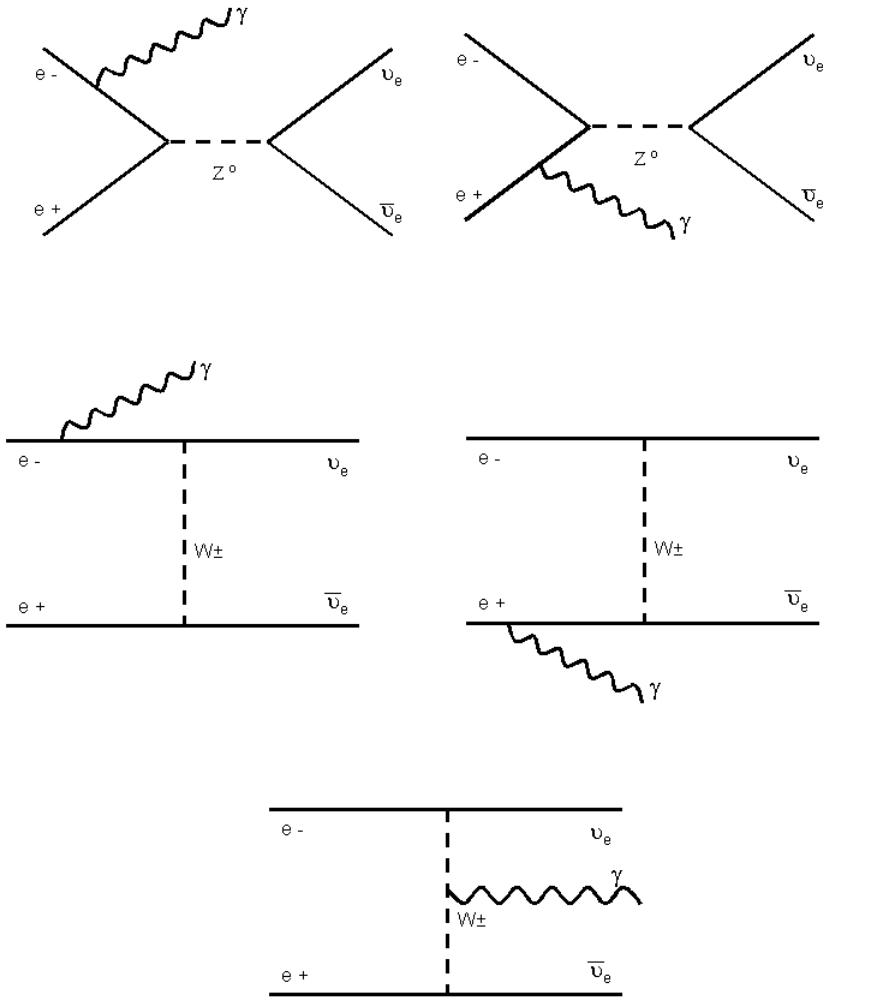

Figure 1.1: *The Feynman diagrams for the EW process.*

boson resonance. The missing mass for one-photon events is

$$\mathrm{M}_{Missing} = \sqrt{s - 2\sqrt{s}E_\gamma}, \tag{1.1}$$

where $\sqrt{s}$ is the center-of-mass energy and E_γ is the photon energy in the lab frame. Note that studying the missing mass distribution of one-photon events is equivalent to studying the photon energy distribution. The missing mass distribution is also expected to peak at high masses due to the favorable cross section for low-energy bremsstrahlung photons.

1.1.2 The Quantum Electrodynamics Process $e^+e^- \to \gamma\gamma(\gamma)$

Photonic events from the Quantum Electrodynamics process (QED events) are electron-positron annihilation into two photons. The lowest order Feynman diagrams for these events are shown in Figure 1.2. The electron and positron annihilate via

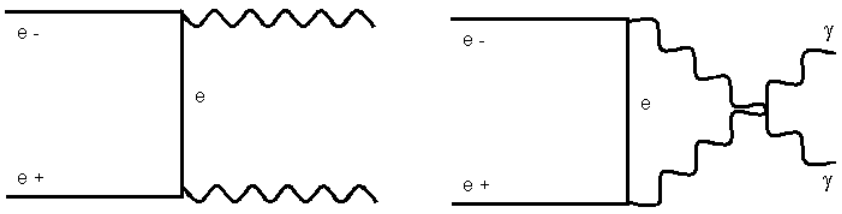

Figure 1.2: *The Feynman diagrams for the QED process.*

t-channel electron exchange producing a photon pair. In the absence of initial state radiation, energy and momentum conservation dictates that the photons share equally

the energy of the composite electron-positron pair. Therefore, the lowest order (Born level) process $e^+e^\perp \to \gamma\gamma$ produces two back-to-back photons with the beam energy. The Born level differential cross section is easily calculated and given by:

$$\left(\frac{d\sigma}{d\Omega}\right)_{Born} = \frac{\alpha^2}{s}\left(\frac{1+\cos^2\theta}{1-\cos^2\theta}\right) \tag{1.2}$$

where α is the fine structure constant, $\sqrt{s}$ is the center-of-mass energy, and the assumption that the electron mass is much less than the beam energy has been made. The cross section decreases as the center-of-mass energy is increased.

The $e^+e^\perp \to \gamma\gamma$ events are the only pure QED reaction at LEP; that is the Electroweak corrections to the cross section calculation are negligible. Because LEP is exploring energies never before studied by man it is very important to study these QED events in order to verify if the production rate and angular distribution agree with the Standard Model predictions for QED. Although Quantum Electodynamics is a well-tested theory, one never knows what is lurking behind the next energy frontier.

1.2 The Search for New Physics

The Standard Model works almost to perfection at presently studied energies but it is an 'effective theory'; the Standard Model does not explain how it arrived at its present state from the initial singularity in our past associated with the Big Bang. In addition, there are some outstanding problems to the Standard Model for which we have no acceptable solutions. One example is the Higgs mass. The Higgs particle is predicted to be responsible for giving mass to particles. However, a

straightforward calculation using the Standard Model (without any well-chosen fine tuning) of radiative corrections to the Higgs mass produces a result of infinity. This is called the naturalness problem. Furthermore the Standard Model does not predict the mass values of the fermions, the quark mixing angles or the characteristics of the mass spectrum such as why leptons are lighter than quarks in each generation.

The Standard Model works too well to be 'wrong'. The probable answer to these questions and many others lie in an extension to the Standard Model. Just as quantum mechanics extends Newtonian mechanics to the particle level, particle physicists believe there is a theory that extends the Standard Model to higher energies. And nested inside this theory will be the answer to many unexplained observations. An attractive model that extends the Standard Model to higher energies is Supersymmetry. Another model, called compositeness, assumes that the elementary particles like the electron have a deeper underlying structure waiting to be discovered.

1.2.1 Supersymmetry

An elegant extension to the Standard Model is a theory called Supersymmetry [9]. Supersymmetry postulates that there is a symmetry between bosonic and fermionic matter. This implies that every particle has a partner which is exactly the same in charge and in how it interacts with matter but differs in spin by one half an integer as shown in Table 1.1.

So, the super-partners of spin 1/2 fermions are spin 0 particles and the super-partners of spin 1 bosons are spin 1/2 particles. For example, the photon's super-

Quarks(spin $\frac{1}{2}$)			Squarks(spin 0)			
$\begin{pmatrix} u \\ d \end{pmatrix}_{\rm L}$	$u_{\rm R}$	$d_{\rm R}$	$\begin{pmatrix} \tilde{u} \\ \tilde{d} \end{pmatrix}_{\rm L}$	$\tilde{u}_{\rm R}$	$\tilde{d}_{\rm R}$	
$\begin{pmatrix} c \\ s \end{pmatrix}_{\rm L}$	$c_{\rm R}$	$s_{\rm R}$	$\begin{pmatrix} \tilde{c} \\ \tilde{s} \end{pmatrix}_{\rm L}$	$\tilde{c}_{\rm R}$	$\tilde{s}_{\rm R}$	
$\begin{pmatrix} t \\ b \end{pmatrix}_{\rm L}$	$t_{\rm R}$	$b_{\rm R}$	$\begin{pmatrix} \tilde{t} \\ \tilde{b} \end{pmatrix}_{\rm L}$	$\tilde{t}_{\rm R}$	$\tilde{b}_{\rm R}$	$\rightarrow \tilde{t}_{1,2}$, $\tilde{b}_{1,2}$
Leptons(spin $\frac{1}{2}$)			Sleptons(spin 0)			
$\begin{pmatrix} e \\ \nu_e \end{pmatrix}_{\rm L}$	$e_{\rm R}$		$\begin{pmatrix} \tilde{e} \\ \tilde{\nu}_e \end{pmatrix}_{\rm L}$	$\tilde{e}_{\rm R}$		
$\begin{pmatrix} \mu \\ \nu_\mu \end{pmatrix}_{\rm L}$	$\mu_{\rm R}$		$\begin{pmatrix} \tilde{\mu} \\ \tilde{\nu}_\mu \end{pmatrix}_{\rm L}$	$\tilde{\mu}_{\rm R}$		
$\begin{pmatrix} \tau \\ \nu_\tau \end{pmatrix}_{\rm L}$	$\tau_{\rm R}$		$\begin{pmatrix} \tilde{\tau} \\ \tilde{\nu}_\tau \end{pmatrix}_{\rm L}$	$\tilde{\tau}_{\rm R}$		$\rightarrow \tilde{\tau}_{1,2}$
Gauge bosons(spin 1)			Gauginos (spin $\frac{1}{2}$)			
g			$\tilde{g}$			
γ			$\tilde{\gamma}$			$\tilde{\gamma}$,$\tilde{Z}$,$\tilde{H}^0_{1,2}$
Z			$\tilde{Z}$			$\rightarrow \chi^0_{1,2,3,4}$
$W^\pm$			$\tilde{W}^\pm$			(Neutralinos)
Higgs bosons(spin 0)			Higgsinos(spin $\frac{1}{2}$)			$\tilde{W}^\pm$,$\tilde{H}^\pm$
						$\rightarrow \chi^\pm_{1,2}$
h, H, A			$\tilde{H}^0_{1,2}$			(Charginos)
$H^\pm$			$\tilde{H}^\pm$			

Table 1.1: *The fundamental particles of the Standard Model are listed on the left and their predicted supersymmetric partners are listed on the right. The arrows indicates fields that mix and the corresponding physical fields that result.*

partner is called a photino and has spin 1/2. The nomenclature for all these additional particles goes as follows. The spin 0 super-partners of fermions are simply the fermion name with an 's' at the beginning so the super-partner of the electron is called the selectron. The names of the spin 1/2 super-partners of the bosons are made by attaching an '-ino' at the end. So the photino is the super-partner of the photon.

The fermions with mass like electrons have two helicity states due to their spin 1/2 nature. The electron super-partners denoted 'selectrons' preserve both helicity states. So that there are actually two super-partners for the electron, the right-handed selectron and the left-handed selectron, one for each helicity state . This is generally true for all 'sfermions' (super-partners of fermions).

As if it isn't confusing enough the boson super-partners can mix. So that the super-partners of bosons are really a mixture of supersymmetric spin 1/2 particles. For example, a boson super-partner could be a mixture of the photino and zino. In order to simplify things (finally!), the neutral boson super-partners (the spin 1/2 supersymmetric particles) are called simply 'neutralinos' (denoted χ^0) and the charged super-partners of the bosons are called 'charginos' (denoted $\chi^{\pm}$). They are ordered according to their mass (χ_1^0 being the lightest neutral spin 1/2 super-partner, χ_2^0 being second lightest, and so on). Table 1.1 summarizes the above three paragraphs.

In R conserving Supersymmetry (the only kind considered in this thesis) the number of supersymmetric particles is conserved in an interaction. This is analogous to fermionic number conservation where the decay of the muon into an electron is accompanied by a muon neutrino and an anti-electron neutrino in order to conserve

electron and muon numbers. Consequently, a supersymmetric particle can never decay into two ordinary particles, and, thus, the lightest supersymmetric particle (LSP) is always stable. This leads to a distinct topology in the detector for a supersymmetric event. The production of the lightest supersymmetric particles is seen in the detector as either a heavy charged particle leaving the detector (if χ_1^+ or $\tilde{e}$ is the lightest supersymmetric particle) or missing energy (if χ_1^0 or $\tilde{\nu}$ is the lightest supersymmetric particle where the χ_1^0 or $\tilde{\nu}$ escape undetected).

In the study of photon only final states we are searching for the production of neutral supersymmetric particles. Due to the lack of discovery at lower energy colliders [10, 11] the realm of supersymmetric particles is presumed to be at high mass. Thus, as LEP2 marches up in energy we are constantly searching for the first direct signs of Supersymmetry through the production of the lightest supersymmetric particles. The nature of the lightest supersymmetric particles and their decay modes is the subject of vast theoretical work [9].

1.2.2 The Neutralino LSP Scenario

One possibility discussed in this thesis is the scenario where χ_2^0 is the second lightest supersymmetric particle (NLSP), the χ_1^0 is the LSP and the decay $\chi_2^0 \to \chi_1^0\gamma$ has a 100% Branching Ratio. In this scenario χ_2^0 is pure photino and χ_1^0 is pure higgsino (i.e. no mixing) [1]. This scenario is one of many theoretical possibilities.

[1] A pure higgsino χ_2^0 and a pure photino χ_1^0 also has a 100% Branching Ratio for the decay $\chi_2^0 \to \chi_1^0\gamma$, however the cross section for $e^+e^\perp \to \chi_2^0\chi_2^0$ is significant only in the pure photino χ_2^0 scenario.

However, it is motivated by an unusual event recorded by the CDF collaboration at Fermi lab [27]. The CDF event is discussed in Section 1.2.3.

In this scenario, Supersymmetry is searched for at LEP via the production channel $e^+e^\perp \to \chi_2^0\chi_2^0$ followed by the decays $\chi_2^0 \to \chi_1^0\gamma$. The Feynman diagrams for $e^+e^\perp \to \chi_2^0\chi_2^0$ are given in Figure 1.3. The cross section for $e^+e^\perp \to \chi_2^0\chi_2^0$ where χ_2^0 is

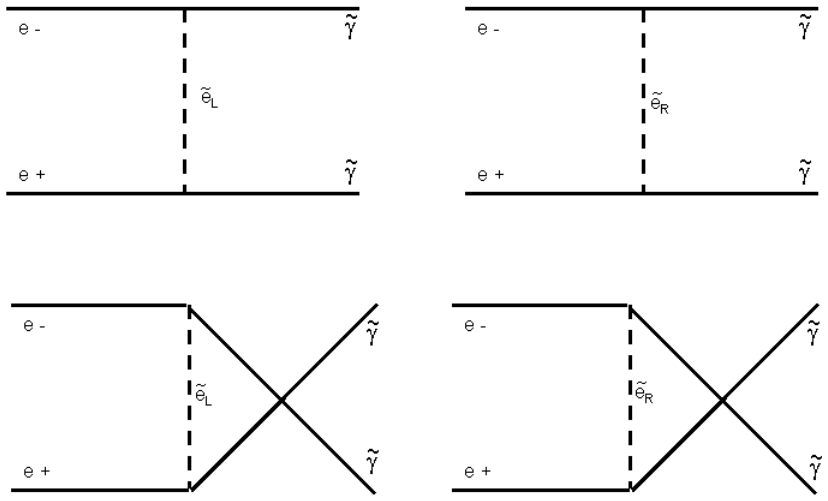

Figure 1.3: *The Feynman diagrams for the* $e^+e^\perp \to \chi_2^0\chi_2^0$ *process, where the* χ_2^0 *is pure photino and denoted as such.*

pure photino (and denoted as $\tilde{\gamma}$) is given by [13]:

$$\left(\frac{d\sigma}{d\Omega}\right) = \frac{\alpha^2 s\beta^3}{4}\left(\frac{(\Delta M^2 + \frac{1}{2}s)^2(1+\cos^2\theta) - s(2(\Delta M^2 + \frac{1}{2}s) - M_{\tilde{\gamma}}^2 - \frac{1}{4}s)\cos^2\theta + \frac{1}{4}s^2\beta^2\cos^4\theta}{[(\Delta M^2 + \frac{1}{2}s)^2 - \frac{1}{4}s^2\beta^2\cos^2\theta]^2}\right) \tag{1.3}$$

where θ is the polar angle, $\Delta M^2 \equiv M_{\tilde{e}_R}^2 - M_{\tilde{\gamma}}^2$ and $\beta = (1 - 4M_{\tilde{\gamma}}^2/s)^{1/2}$. In the above equation $M_{\tilde{e}_R} = M_{\tilde{e}_L}$ and the approximation $M_e = 0$ has been made to simplify the

cross section. As can be seen from the formula, the cross section depends on $\sqrt{s}$ and the χ_2^0 and selectron masses. For $M_e = 0$ the cross section is an incoherent sum of the $\tilde{e}_R$ and $\tilde{e}_L$ diagrams, so if we take $M_{\tilde{e}_L} \gg M_{\tilde{e}_R}$ the cross section is reduced by a factor of two. For a χ_2^0 mass of 65 GeV/c^2, $\tilde{e}_R$ and $\tilde{e}_L$ masses of 100 GeV/c^2 and $\sqrt{s} = 161\,\text{GeV}$ (172 GeV) the cross section is 0.37 pb (0.49 pb).

The topology of events from $e^+e^\perp \to \chi_2^0\chi_2^0 \to \chi_1^0\chi_1^0\gamma\gamma$ is two acoplanar photons (i.e. two photons and missing transverse energy). The acoplanarity angle is defined as follows: draw a plane perpendicular to the beam axis; the angle between the projections of the photon momentum vectors in this plane is the acoplanarity angle. This plane is defined in ALEPH coordinates as the x-y plane. It is understood that acoplanar photons are two photons that have acoplanarity less than 180° (i.e. photons that are not back-to-back in the x-y plane). Since transverse energy is defined as the energy perpendicular to the beam axis, acoplanar photons do not balance transverse energy and, thus, there is missing transverse energy in the event (assumed to be carried off by undetected weakly interacting particles). The range of the photon energy is given by:

$$E_{low} < E_\gamma < E_{high} \tag{1.4}$$

where

$$E_{low} = \frac{1-\beta}{\sqrt{1-\beta^2}} \frac{M_{\chi_2^0}^2 - M_{\chi_1^0}^2}{2M_{\chi_2^0}} \tag{1.5}$$

and

$$E_{high} = \frac{1+\beta}{\sqrt{1-\beta^2}} \frac{M^2_{\chi^0_2} - M^2_{\chi^0_1}}{2M_{\chi^0_2}}. \tag{1.6}$$

with

$$\beta = \sqrt{1 - \frac{4M^2_{\chi^0_2}}{s}}; \tag{1.7}$$

β is the velocity of χ^0_2 in the lab frame. In the energy equations 1.5 and 1.6 the second term is the energy of the photon in the χ^0_2 center-of-mass frame and the first term is the boost from the center-of-mass frame to the lab frame. The range of photon energy is simply obtained from the kinematics of the event for an isotropic decay $\chi^0_2 \to \chi^0_1\gamma$.

Unlike the EW events both photons carry significant energy, and unlike the QED events there is necessarily missing energy in the event. In addition, the $|\cos\theta|$ distribution for the photons is very close to isotropic [2], whereas photons from the EW and QED processes peak strongly at high $|\cos\theta|$. Both the energy information and angular information will be used to separate the EW and QED photon events from possible signs of Supersymmetry.

The production $e^+e^\perp \to \chi^0_1\chi^0_1$ is of course the first accessible mode, but this process is effectively invisible as the neutralinos escape undetected. This process can be seen through the bremsstrahlung photon (i.e. $e^+e^\perp \to \chi^0_1\chi^0_1\gamma$) but then the cross section is reduced by an order α and therefore becomes much more difficult experimentally. Given the luminosity from the 1996 run, if the cross section for $e^+e^\perp \to \chi^0_1\chi^0_1$ is extremely high (greater than 100 pb) the process $e^+e^\perp \to \chi^0_1\chi^0_1\gamma$ would be seen as an

[2] The decay $\chi^0_2 \to \chi^0_1\gamma$ is isotropic and the production angle of the χ^0_2 (given by equation 1.3) is not severely peaked. Thus, the polar angle for the photons in the laboratory reference frame have a distribution very close to isotropic.

excess in the high mass region of the photon missing mass distribution (discussed in Chapter 3). Note that this is equivalent to saying that an excess would be seen in the low energy region of the photon energy distribution.

The process $e^+e^\perp \to \chi_2^0\chi_1^0$ would also seem preferable to $e^+e^\perp \to \chi_2^0\chi_2^0$. However, when the neutralino composition is pure photino for the χ_2^0 and pure higgsino for the χ_1^0 (giving a 100% Branching Ratio) the cross section for this process is predicted to be extremely low [3]. Nevertheless, this type of process is searched for by studying the one-photon events (for which there is a large background of EW events). The decay kinematics for $\chi_2^0 \to \chi_1^0\gamma$ and the velocity of χ_2^0 in the lab frame determine the photon energy. The photon energy range for $e^+e^\perp \to \chi_2^0\chi_1^0 \to \chi_1^0\chi_1^0\gamma$ can be written in exactly the same manner as for a photon coming from $e^+e^\perp \to \chi_2^0\chi_2^0 \to \chi_1^0\chi_1^0\gamma\gamma$ given by equations (1.4 - 1.6). However in this scenario two different mass particles are produced, thus the velocity β of χ_2^0 is a more complicated function, given by:

$$\beta = \sqrt{\frac{p^2}{p^2 + M^2_{\chi_2^0}}} \tag{1.8}$$

with

$$p = \frac{1}{2\sqrt{s}}\sqrt{s^2 - 2s(M^2_{\chi_2^0} + M^2_{\chi_1^0}) + (M^2_{\chi_2^0} - M^2_{\chi_1^0})^2}. \tag{1.9}$$

The dominant Feynman diagrams are shown in Figure 1.4.

[3] There is a very specific scenario when the process $e^+e^\perp \to \chi_2^0\chi_1^0$ is predicted to be accessible at LEP2. If a mass difference between χ_2^0 and χ_1^0 is small enough (~ 5 GeV) the Branching Ratio for $\chi_2^0 \to \chi_1^0\gamma$ is large for most neutralino compositions [14] due to phase space suppression of the other decay modes. If in addition χ_2^0 and χ_1^0 are light enough there would be a sufficient boost on the photon energy to have reasonable detection efficiency. In this scenario the cross section multiplied by Branching Ratio can be larger for $e^+e^\perp \to \chi_2^0\chi_1^0 \to \chi_1^0\chi_1^0\gamma$ than for $e^+e^\perp \to \chi_2^0\chi_2^0 \to \chi_1^0\chi_1^0\gamma\gamma$.

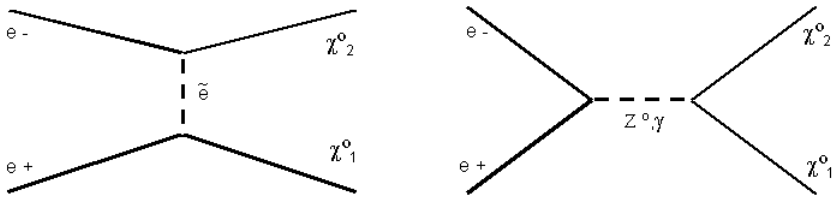

Figure 1.4: *The dominant Feynman diagrams for the* $e^+e^\perp \to \chi_2^0\chi_1^0$ *process.*

1.2.3 Gauge-Mediated Supersymmetry Breaking and the Gravitino LSP Scenario

Gauge-Mediated Supersymmetry Breaking (GMSB) [15, 16, 17, 18, 19, 20] is a version of Supersymmetry where the gravitino (denoted as $\tilde{G}$), the super-partner of the graviton, is the LSP [4]. In the minimal model of GMSB (the only model of GMSB considered in this thesis), the χ_1^0 is the NLSP [5] and the decay $\chi_1^0 \to \tilde{\mathrm{G}}\gamma$ is isotropic [19] with a 100% Branching Ratio. The gravitino $\tilde{G}$ is essentially massless ($\mathrm{M}_{\tilde{G}} < 1\,\mathrm{MeV}/c^2$) and neutral. The process $e^+e^\perp \to \chi_1^0\chi_1^0 \to \tilde{\mathrm{G}}\tilde{\mathrm{G}}\gamma\gamma$ is seen in the detector as two photons and missing energy. In GMSB, the χ_1^0 is almost pure 'B-ino' [19], the super-partner of the isosinglet intermediate vector Boson from the $U(1)$ part of the Electroweak $SU(2)_L \otimes U(1)$ symmetry. A pure 'B-ino' χ_1^0 can be thought

[4] The graviton is the theorized particle that transmits the force of gravity. The gravitational interaction is too weak to be detected at the particle level so the graviton has never been observed experimentally.

[5] In the scenario of very large $\tan\beta$, where β is the ratio of Higgs vacuum expectation values, the $\tilde{\tau}$ is slightly lighter in mass than the χ_1^0.

of as a specific mixture of photino and zino components. Similar to the production of photinos in the previous section, the production of pure B-ino χ_1^0's in $e^+e^\perp \to \chi_1^0\chi_1^0$ proceeds via selectron exchange. However, for $e^+e^\perp \to \chi_1^0\chi_1^0$ where the neutralino χ_1^0 is pure B-ino, right-selectron exchange dominates over left-selecton exchange. The difference is that, unlike the photino, the B-ino couples to hypercharge.

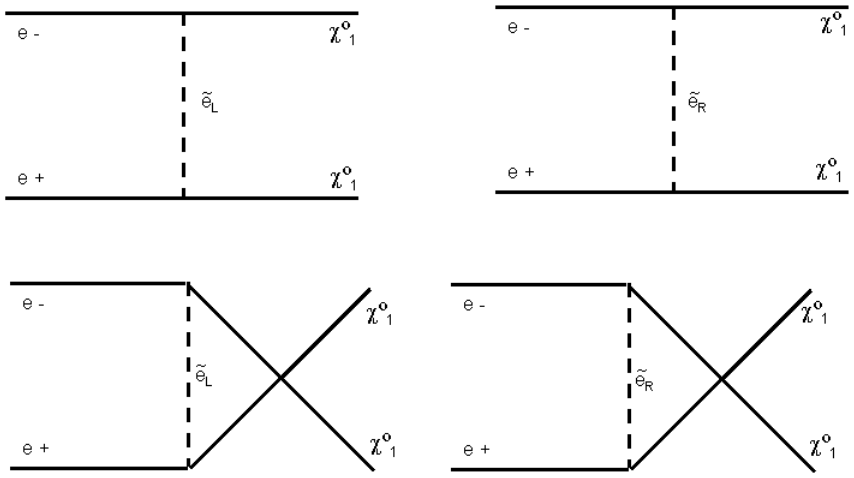

Figure 1.5: *The Feynman diagrams for the* $e^+e^\perp \to \chi_1^0\chi_1^0$ *process.*

The Feynman diagrams are given in Figure 1.5 and the differential cross section is given by [21]

$$\frac{d\sigma}{d\cos\theta} = \sum_{i=\tilde{e}_R,\tilde{e}_L} \frac{\beta^3}{s}\frac{\pi\alpha^2 Y_i^4}{2\cos^4\theta_W}\left(\frac{1-\cos^2\theta}{(1+z_i)^2-\beta^2\cos^2\theta} + \frac{2z_i^2\cos^2\theta}{((1+z_i)^2-\beta^2\cos^2\theta)^2}\right) \tag{1.10}$$

where β is the B-ino velocity in the lab frame, $z_i = 2(M_i^2 - M_{\tilde{B}}^2)/s$, and $Y_{\tilde{eR}} = 2$, $Y_{\tilde{eL}} = -1$ are the hypercharge of the right and left selectrons. Because the hypercharge is

to the fourth power, it is clear that the left-selectron contribution to the cross section is down a factor of 16 from that of the right selectron, given equal selectron masses.

The process $e^+e^\perp \to \chi_1^0\chi_1^0 \to \tilde{G}\tilde{G}\gamma\gamma$ is very similar to $e^+e^\perp \to \chi_2^0\chi_2^0 \to \chi_1^0\chi_1^0\gamma\gamma$ except that all the final decay particles are massless in the former. The mass of the gravitino is expected to be less than $1\,\mathrm{MeV}/c^2$. This mass value is 5 orders of magnitude smaller than the center-of-mass energy. Assuming the gravitino mass to be zero has negligible effect on its energy distribution. The photon energies are given by equations (1.4 - 1.6) if one simply substitutes χ_1^0 for χ_2^0 and $\tilde{G}$ for χ_1^0 and then take the gravitino mass to zero. The photon energy range for $e^+e^\perp \to \chi_1^0\chi_1^0 \to \tilde{G}\tilde{G}\gamma\gamma$ is given by

$$E_{low} < E_\gamma < E_{high} \tag{1.11}$$

where

$$E_{low} = \frac{1-\beta}{\sqrt{1-\beta^2}}\frac{M_{\chi_1^0}}{2} \tag{1.12}$$

and

$$E_{high} = \frac{1+\beta}{\sqrt{1-\beta^2}}\frac{M_{\chi_1^0}}{2}. \tag{1.13}$$

where

$$\beta = \sqrt{1-\frac{4M_{\chi_1^0}^2}{s}}. \tag{1.14}$$

In Gauge-Mediated Supersymmetry Breaking models the neutralino can have a non-negligible lifetime. This could lead to the striking topology of acoplanar photons that do not originate from the interaction region. The neutralino lifetime directly

depends on the Supersymmetry breaking scale $\sqrt{F}$ and the mass of the neutralino $M_{\chi_1^0}$ and is given by [18]:

$$c\tau \simeq 130 \left(\frac{100\,\mathrm{GeV}}{M_{\chi_1^0}}\right)^5 \left(\frac{\sqrt{F}}{100\,\mathrm{TeV}}\right)^4 \mu\mathrm{m}. \tag{1.15}$$

Therefore a discovery of the χ_1^0 with measurable lifetime and a measurement of its mass would lead to the determination of the energy scale at which Supersymmetry is broken. In the less fortunate scenario where no discovery is made we can still set a lower limit on the Supersymmetry breaking scale as a function of neutralino mass. The Supersymmetry breaking scale is predicted to be in the range of 10^2 to 10^4 TeV [17]. The sensitivity of this experiment on $\sqrt{F}$ for the given luminosity of 11.1 $pb^{\perp 1}$ of data at 161 GeV and 10.6 $pb^{\perp 1}$ of data at 172 GeV is about 500 TeV for a neutralino mass of 71 GeV/c^2.

Another model that predicts the gravitino to be the LSP and the neutralino to be the NLSP is the so-called 'No-Scale Supergravity' model proposed by Lopez, Nanopoulos and Zichichi (here after referred to as the LNZ model) [22, 23, 24, 25]. Phenomenologically this model is exactly the same as GMSB except that the neutralino always decays at the interaction point and the gravitino mass is several orders of magnitude smaller.

The one-photon process $e^+e^\perp \to \chi_1^0\tilde{G} \to \tilde{G}\tilde{G}\gamma$ is expected to be produced at LEP2 only for very light gravitino masses as the cross section scales as the inverse of the gravitino mass squared [26]. For a gravitino mass of $10^{\perp 5}$ eV/c^2 the cross section is predicted to be around 1 pb. In the LNZ model the gravitino mass is allowed to be

this light [24], but in GMSB the gravitino is predicted to have a mass greater than 1 eV/c^2. Thus, this process is expected in the LNZ model but not in GMSB models.

The energy range for the photon is spread around $\frac{M_{\chi_1^0}}{2}$ and can be written as in equations (1.11 - 1.13). The velocity β, however, is quite different and depends on the mass of χ_1^0 and $\sqrt{s}$ (analogous to the $e^+e^\perp \rightarrow \chi_2^0\chi_1^0$ production, but here the gravitino mass is effectively zero). The velocity of χ_1^0 is given by:

$$\beta = \sqrt{\frac{p^2}{p^2 + M^2_{\chi_1^0}}} \tag{1.16}$$

with

$$p = \frac{s - M^2_{\chi_1^0}}{2\sqrt{s}}. \tag{1.17}$$

The dominant Feynman diagrams are shown in Figure 1.6

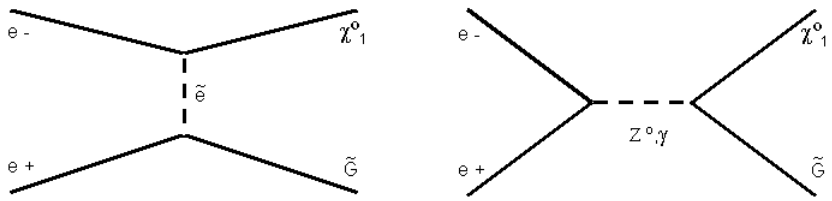

Figure 1.6: *The dominant Feynman diagrams for the* $e^+e^\perp \rightarrow \chi_1^0\tilde{G}$ *process.*

1.2.4 The CDF Event

In 1995, CDF observed an unusual event with two high-energy electrons, two high-energy photons, and a large amount of missing transverse energy [27] (shown

in Figure 1.7). There is no obvious Standard Model explanation for this event [28]. However it fits nicely into the supersymmetric models discussed above. In χ_1^0 LSP Supersymmetry the CDF $ee\gamma\gamma + E^T_{MISS}$ event could be explained by the Drell-Yan process $q\bar{q} \to \tilde{e}\tilde{e} \to ee\chi_2^0\chi_2^0 \to ee\chi_1^0\chi_1^0\gamma\gamma$ where the two χ_1^0's escape detection resulting in missing transverse energy. If this is the explanation for the CDF event, the best possibility for discovery at LEP is $e^+e^\perp \to \chi_2^0\chi_2^0 \to \chi_1^0\chi_1^0\gamma\gamma$, seen in the detector as two acoplanar photons. In gravitino LSP models, the CDF event could be explained by $q\bar{q} \to \tilde{e}\tilde{e} \to ee\chi_1^0\chi_1^0 \to ee\tilde{G}\tilde{G}\gamma\gamma$. The best channel for discovery at LEP is $e^+e^\perp \to \chi_1^0\chi_1^0 \to \tilde{G}\tilde{G}\gamma\gamma$, seen in the detector as two acoplanar photons [6].

1.2.5 Closing Remarks on the Search for Supersymmetry

In χ_1^0 LSP Supersymmetry the neutralino compositions, photino and higgsino, which give a 100% Branching Ratio for the decay $\chi_2^0 \to \chi_1^0\gamma$ are motivated by the CDF event. It could very well be that the χ_2^0 is pure photino but there is no theoretical preference to select this neutralino composition as opposed to any other. Neutralino compositions other than the prudent choice of pure photino and higgsino generally have very low Branching Ratio for the decay $\chi_2^0 \to \chi_1^0\gamma$ and therefore photons are not generally considered the best topology to search for χ_1^0 LSP Supersymmetry. In GMSB the χ_1^0 is calculated to be pure B-ino and the decay $\chi_1^0 \to \tilde{G}\gamma$ is the ONLY allowed decay mode (for $M_{\chi_1^0} < M_Z$). Similarly, in the LNZ model the neutralino

[6] Of course, one can have the process $e^+e^\perp \to \tilde{l}\tilde{l} \to l^+l^\perp\tilde{G}\tilde{G}$ at LEP, but for most gravitino LSP models the χ_1^0 is the least massive superpartner, and therefore can be produced at lower center-of-mass energy. In the minimal model of Gauge-Mediated Supersymmetry Breaking this is always true except at very large $\tan\beta$. In the LNZ model this is always true.

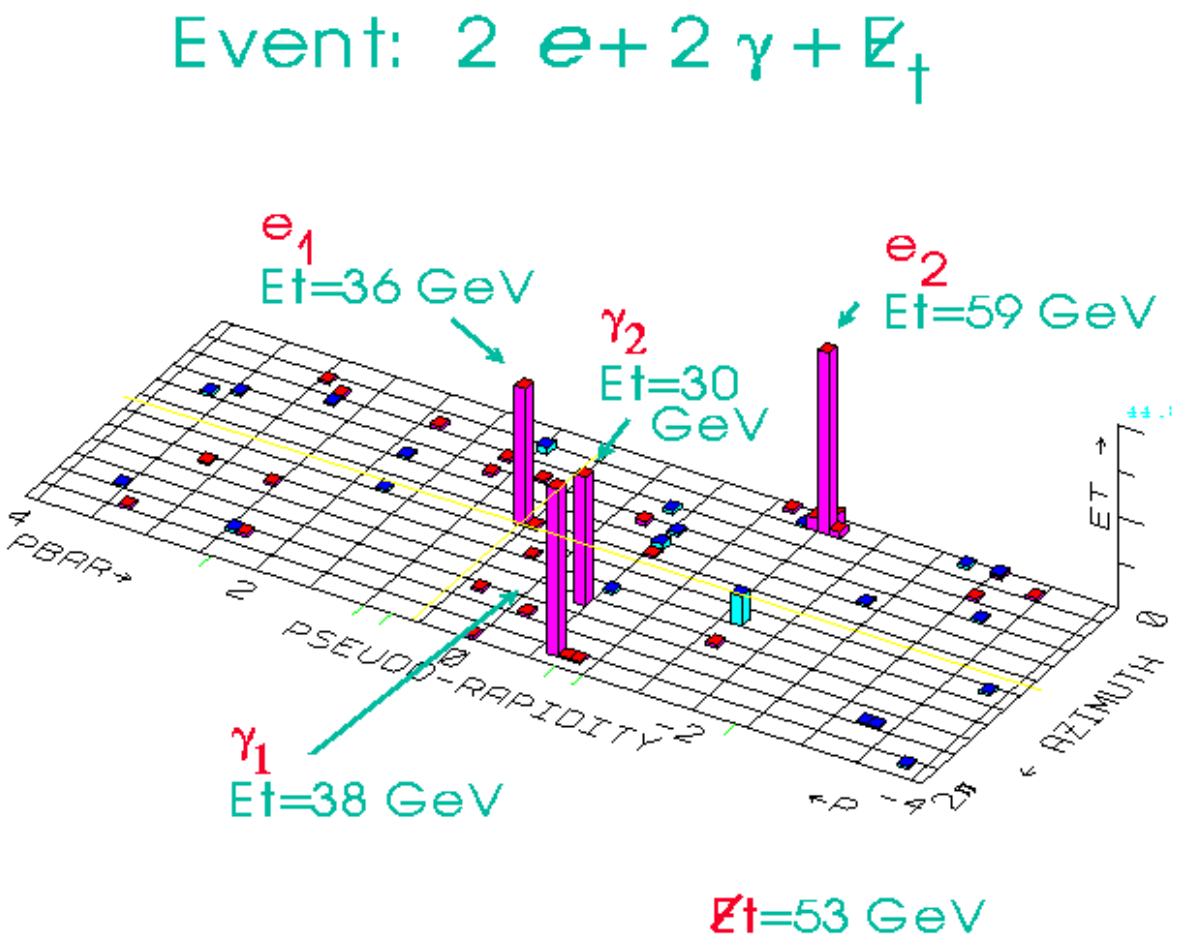

Figure 1.7: *The CDF event* .

always decays into a gravitino and a photon. At LEP, photon events are not only a good place to search for gravitino LSP Supersymmetry, it is the best place to search!

1.2.6 Compositeness

Compositeness theories [29, 30] assume that the fermions and gauge bosons are not point particles but are in fact composed of a deeper underlying structure (elementary

particles often labeled preons). In this scenario, the electron mass would arise from the solution to its bound state just as the mass of the pion arises from the bound state solution of the 'u' and 'd' quarks. The preons are thought to be bound together by a confining interaction at a very high energy scale. None of the proposed composite models is able to predict this energy scale. If the Standard Model is part of a more general 'composite' theory the Lagrangian must be modified and can be written as

$$L = L_{\mathrm{SM}} + L_{\mathrm{eff}}$$

where L_{eff} takes into account the new interactions due to compositeness. Given the success of the Standard Model at low energies, L_{eff} must become negligible as the interaction energy tends towards zero. L_{eff} , of course, depends on the specific compositeness model. The simplest one is to state that an observation of QED breakdown implies that the electron has a finite size. The idea is that as the energy is increased higher and higher we are probing deeper and deeper into the electron and at some point the structure of the electron would manifest itself in the reaction $e^+e^\perp \rightarrow \gamma\gamma(\gamma)$. When the energy is sufficiently high the process $e^+e^\perp \rightarrow \gamma\gamma(\gamma)$ can not be calculated solely from QED. At this 'cut-off' energy Λ the cross section and angular distribution for $e^+e^\perp \rightarrow \gamma\gamma(\gamma)$ is determined by the full composite theory Lagrangian $L = L_{\mathrm{SM}} + L_{\mathrm{eff}}$. Historically, the effects of QED breakdown, for a large momentum transfer, has been parameterized by modifying the propagator with the form factor:

$$F_{\pm}(q^2) = 1 \pm \frac{q^4}{\Lambda_{\pm}^4}$$

where q is the momentum transfer and $\Lambda_{\pm}$ are the so-called QED cut-off parameters. This leads to a modified lowest order differential cross section [31]

$$\left(\frac{d\sigma}{d\Omega}\right) = \left(\frac{d\sigma}{d\Omega}\right)_{QED} \left(1 \pm \frac{s^2}{2\Lambda_{\pm}^4}(1-\cos^2\theta) + \frac{s^4}{16\Lambda_{\pm}^8}(1-\cos^2\theta)^2\right) \tag{1.18}$$

where Λ_+ refers to the case of constructive interference between the QED Feynman diagrams and the compositeness diagrams, and $\Lambda_\perp$ refers to the case of destructive interference. Compositeness theories can only be calculated at the Born level because they are non-renormalizable.

1.2.7 Excited Electron

Electron compositeness may also become apparent due to the existence of excited states. If the electron is made of preons it will have excited states. The reaction $e^+e^\perp \rightarrow \gamma\gamma(\gamma)$ may proceed via excited electron exchange (as shown in Figure 1.8) in addition to the normal QED diagrams. Assuming a magnetic coupling of the excited

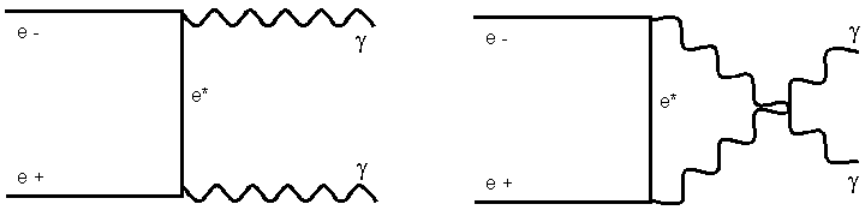

Figure 1.8: *The Feynman diagrams for $\gamma\gamma$ pair production through e^* exchange.*

electron e^* to $e\gamma$ of the form [32] $\frac{e\lambda}{2M_e^*}\overline{\Psi}_{e^*}\sigma_{\mu\nu}\Psi_e F^{\mu\nu} + h.c.$ where M_e^* is the mass of e^* and λ is a measure of the coupling strength, then the differential cross section is given by [30]

$$\frac{d\sigma}{d\Omega} = \left(\frac{d\sigma}{d\Omega}\right)_{QED}\left(1 + s^2\left(\frac{\lambda}{M_{e^*}}\right)^2 H_1(s,\theta) + \frac{s^3}{4}\left(\frac{\lambda}{M_{e^*}}\right)^4 H_2(s,\theta)\right) \tag{1.19}$$

where

$$H_1(s,\theta) = \frac{\sin^4\theta(s - 2M_{e^*}^2) + 4M_{e^*}^2\sin^2\theta}{(1+\cos^2\theta)(s^2\sin^2\theta + 4sM_{e^*}^2 + 4M_{e^*}^4)} \tag{1.20}$$

and

$$H_2(s,\theta) = \frac{s^3\sin^8\theta + 8s^2M_{e^*}^2\sin^6\theta + 4sM_{e^*}^4\sin^4\theta(5+\cos^2\theta) + 32M_{e^*}^6\sin^2\theta}{(1+\cos^2\theta)(s^2\sin^2\theta + 4sM_{e^*}^2 + 4M_{e^*}^4)^2}. \tag{1.21}$$

Until now, no evidence of any underlying structure of fermions or gauge bosons has been observed [33, 34]. Nevertheless, even considering the large statistics of the LEP Z peak running, as LEP2 marches up in energy the potential for discovering compositeness marches up as well. This is true because the dependence of the Λ limit on the center-of-mass energy $\sqrt{s}$ and on the luminosity L is :

$$\Lambda \propto s^{3/8}L^{1/8}$$

The dependence on luminosity is down by a square root due to the presence of the largely irreducible background of QED events. In addition, the QED cross section is proportional to one over the center-of-mass energy squared which gives rise to be 3/8 power term for the center-of-mass energy squared. This thesis studies the data from 161 GeV and 172 GeV center-of-mass energies. The center-of-mass energy is almost doubled compared to the Z peak data, which more than compensates for the

lack of luminosity (down by a factor of 7.7). Hence, the potential for discovery of compositeness in the $e^+e^\perp \to \gamma\gamma(\gamma)$ process is significant.

1.3 Conclusion

This thesis describes the study of events where the only detected particles are photons. The cross section for the EW process $e^+e^\perp \to \nu\bar{\nu}\gamma(\gamma)$ is measured and compared to the Standard Model prediction. The missing mass and polar angle distributions are also studied and compared to the Standard Model. The QED process $e^+e^\perp \to \gamma\gamma(\gamma)$ is measured in terms of its cross section and polar angle distribution and compared to the Standard Model predictions.

This thesis also describes the search for any peculiarities in photon only final state events at the highest energies ever studied by man (that is until the 1997 running at 183 GeV). In particular, Supersymmetry is searched for. If verified, Supersymmetry would go a long way in explaining how the universe was formed. The search for compositeness (which , if verified, would uncover another layer in the search for the fundamental building blocks of matter) is described, as well, in this thesis.

The results of this thesis are actually more general than the introduction indicates. The Supersymmetry and compositeness models described above are simply reference models. The results of this thesis are applicable to any type of new physics that predicts photon only final state events in $e^+e^\perp$ collisions. For example, acoplanar photons are used to study the reaction $e^+e^\perp \to \chi_1^0\chi_1^0 \to \tilde{G}\tilde{G}\gamma\gamma$ and $e^+e^\perp \to \chi_2^0\chi_2^0 \to \chi_1^0\chi_1^0\gamma\gamma$,

but the cross section upper limits derived for these processes apply as well to the generic process $e^+e^\perp \to XX \to YY\gamma\gamma$ where Y is massless or has mass.

The rest of this thesis proceeds as follows. In Chapter 2 the LEP accelerator and ALEPH detector are briefly described with emphasis on the details that are relevant to this thesis. Chapter 3 details the analysis for the EW process, the EW cross section measurement and the search for Supersymmetry in the one-photon data sample. The search for Supersymmetry using acoplanar photons and comparisons to the interesting event found by the CDF collaboration are presented in Chapter 4. In Chapter 5, the QED analysis and cross section measurement is described. In addition, the search for compositeness using this data sample is presented. The conclusions are stated in Chapter 6. Appendix 1 contains the combination of results from all four LEP experiments for the search for GMSB.

Chapter 2

The ALEPH Detector at LEP

The Large Electron–Positron (LEP) accelerator has been designed to collide electrons and positrons at the Z boson mass. The ALEPH (Apparatus for LEP Physics) detector has been built to measure the events created by the $e^{+}e^{\perp}$ collisions in LEP. ALEPH is an all-purpose detector, designed to detect a large variety of Z decays. The hermetic construction of ALEPH allows the detector to measure all electromagnetic and hadronic energy from an interaction except for a small region of polar angle 34 mrads around the beam axis.

Beginning in June 1996, with the installation of super-conducting cavities the LEP2 phase commenced. By the end of LEP2, 272 super-conducting cavities will be installed and the center-of-mass energy will reach about 192 GeV. The object of this increase in energy is to measure the $W^{\pm}$ mass and to search for the Higgs boson, Supersymmetry, and whatever else is behind the next energy frontier.

This work presents results based on the first year of data taking at LEP2, where

the ALEPH detector recorded 11.1 $pb^{\perp 1}$ of data at $\sqrt{s} = 161$ GeV 1.1 $pb^{\perp 1}$ of data at $\sqrt{s} = 170$ and 9.5 $pb^{\perp 1}$ of data at $\sqrt{s} = 172$ GeV. The data analyzed in this thesis and the results that follow are the result of an enormous international collaboration requiring many years of work and cooperation by hundreds of physicists, engineers and technicians.

2.1 The Large Electron–Positron Storage Ring

LEP is the largest accelerator in the world. It is located across the French–Swiss border extending from the outskirts of Geneva to the base of the Jura mountains. With a circumference of 26.6 km and at a depth of roughly 100 m, LEP truly fits the definition of the modern-day meaning for 'Big Science'.

LEP accelerates and maintains electrons and positrons up to 86 GeV (96 GeV by completion of LEP2) in circular orbits in opposite directions and makes them collide every 22 μs at the four places where the detectors (ALEPH, DELPHI, L3, OPAL) are located.

To obtain this high energy efficiently, the electrons and positrons are produced and pre-accelerated up to 22 GeV before injection into LEP using the existing CERN accelerators. Figure 2.1 shows the LEP injection chain.

The linear accelerator (LINAC) consists of two linear accelerators in tandem. In the first stage, electrons are produced from a high-intensity gun and accelerated to 200 MeV. They are then passed through a tungsten target to produce positrons. In

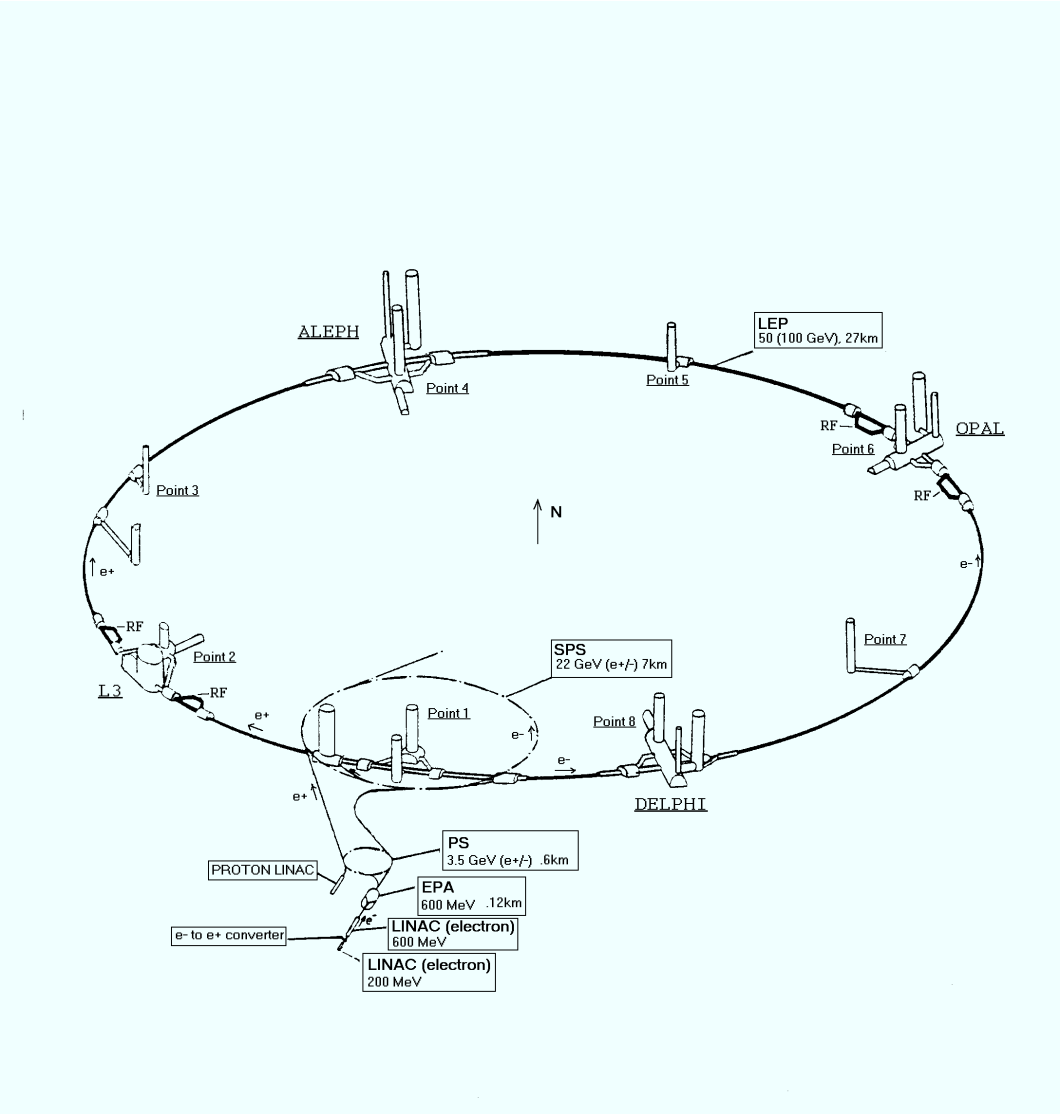

Figure 2.1: *The LEP storage ring with supporting injection accelerators*

the second part of the LINAC, the electrons and positrons are boosted to 600 MeV before being passed on to the Electron Positron Accumulator (EPA). In the EPA the electrons and positrons are accumulated separately into bunches and cooled by synchrotron radiation. These bunches are sent to the Proton Synchrotron (PS) where their energy is brought up to 3.5 GeV. After the PS, they are passed to the Super Proton Synchrotron (SPS) where they reach 22 GeV each. Finally, they are injected into LEP, and accelerated to their maximum energy.

2.2 The LEP2 energy upgrade

Beginning in 1996, the LEP2 phase of LEP began. For the first time in history man has collided electrons and positrons at and above the $W^+W^\perp$ threshold. What lurks beyond this energy frontier is the subject of this thesis. The most crucial parameters for physics at LEP2 are the maximum beam energy and the integrated luminosity.

The beam energy is limited by the RF voltage needed to replenish the losses due to synchrotron radiation. Since radiation losses increase as $\mathrm{E}^4_{\mathrm{beam}}$ the required RF voltage increases by a factor of 16 as the beam is increased from 45 GeV at LEP1 to approximately 90 GeV at LEP2 (as shown in Figure 2.2). Increasing the RF voltage by a factor of 16 is made possible by the installation of 272 super-conducting cavities (sc). In order to reach $\sqrt{s} = 161$ GeV LEP installed 144 sc; an additional 32 sc were installed for the 172 GeV run. The total of 176 sc for the 1996 run allows almost 2 GV of RF voltage. The remaining 96 sc will be installed by the summer of 1998,

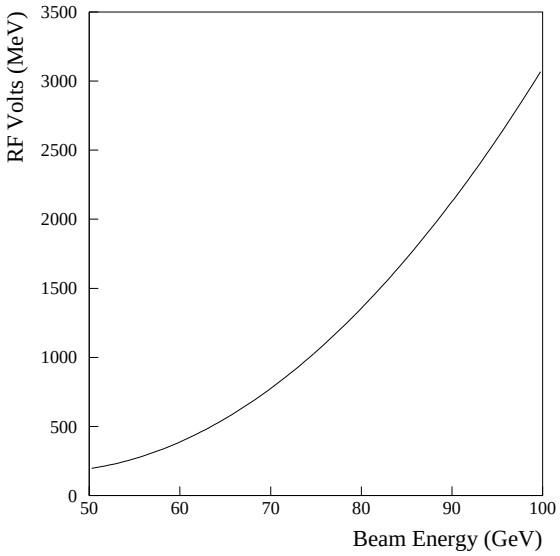

Figure 2.2: *RF voltage as a function of beam energy.*

allowing a maximum beam energy of 96 GeV.

Unlike LEP1 where the luminosity was limited by beam-beam interactions, LEP2 is limited by the total current. For LEP2 the luminosity can be written as [35]

$$\mathrm{L} \propto \mathrm{k_b} \left(\frac{i_\mathrm{b}^2}{\sigma_x \sigma_y} \right) = \left(\frac{i_\mathrm{total}^2}{\mathrm{k_b} \sigma_x \sigma_y} \right). \tag{2.1}$$

where i_b is the bunch current, i_{total} is the total current, $\mathrm{k_b}$ is the number of bunches and σ_x, σ_y are the spread of the beam perpendicular to its direction. Table 2.1 gives some typical values [36] for the luminosity parameters. Thus, the luminosity is maximized by storing the maximum amount of current in the minimal number of bunches. Putting all of the available current in one bunch is ideal, but the current in a bunch is limited by something called the Transverse Mode Coupling Instability [37].

Parameter	Typical value
σ_x	0.25 mm
σ_y	0.004 mm
k_b	1 or 2
i_b	750 μA
average luminosity	0.5 $pb^{\perp 1}$/day

Table 2.1: *Typical values for the luminosity parameters.*

The maximum current that can be put in a bunch at LEP2 is called the bunch current threshold. Therefore operating in two bunch mode becomes economical when the total amount of current surpasses the bunch current threshold. Maximizing the injection beam energy to 22 GeV along with fine tuning of the machine parameters to maximize the bunch current [38] allows LEP2 to run at a peak luminosity of greater than $10^{31}\,cm^{\perp 2}\,s^{\perp 1}$.

The 1996 run attained the desired energy goals of $\sqrt{s}$ = 161 GeV and 172 GeV and a maximum integrated daily luminosity of 1.1 $pb^{\perp 1}$.

2.3 Overview of the ALEPH detector

ALEPH is an all-purpose detector located in Point 4 of the LEP accelerator ring. The electrons and positrons collide in the center of the detector, called the Interaction Point (IP). A cut away view of the entire ALEPH detector is shown in Fig. 2.3.

The inner-most detector is the Vertex Detector (VDET), a silicon detector especially important for precision tracking (like detecting b quark events). The next

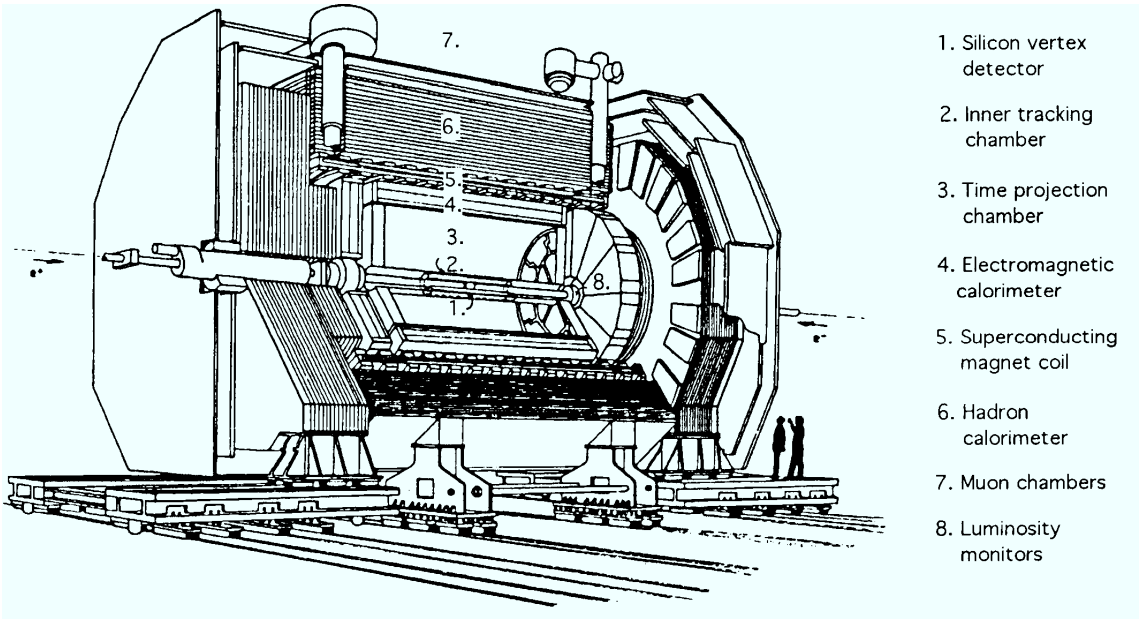

Figure 2.3: *The ALEPH detector.*

detector out is the Inner Tracking Chamber (ITC), a tracking detector of gas and wires especially important for triggering. The Time Projection Chamber (TPC) is the main tracking detector covering a radius of 1.8 m. Next out in radius from the IP is the Electromagnetic Calorimeter (ECAL); this detector is essential in measuring photon and electron energy and position. The ALEPH Magnet encompasses the VDET, ITC, TPC and ECAL allowing the momentum to be measured for charged particles. Outside the ALEPH Magnet is the Hadronic Calorimeter (HCAL) which is responsible for measuring hadronic energy and identifying muons. Located at low polar angles are the luminosity monitors, the LCAL and SiCAL. These two detectors serve the very important function of measuring the luminosity. In addition, the analysis presented in this thesis utilizes these two detectors to veto events that have

energy detected at low polar angles.

The ALEPH coordinate system used throughout this thesis is defined as such. The z axis points in the $e^{\perp}$ orbit direction, x is horizontal and points to the center of LEP, and $y = z \times x$ points almost straight up.

2.4 The ALEPH Magnet

The magnet, consisting of an iron yoke and a super-conducting coil, surrounds the three tracking detectors and the Electromagnetic Calorimeter. It provides a homogeneous magnetic field of 1.5 T parallel to the LEP beam allowing the measurement of the charge and momentum of charged particles through the relation:

$$p = \frac{0.003\, B\rho}{\sin\theta} \tag{2.2}$$

where p is the momentum in GeV/c , θ is the angle of the track relative to the field axis, B is the field strength in tesla, and ρ is the radius of curvature in centimeters. This relation is derived from the Lorentz force law.

The super-conducting coil consists of a main solenoid and two compensating coils at the ends; the total length is 7.24 m. The solenoid normally carries 5000 A of current producing 736 MJ of stored energy. To stabilize the temperature at superconductivity levels (4° K in this case), refrigeration and liquid helium is used.

The large amount of iron in the HCAL, used as a sampling medium, serves to ensure the uniformity of the magnetic field and return of the magnetic field flux.

2.5 The Vertex Detector

The ALEPH vertex detector is a silicon microstrip detector which gives extremely precise three-dimensional coordinates on charged particle trajectories close to the interaction point. The vertex detector is very important in finding the secondary vertex of $Z \rightarrow b\bar{b}$ events and in improving the track parameter resolution in general. The VDET is not used in the analysis of this thesis but its description is included below for completeness.

The VDET95 (the vertex detector used during LEP2 data taking) is approximately 40 cm long with two layers at radial distances of 6.3 and 10.8 cm (as shown in Figure 2.4). The two concentric layers of silicon wafer strips have readout strips on both sides (as shown in Figure 2.5).

The 'r-ϕ side' with strips parallel to the beam measures the ϕ-coordinate of particle tracks whereas the z-coordinate is measured by strips perpendicular to the beam on the other side, the 'z side'.

Track coordinates are reconstructed by averaging the charge-weighted positions of adjacent strips that are at least three sigma above the mean noise charge. The point resolution achieved in 1996 is $\sigma_{r\phi} \approx 12$ μm, $\sigma_z \approx 14$ μm for $\mid \cos\theta \mid$ less than 0.4. The readout chip (MX-7RH) can stand a radiation dose of 1 Mrad.

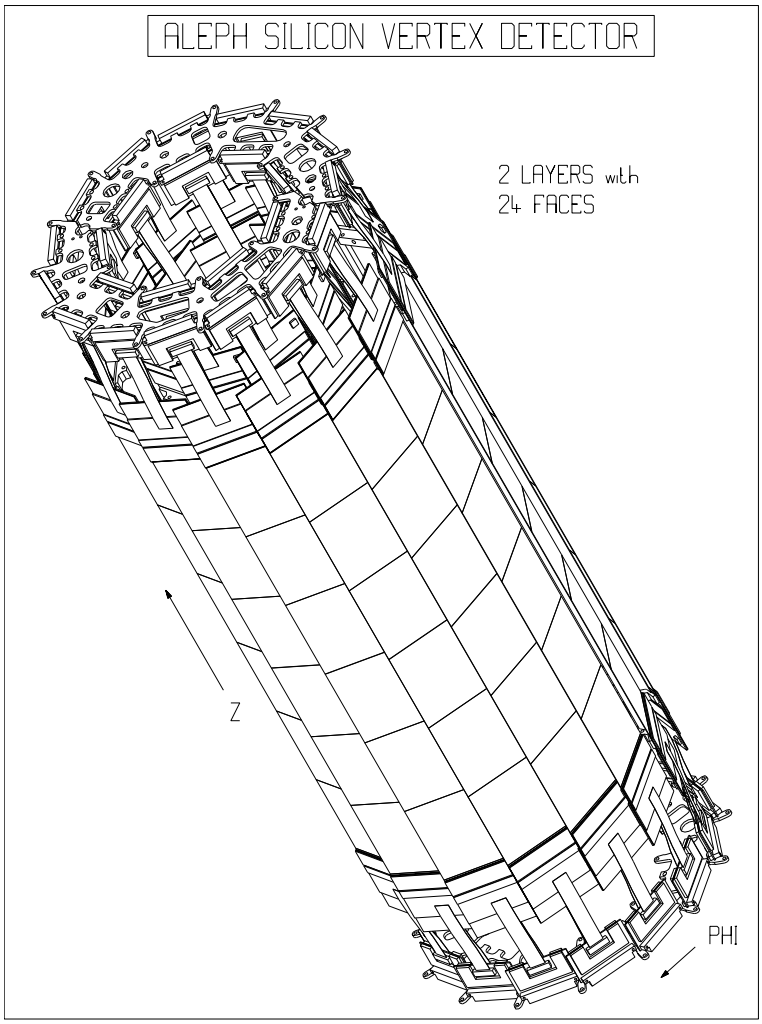

Figure 2.4: *3d view of the ALEPH vertex detector.*

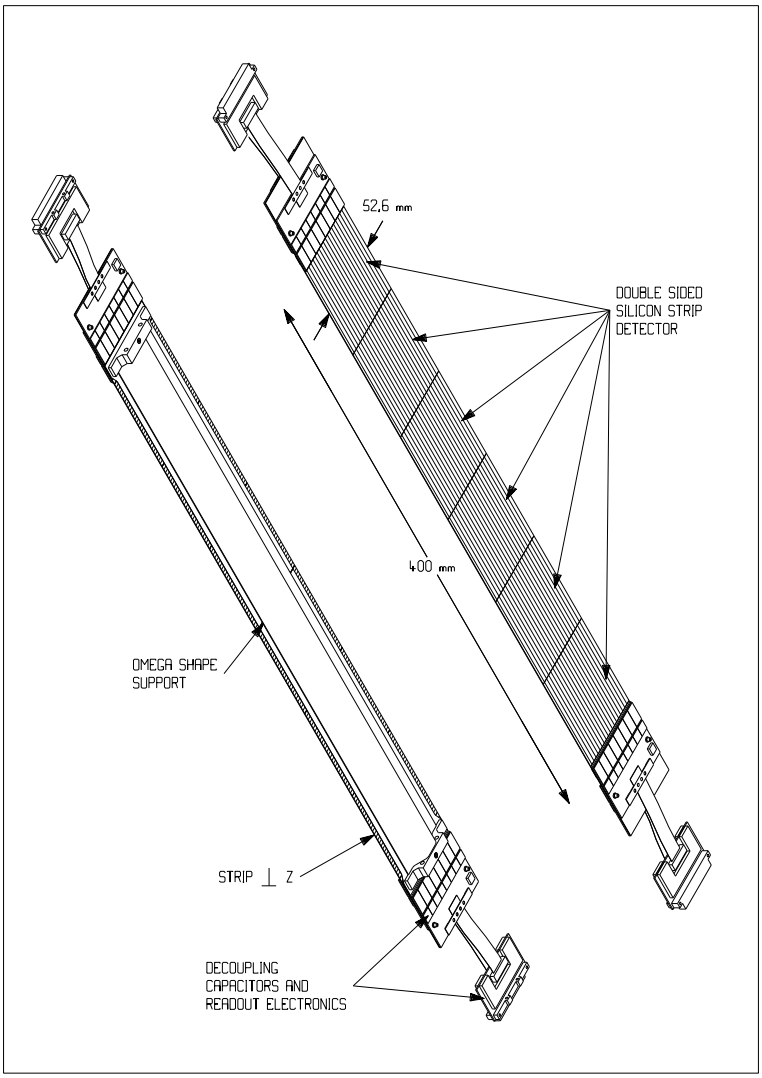

Figure 2.5: *The vertex detector faces.*

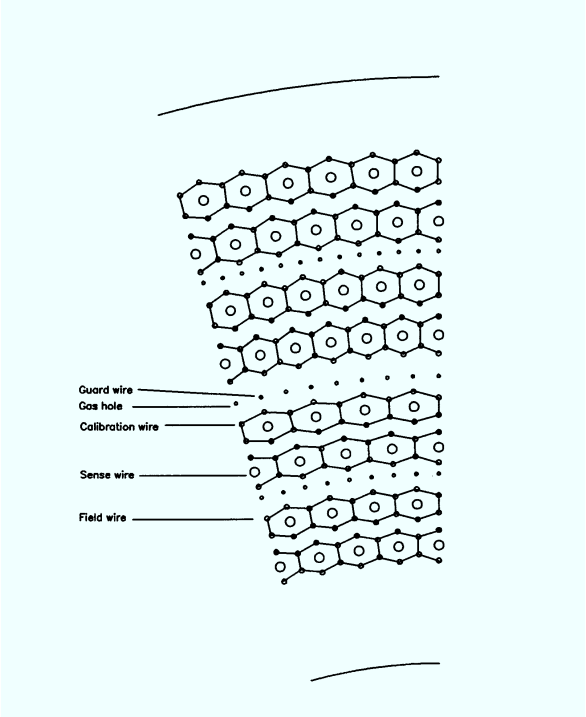

Figure 2.6: *Detail of an ITC end-plate.*

2.6 The Inner Tracking Chamber

The Inner Tracking Chamber (ITC) is a multi-wire drift chamber serving a dual purpose in ALEPH. It provides up to eight r-ϕ points for tracking and it delivers the only tracking information for the first-level trigger.

The ITC is 2 meters long (corresponding to angular coverage $|\cos\theta| \leq 0.97$) and covers the radial region from 16 cm to 26 cm. There are 960 sense wires distributed over eight concentric layers parallel to the beam axis. Figure 2.6 shows a cross section perspective of the ITC.

The ITC volume is filled with a gas mixture of 80% argon and 20% carbon dioxide. A charged particle traversing the ITC ionizes the atoms in the gas. The ionized electron drifts with a mean velocity of 50 μm/ns towards the sense wires which are held at 2 kV.

The r-ϕ coordinate of a charged particle trajectory is obtained by measuring the drift time within a fired cell. The resolution is 150 μm. The z coordinate is inferred through the difference in pulse arrival time between two ends of a wire. The resolution is only about 3 cm, insufficient to be used for tracking reconstruction but adequate for a three-dimensional trigger decision.

In the search for events where only photons are detected (photon only final states), the ITC is essential as a veto of low momentum charged tracks. Low momentum charged tracks (0.14 GeV/c for particles produced at 90° to the beam axis) will not traverse the TPC and, thus, the ITC is relied upon to eliminate these events.

2.7 The Time Projection Chamber

The Time Projection Chamber (TPC) is the 'Big Daddy' of the tracking detectors (VDET, ITC, TPC) and the central detector in ALEPH. The time projection chamber with an inner radius of 31 cm, an outer radius of 180 cm and 440 cm long is the largest of its kind (shown in Figure 2.7).

Dividing the chamber into two halves is a graphite-coated Mylar membrane (25 μm thick) that is held at -25 kV. The two end-plates are held at ground. Each end cap

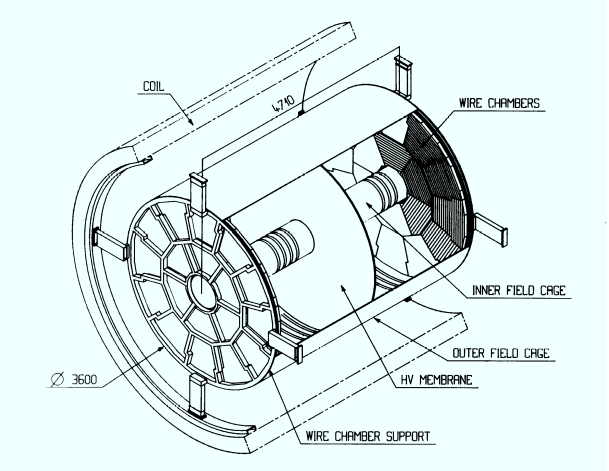

Figure 2.7: *The TPC mechanical structure.*

is fitted with 18 proportional wire chambers (or 'sectors') which measure ionization energy (used for particle identification), r-ϕ position and drift time. The sectors contain sense wires and segmented cathode pads (size 6.2×30 mm^2, 21 rows in radial direction), as shown in Figure 2.8. The TPC is operated with an argon-methane (91:9) gas mixture at atmospheric pressure. A charged particle traversing the volume of the TPC produces electrons and ions. The electrons from primary ionization drift towards one of the end-plates in the axial magnetic field of 1.5 T and an electric field of 125 V/cm.

In the vicinity of a sense wire, the electrons create an avalanche and induce a signal on the cathode pads. The signals are used to measure the energy (dE/dX used for particle identification discussed below) and the coordinates of the track.

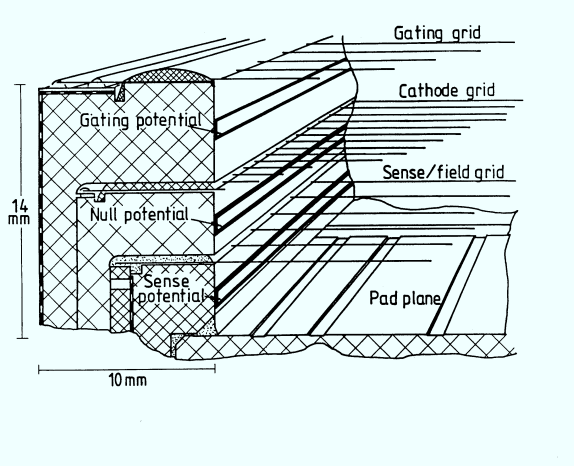

Figure 2.8: *Schematic diagram of a sector edge, showing wire attachment, pad plane, wire grades, and potential strips.*

Azimuthal coordinates are derived from the r-ϕ position of the recorded avalanche with a resolution of 170 μm. The z position of a point on the trajectory is deduced from the drift velocity of electrons in the electric field. The mean drift velocity is 5.24 cm/μs, which corresponds to a drift time of 42 μs for the maximal drift length of 2.2 m. The pads are read out every 200 ns starting from the beam crossing. The z resolution depends on the polar angle; it is 740 μm for a particle at $\theta = 90°$.

In addition to its primary role as a tracking device, the TPC also does particle identification by measuring the energy loss per unit length by ionization ($\mathrm{d}E/\mathrm{d}X$) of a charged particle. The $\mathrm{d}E/\mathrm{d}X$ is parameterized by the Bethe-Bloch relation

$$\frac{\mathrm{d}E}{\mathrm{d}X} = -A\frac{1}{\beta^2}(\ln\beta\gamma - \beta^2 + B)$$

where A and B are constants, β is the scaled velocity v/c and γ is the boost factor $1/\sqrt{1-\beta^2}$.

The dE/dX depends on the mass and momentum of the charged particle. Thus, the measurement of the dE/dX together with the momentum provides a mass measurement for the particle and thus a particle identification. Figure 2.9 is a scatter plot of dE/dX vs. momentum for a large number of tracks. The different particle types are clearly discernible.

For the analysis of photon only final states the TPC is essential in identifying tracks that come from a photon conversions and, of course, in eliminating events with charged tracks that do not come from a photon conversion.

2.8 Overall Tracking Performance

Tracks are reconstructed starting in the TPC. Nearby hits are connected requiring consistency with a helix pattern (the pattern of a charged particle in a magnetic field). These tracks are then linked to hits in the ITC and VDET. The final track is determined using a fitting technique [39] taking into account the track hit errors and multiple scattering. The transverse momentum resolution is given by

$$\sigma(1/p_T) = 0.6 \times 10^{\perp 3}(\mathrm{GeV}/c)^{\perp 1} \tag{2.3}$$

for 45 GeV muons.

Two tracks close together in space can be separated into individual tracks if they are more than 1.5 cm apart in r-ϕ or 2 cm apart in z. A photon conversion is not reconstructed if both the r-ϕ and z distances between tracks are smaller than the above distances.

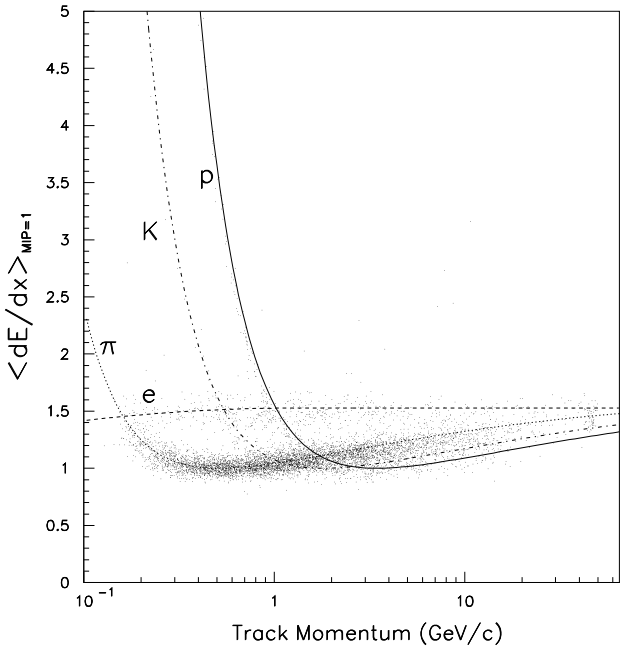

Figure 2.9: *Particle identification using dE/dX.*

2.9 The Electromagnetic Calorimeter, ECAL

The ECAL (shown in Figure 2.10) is a lead/wire-chamber sampling device. It is the last detector inside the ALEPH magnet. The barrel has an inner radius of 185 cm and an outer radius of 225 cm. The endcaps are located 255 cm from the IP and extend from 57 cm to 228 cm in radius. The nominal thickness of a module is 22 radiation lengths divided into three sections in depth ('stacks') corresponding to the first four, the middle nine, and the last nine radiation lengths.

The ECAL is formed of a barrel, surrounding the TPC, and closed at each end by endcaps A and B. The barrel and two endcaps are each divided into 12 modules, each covering an azimuthal angle of 30°. The cracks between modules form only 2% of the barrel and only 6% of the endcaps. Aside from the cracks and inside $|\cos\theta| < 0.97$, the ECAL is a completely hermetic detector. Each module is made up of 45 layers with each layer containing a lead sheet (converter detector), an anode wire plane, and a cathode pad plane. An ECAL module is divided into three stacks. The first stack of the module comprises 10 of the 45 layers, the second stack contains 23 layers, and the third stack has 12 layers. The lead sheets in stacks 1 and 2 are 2 mm thick. In the third stack the lead sheets are 4 mm thick.

Inside each one of the 45 planes are between 195 and 233 gold-plated tungsten wires, 25 μm in diameter and with 5 mm pitch. The total energy of each plane is read out. The total wire energy of a module (the sum of the 45 planes) is used for trigger information as well as a check of the pad energy measurement. The formation of a plane in an ECAL module is shown in Figure 2.11.

The total energy and position of the electromagnetic showers are measured using small (30×30 mm^2) cathode pads of sizes approximately equal to the width of an electromagnetic shower. The cathode pads are connected internally to form 'towers' pointing to the interaction point (in total there are 73,728 towers).

Energy and spatial resolution are measured from real data over a range of energies using Bhabha events (typically 45 GeV electrons), τ-pair events involving the decay $\tau \to e\nu\nu$ (10–30 GeV electrons) and $e^+e^\perp \to e^+e^\perp e^+e^\perp$ events (1–10 GeV electrons).

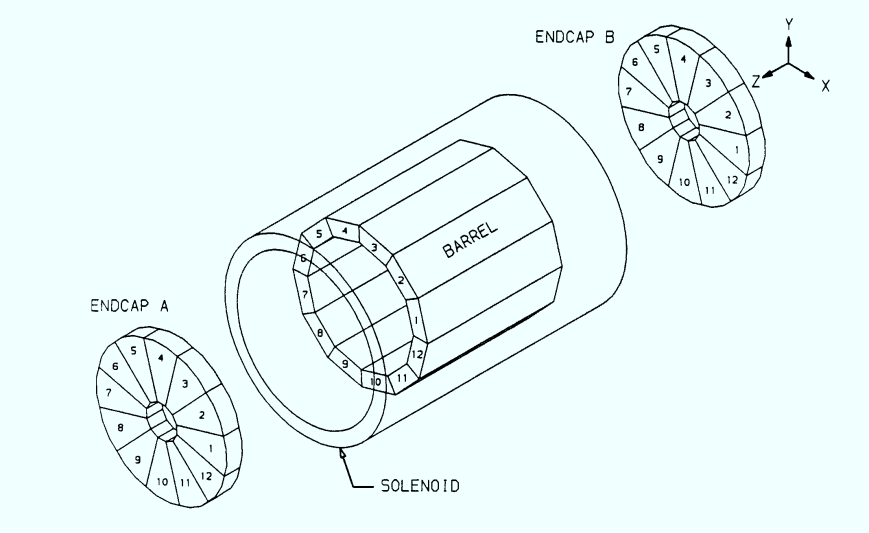

Figure 2.10: *The ECAL.*

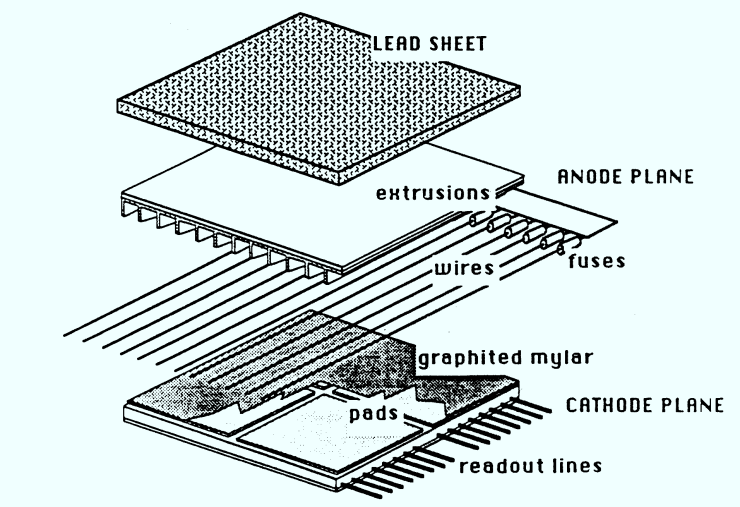

Figure 2.11: *Typical stack layer.*

After energy corrections for:

- ionization losses before the ECAL
- shower leakage
- saturation

the energy of each electromagnetic cluster (neighboring towers that recorded energy above the threshold of 20 MeV) is compared to the final momentum of the electron, as measured by the tracking chambers. Ionization losses amount to 30 MeV for a 45 GeV electron. Losses in energy due to track ionization are obviously not important for photons. Shower leakage effects due to the shower not being fully contained in a module is most evident at normal incidence ($\theta = 90°$). The effect is to modify the measured energy by a term proportional to the energy. At normal incidence for an energy of 50 GeV it is about a 1% correction. The saturation correction is applied to correct for the saturation levels of the individual cathode pads. The saturation effect is proportional to the energy and independent of the incident angle and found to be

$$Saturationeffect = \alpha_1 \mathrm{E}$$

$$\alpha_1 = (7.8 \pm .6) \times 10^{\perp 4} \mathrm{GeV}^{\perp 1}.$$

The dependence of the energy resolution as a function of energy is found by fitting the data samples mentioned above. The corresponding fitted resolution [39] is

$$\frac{\sigma_E}{E} = \frac{0.18}{\sqrt{E}(\mathrm{GeV})} + 0.009 \ . \tag{2.4}$$

The spatial coordinates are found by measuring the center of gravity of the electromagnetic shower from the four leading towers (the four most energetic connected towers of the shower). The angular resolution is measured, as above for the energy, by using electrons from real data and comparing to the TPC measurement. The angular resolution is found to be

$$\sigma_{\theta/\phi} = \frac{2.5}{\sqrt{E}(\mathrm{GeV})} + 0.25 \text{ mrad} . \tag{2.5}$$

Both the energy and spatial resolution are checked by test beams with photons and found to agree with the respective measurements from electrons.

Another important feature of the ECAL is that it measures the time between the beam cross-over (synchronized to the LEP beam pickup) and the time when energy from an event is deposited in the ECAL. The interaction time relative to the beam crossing ($t_\circ$) is found by taking the energy weighted average of the $t_\circ$ measurement from each wire plane. The $t_\circ$ of each module is calibrated using data. Normally there is an overall offset and a dependence on the fraction of energy in stack three where the gain is double that of stacks one and two. This timing measurement is especially useful in eliminating cosmic ray events.

The ECAL is the only detector for photon identification and photon momentum reconstruction. Photons are identified by their characteristic shower in the ECAL and the lack of a charged track pointing to its shower. Photon momentum is reconstructed by determining the energy from its shower in the ECAL and assuming the photon originated from the IP. In addition, the well-defined electromagnetic shower in the

ECAL is utilized to separate electrons from other charged particles. This is essential in order to properly identify photon conversions.

2.10 The Hadronic Calorimeter, HCAL

The HCAL constitutes the main support of ALEPH. The large iron structure collects the return flux of the magnetic field and acts as the absorber of hadrons, measuring their energy. The HCAL is also essential for muon identification.

The HCAL is constructed like the ECAL, a barrel of 12 modules, and two endcaps consisting of six modules each (as shown in Figure 2.12). The barrel of the HCAL is 6.3 m long, centered at the IP, and extends in radius from 3.0 m to 4.7 m. The endcaps extend from 45 cm to 435 cm from the beam axis. The HCAL is rotated with respect to the ECAL by 32.7 mrads (1.875°) in order to avoid overlapping cracks. Each module consists of 23 plastic streamer tubes separated by 22 iron slabs (5 cm thick) corresponding to a total of 7.16 nuclear interaction lengths at 90°. The streamer tubes, working beyond the proportional region, provide a two-dimensional pattern (in r and ϕ) of yes/no signals with 1 cm granularity in ϕ. The energy and position is measured capacitively by pads organized in projective towers. Twenty-three pads pointing to the interaction point form a tower covering $3.7° \times 3.7°$, which contains on average 14 ECAL towers. The energy resolution for pions at normal incidence is given by:

$$\frac{\sigma_E}{E} = \frac{84\%\sqrt{\text{GeV}}}{\sqrt{E}} \, . \tag{2.6}$$

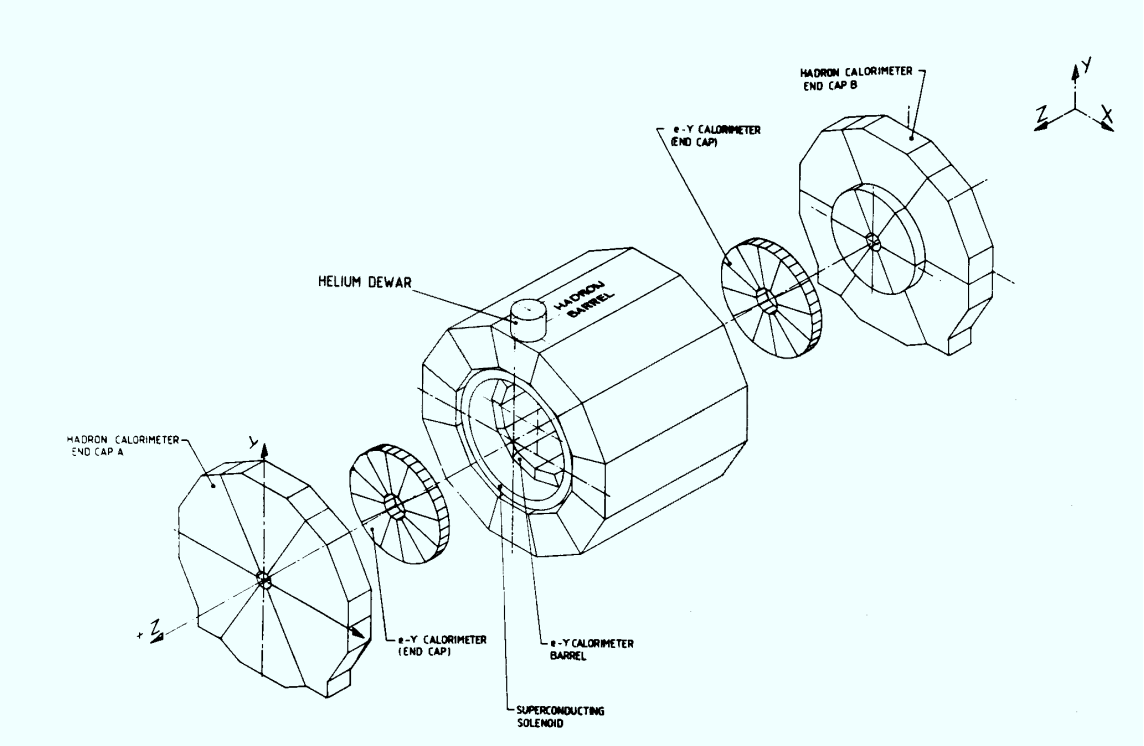

Figure 2.12: *The HCAL.*

Muon identification is achieved by detecting a pattern in the streamer tubes. In addition, there are two additional layers of streamer tubes oriented perpendicularly to each other outside the HCAL. They give the direction and position of muons passing through the HCAL.

For photon only final states the HCAL is essential in identifying muons from cosmic rays that can fake a photon signal in the ECAL. In addition, when a photon candidate enters the ECAL inter-module cracks or where the ECAL barrel and endcaps come together the photon shower often leaks into the HCAL. The HCAL energy

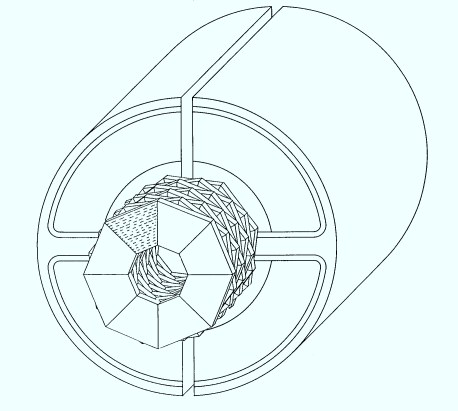

Figure 2.13: *The luminosity monitors.*

in this region is added to the photon energy measured in the ECAL to obtain the final photon energy. This is discussed in more detail in Section 2.12.

2.11 Luminosity Monitors

The luminosity measurement of the colliding electron and positron beams is performed by two calorimeters, the LCAL and SiCAL (shown in Figure 2.13). The dimensions of each detector are detailed in Table 2.2. Each calorimeter has two elements, one on each side of the beam-pipe. They both detect Bhabha events at small scattering angle θ. The advantage of having the detectors at low angle is two-fold. The Bhabha cross section scales as $1/\theta^4$, thus high statistics are achieved. In addition, the cross section is well understood in this region from Quantum Electrodynamics

Parameter	LCAL	SiCAL
Distance from IP (cm)	262	250
Inner radius (cm)	10	6
Outer radius (cm)	52	15
Active angle $\theta_{\min}$ (mrads)	45	34
Active angle $\theta_{\max}$ (mrads)	160	58

Table 2.2: *Dimensions of the luminosity monitors.*

(at low polar angles the interference between the s-channel and t-channel diagrams is negligible).

The luminosity is given by the number of events detected divided by the cross section. The cross section in lowest order at small angles is

$$\frac{\mathrm{d}\sigma}{\mathrm{d}\Omega} = \frac{16\alpha^2}{s}\frac{(\hbar c)^2}{\theta^4} \tag{2.7}$$

where α is the fine structure constant, s is the center-of-mass energy squared, $\hbar$ is Planck's constant, c is the speed of light and θ is the polar angle. Integration over the acceptance gives:

$$\sigma^{\mathrm{acc}} = \frac{1040}{s(\mathrm{GeV}^2)}\left(\frac{1}{\theta^2_{\min}} - \frac{1}{\theta^2_{\max}}\right)\mathrm{nb} \tag{2.8}$$

Table 2.3 details the luminosity recorded for the 1996 run. For this thesis, the small amount of luminosity obtained at 170 GeV is always included in the 172 GeV data unless otherwise stated. The LCAL and SiCAL also measure energy, thus increasing the detector acceptance down to 34 mrads. The luminosity calorimeters (LCAL and SiCAL), together with the hadron calorimeter (HCAL), are used to veto events in which photons are accompanied by other energetic particles at low polar angles.

$\sqrt{s}$ (GeV)	luminosity ($pb^{\perp 1}$)	sigma(stat.)	sigma(syst.)
161.0	10.740	0.043	0.062
161.2	0.339	0.008	0.002
170.0	1.114	0.015	0.006
172.0	9.536	0.045	0.054

Table 2.3: *The luminosity recorded in the 1996 data taking with the ALEPH detector.*

The LCAL consists of two halves which fit together around the beam axis; the area where the two halves join is a region of reduced sensitivity ('the LCAL crack'). There are four LCAL cracks in total, two on each side of the detector, above and below the beam pipe. This vertical crack is only partially covered by the HCAL and SiCAL. The LCAL crack accounts for only 0.05% of the total solid angle coverage of the ALEPH detector, but because it is located at low polar angles the process $e^+e^{\perp} \rightarrow e^+e^{\perp}(\gamma)$, where the final state electron and positron enter the LCAL cracks, leaving the photon as the only detected particle, poses a background for the EW process. Additional selection criteria are required in the EW analysis to 'close off' the LCAL cracks.

2.12 Definition of a reconstructed photon

Photon candidates are identified using an algorithm [40] which performs a topological search for localized energy depositions (a cluster) within groups of neighboring ECAL towers with significant energy deposition. To take advantage of the compact nature of electromagnetic showers and of the projected geometry of the ECAL, two

storeys are considered neighbors only when they share a common face. The cluster is required to have transverse and longitudinal profiles consistent with that of an electromagnetic shower. The clusters found by the algorithm are retained as candidate photons if their energy is greater than 0.25 GeV and if there is no charged track impact at a distance of less than 2 cm from the projecting towers of the cluster barycenter.

Figure 2.14 is an event display of a one-photon EW event (one photon and nothing else detected in the event). The θ-ϕ view (large box) shows a close up of the photon cluster. Each rectangular box represents an ECAL tower and the amount of energy contained in each tower is indicated by how much the rectangular box is filled in.

The same algorithm used to identify photons in the ECAL also finds the energy and position of the photon candidate by considering the four central towers. The four central towers are defined as the four neighboring towers with the most energy. The photon energy is computed from the energy in the four central towers of the cluster and the expected value of the fraction of energy in the four towers. In Figure 2.14 only the four towers with the most energy (the four rectangular boxes that are most filled in) are used to calculate the energy and position. This method has the advantage of eliminating tails in the energy and position measurements due to clustering effects and detector noise. The energy resolution is slightly degraded to

$$\frac{\sigma_E}{E} = \frac{0.25}{\sqrt{E}(\mathrm{GeV})} + 0.009 \ . \tag{2.9}$$

The angular resolution for an isolated cluster reconstructed in this manner remains

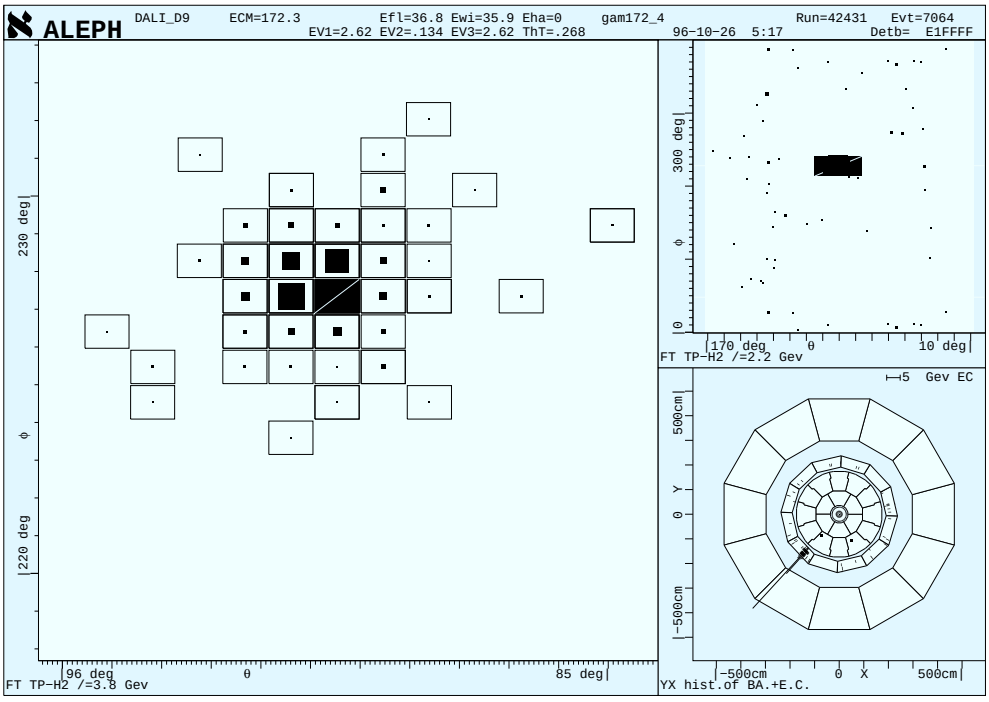

Figure 2.14: *an event display of a typical ECAL cluster from a one-photon event ($\theta - \phi$ view). Note that the energy of the cluster is almost fully contained in the four central towers. The full θ-ϕ view and the x-y view are shown in the upper and lower right, respectively. The x-y view shows the cross section of the detector. The photon is completely contained in the ECAL (as seen in the x-y view).*

the same as that in equation 2.5.

Photon candidates may also be identified in the tracking system if they convert producing an electron-positron pair [41, 39]. About 5% of the photons within $|\cos\theta| < 0.95$ convert in the material of the detector producing an electron-positron pair, identified as follows. Both tracks must be reconstructed and have opposite charge. One of the tracks must be identified as an electon [39, 42]. Then a photon conversion pair finding algorithm is used with the following cuts:

- The distance in the x-y plane between the two tracks at the closest approach to the materialization point must be less than 1 cm.
- The z separation of the two tracks at the closest approach to the materialization point is required to be less than 1 cm.
- The invariant mass of the track pair at the materialization point is less than 50 MeV/c^2
- The materialization point must be at least 5 cm from the beam axis.

The materialization point is found by doing a three dimensional vertex fit on the charged tracks without kinematic constraints. Figure 2.15 shows an event display of a photon conversion. Once identified, a reconstructed conversion is treated exactly like a photon. This definition of a photon is used throughout the paper.

Photons that enter near the ECAL inter-module cracks or in the gap region between the barrel and one of the endcaps often have a poor energy measurement.

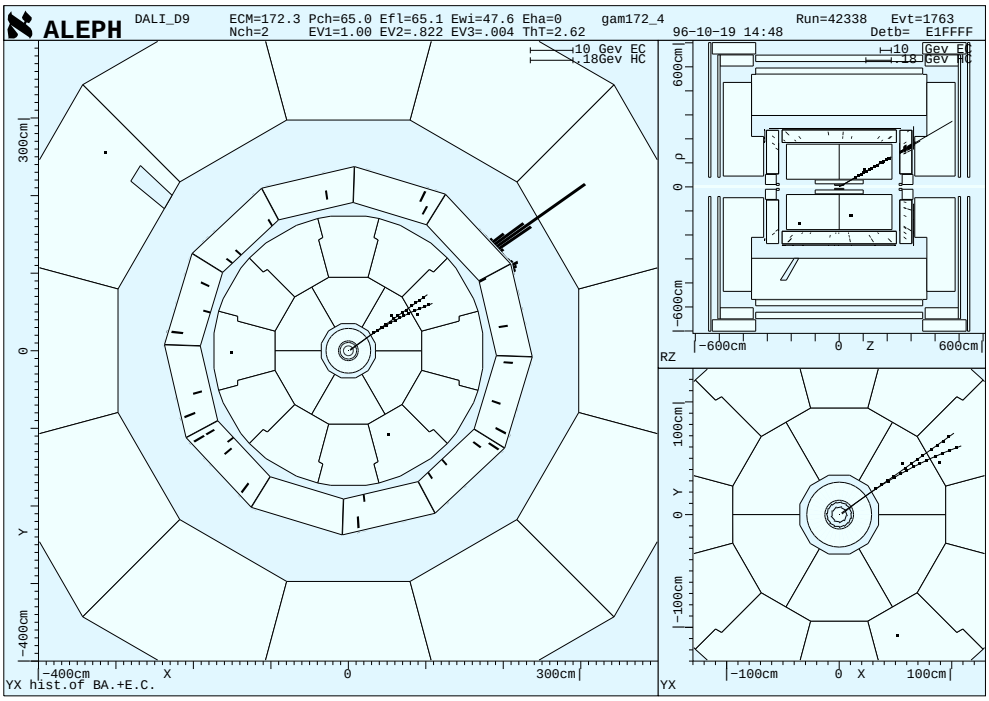

Figure 2.15: *A photon that converted in the inner wall of the TPC is shown in the x-y view (large box), the r-z view (upper right) and again in the x-y view (lower right) where only the tracking chambers are shown.*

Bhabha events ($e^+e^\perp \rightarrow e^+e^\perp$) from the 1995 run at the Z peak were used to study the cracks of the ECAL. Figure 2.16 shows the energy of the ECAL cluster versus polar and azimuthal angle. Since these are Bhabha events at the Z peak the nominal energy should be 45.6 GeV. Due to initial state radiation the average energy is reduced a few GeV. A drop in energy is observed in the polar and azimuthal angles corresponding to the gap region and inter-module cracks, respectively. The inter-module cracks are at different azimuthal angle for the barrel and endcap. Energy reconstruction is optimized by identifying these low sensitivity regions and correcting for energy leakage into the HCAL. Photons far from ECAL cracks have their energy measured solely from the localized energy deposition. Photons that are not well-contained in the ECAL (in a crack or gap region) have their energy measured from the sum of the localized energy depositions and all energy deposits in the HCAL within a cone of $\cos\alpha > 0.98$. Figure 2.17 shows the energy versus angle for the same data but with the addition of HCAL energy for electrons not well-contained in the ECAL. The energy measurement is much improved.

2.13 Neutral Trigger

The trigger most relevant for photon events is the neutral trigger. The neutral trigger for the 1996 running is 0.95 GeV total wire energy in a module for the barrel of the ECAL or 2.09 (2.30) GeV total wire energy in a module for endcap A (B) of the ECAL. This energy threshold has a negligible effect on all the analyses to be

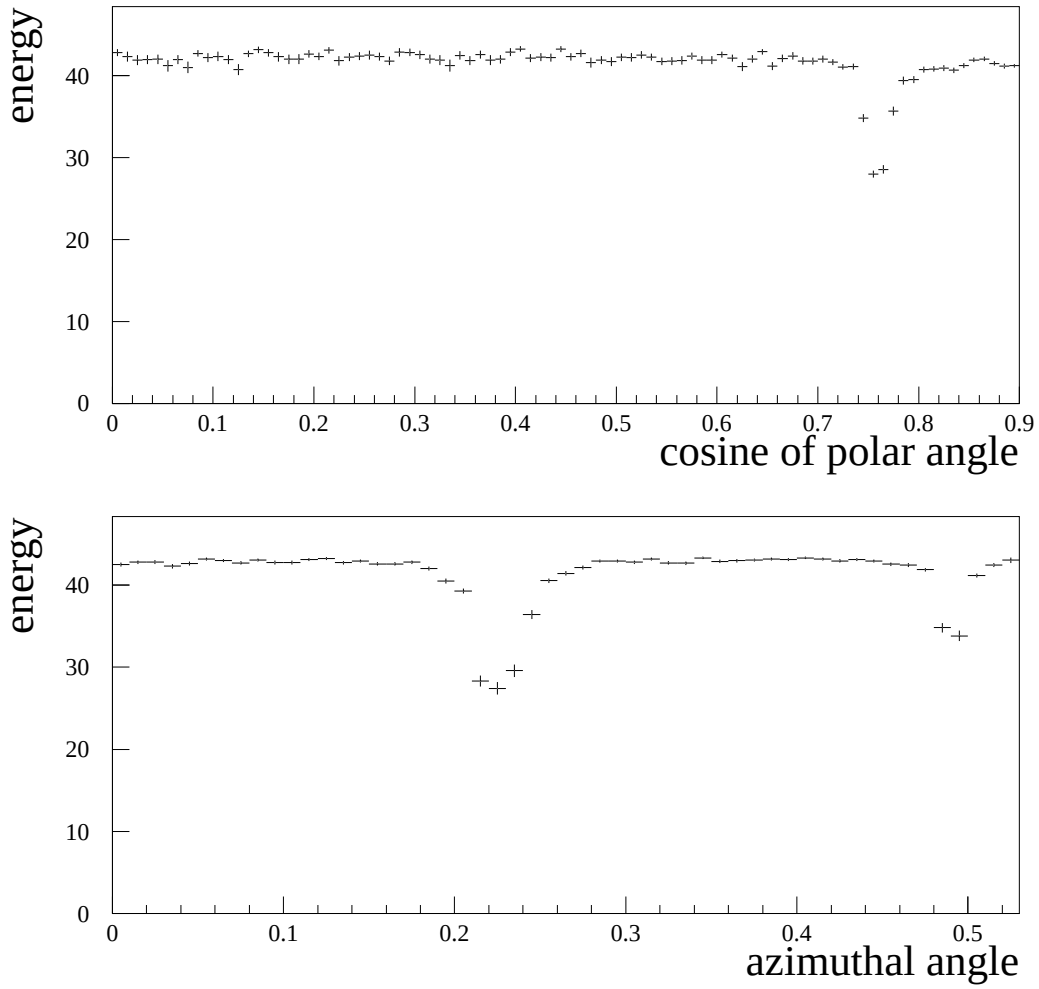

Figure 2.16: *The average energy (in GeV) vs. angle of Bhabha electrons from the 1995 Z peak running. The energy is clearly mismeasured in the gap region (centered at approximately* $|\cos\theta| = 0.75$*) and the inter-module crack region (centered at azimuthal angle 0.23 and 0.49 for the endcaps and barrel, respectively). The azimuthal angle is in radians and plotted for one module. One ECAL module covers 0.52 rads. The ECAL cracks in* ϕ *are symmetric for both the barrel and endcap modules.*

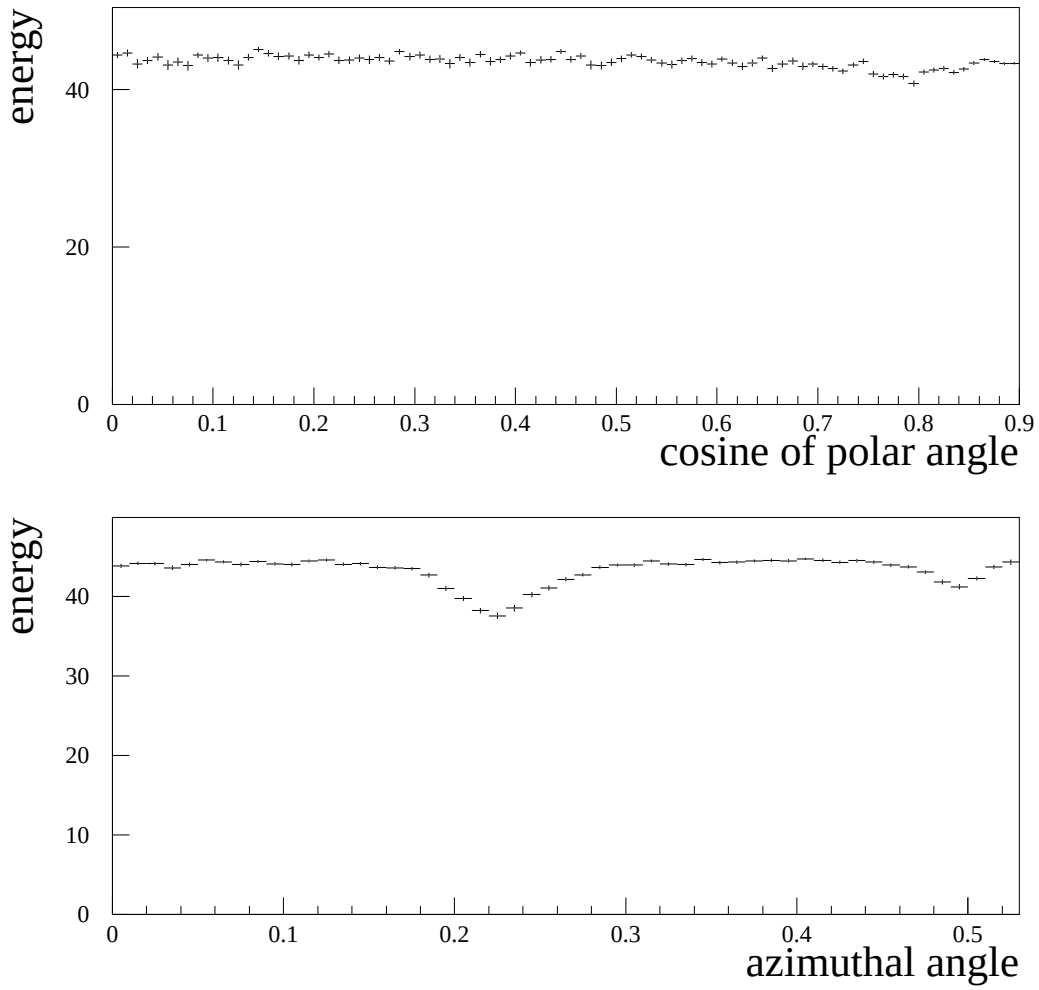

Figure 2.17: *The average energy (in GeV) vs. angle of Bhabha electrons from the 1995 Z peak running. The HCAL energy is included in the gap and inter-module crack regions. The energy measurement is clearly improved.*

described.

2.14 The Monte Carlo samples

Modern high-energy physics experiments rely on detailed simulation of both particle level interactions and the detector response to these reactions. The calculations for both particle interactions and the detector response are valid only for large statistics. Because these simulations rely on random processes, they are termed *Monte Carlo*. The Monte Carlo process begins by simulating the electron-positron collision. A *generator* is responsible for accurately predicting the particle interaction of interest. The user sets the initial conditions (type of process, $\sqrt{s}$, etc.) and, using a random number generator, the program outputs events which contain the 4-momenta of the final state particles. The 4-momenta of the final state particles obtained from the generator program are then passed through the detector simulation and detector reconstruction programs [41]. Monte Carlo programs are extremely helpful in designing the selection criteria for a given process. In addition, Monte Carlo is used to estimate the efficiency for the selection criteria, the Standard Model cross-section predictions and the background estimates.

While modern Monte Carlo programs are extremely detailed and accurate, they are not perfect. Therefore any opportunity to make a measurement or correction which does not require Monte Carlo simulation is exploited. In addition, a measurement or correction depending on Monte Carlo simulation is double checked.

The efficiency for the $e^+e^\perp \to \nu\bar{\nu}\gamma(\gamma)$ cross section measurement and the background for the anomalous photon plus missing energy searches are estimated using the KORALZ Monte Carlo program [43], for which 1988 $pb^{\perp 1}$ at $\sqrt{s} = 161$ GeV and 3106 $pb^{\perp 1}$at $\sqrt{s} = 172$ GeV were generated and fully reconstructed. This Monte Carlo is checked by comparing to the NUNUGG [44] generator at $\sqrt{s}$ below the $W^\pm$ threshold and to the CompHEP [45] generator at higher energies. The Monte Carlos agree within errors to 1% for the emission of one photon. The background estimate for the acoplanar-photon search from the KORALZ Monte Carlo program is checked by comparing to the CompHEP Monte Carlo program. Large samples of both programs were generated at $\sqrt{s} = 172$ GeV. The acoplanar-photon signature is checked for loose acceptance cuts ($E_\gamma > 5\,\mathrm{GeV}$, $|\cos\theta| < 0.95$) and in a more restrictive region ($\mathrm{Missing\,Mass} > 100\,\mathrm{GeV}/c^2$). The discrepancy between KORALZ and CompHEP is at the 10% level [46]. Shown in Figure 2.18 is the integrated cross section for the EW process as a function of the cut on the second most energetic photon for both the KORALZ and CompHEP programs.

To calculate the expected cross section and estimate the efficiency for the $e^+e^\perp \to \gamma\gamma(\gamma)$ process the order α^3 Monte Carlo by Berends and Kleiss [47] is used. 1306 $pb^{\perp 1}$ at $\sqrt{s} = 161$ GeV and 1038 $pb^{\perp 1}$at $\sqrt{s} = 172$ GeV were generated. The correction to the total cross section from order α^4 and higher effects is estimated to be less than 1% [48]. The effect on the efficiency is completely negligible.

The Bhabha generator [49] is used to compare with Bhabha events selected in the data. Bhabha events are helpful in studying the ECAL. In addition, the com-

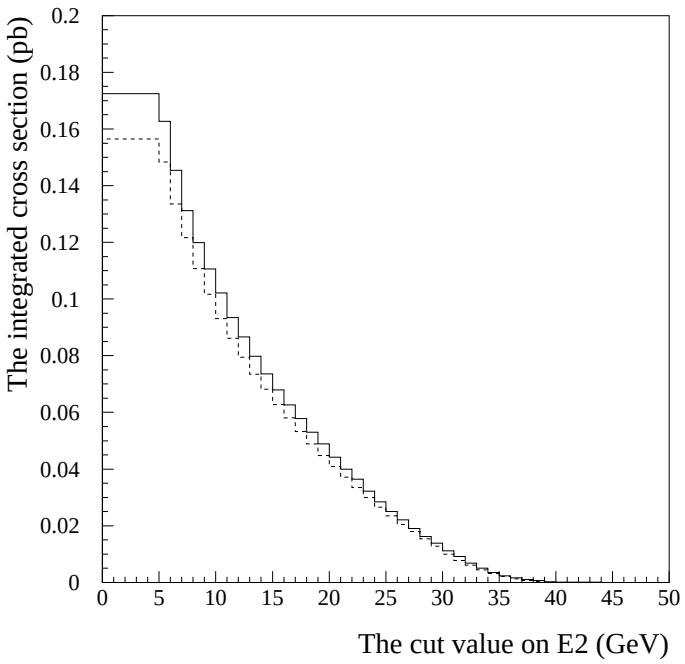

Figure 2.18: *The integrated cross section for the EW* $e^+e^\perp \to \nu\bar{\nu}\gamma\gamma(\gamma)$ *process at* $\sqrt{s}$*=172 GeV as a function of the cut value on the second most energetic photon for the CompHEP (solid histogram) and KORALZ programs (dashed histogram).*

parison of reconstructed Bhabha events in the data to reconstructed Monte Carlo events is used to test the detector simulation program. Background to the photon(s) plus missing energy signature can come from $e^+e^- \to e^+e^-(\gamma)$ (a Bhabha event with a Bremsstruhlung photon) events where initial or final state particles radiate a photon and the final state particles escape along the beam direction undetected. This background is studied using a different generator, the BHWIDE [50] Monte Carlo program.

The generator used for simulating supersymmetric events is SUSYGEN [51]. This Monte Carlo is used to design the selection criteria and evaluate the efficiency for the searches for Supersymmetry. In addition to SUSYGEN, a toy Monte Carlo, was developed for the photon(s) and missing energy topology. The toy Monte Carlo simulates the relatively simple kinematics of the supersymmetric processes studied in this thesis. The toy Monte Carlo does not include initial state radiation and therefore is always used in conjunction with SUSYGEN. The toy Monte Carlo allows the speedy calculation of efficiency over a wide range of mass points.

Chapter 3

The EW process $e^+e^- \to \nu\bar{\nu}\gamma(\gamma)$

The EW process consists of the Feynman diagrams shown in Figure 1.1. The weakly interacting neutrinos generally escape undetected leaving the bremsstrahlung photon (or photons for the higher order diagrams) as the only detected particle. The signal, as seen in the detector, is one or more photons and a large amount of missing energy (carried off by the undetected neutrinos). As explained in Chapter 1, the photons are bremsstrahlung photons from the incoming electron or positron. The chance of two photons being bremsstrahlung is reduced by an order α; therefore, EW events are predominantly events with a single photon and missing energy. Because of the huge cross section for Z production, the majority of these events have a missing mass at the Z mass.

3.1 Event selection criteria

This type of signal, an isolated pocket of energy in the ECAL and nothing else in the detector, is susceptible to background not originating from the beam collision. Cosmic rays from space and noise in the ECAL (a spark on the wires for example) can fake the signal. Because the detector is approximately 200 meters underground, it is well shielded from all cosmic particles except muons and neutrinos, which interact weakly with matter and have long lifetimes. The neutrinos almost always pass through the detector without leaving a trace, posing no problem. The muons, however, bremsstrahlung photon(s) as they traverse the detector. However, because muons are charged particles, they are easily spotted in the tracking chambers (ITC and TPC) and/or the HCAL if they traverse the detector. The event is then eliminated by requiring no charged tracks in the ITC and TPC and less than four fired streamer tubes in the outer region of an HCAL module.

Cosmic muons that traverse only the ECAL and bremsstrahlung a photon are a little more tricky to eliminate. However, the ECAL information can be exploited to remove these types of events. Bremsstrahlung photons are generally emitted in the same direction as the particle emitting them. A photon emitted by a muon that does not traverse the tracking chamber will not in general point to the Interaction Point (IP). The photon of an EW event comes from the IP. By finding where the photon 'points' in space, the photon impact parameter is found and the signal can be distinguished from background. The barycenter (the center of gravity of the energy

for an ECAL cluster) of the photon shower is found in each of the three ECAL stacks. Taking two points at a time, three possible photon trajectories are calculated and used to estimate the distance of closest approach in space of the photon to the interaction point. The minimum of the three estimated distances of closest approach is called the photon impact parameter. The cut on the photon impact parameter is determined using data events from the QED selection criteria (to be discussed in Chapter 5) and is required to be less than 25 cm (as shown in Figure 3.1), approximately 4 sigma of the resolution. Shown in Figure 3.2 is the photon impact parameter distribution for data and KORALZ Monte Carlo events that pass the EW selection criteria (excluding the photon impact parameter cut). After the no charged track, HCAL pattern and photon impact parameter cuts no cosmic ray events are left in the data, as verified by scanning the events.

Detector noise events are usually quite dramatic, as shown in Figure 3.3. These events fire many storeys with roughly equal energy resulting in very wide clusters. Real photon events have showers that typically span only a few storeys with the energy concentrated in the middle resulting in compact clusters (as shown in Figure 2.14). A cluster width is calculated by taking an energy-weighted average of the angular deviation from the cluster barycenter of each of the ECAL storeys contributing to the cluster. The cluster width is defined as

$$Cluster\ width = \frac{1}{\mathrm{E}_{total}} \sum_{i}^{\mathrm{N}_{st}} \theta_{iB} \mathrm{E}_i \tag{3.1}$$

$$\theta_{iB} = \arccos\left(\frac{\vec{x_i} \cdot \vec{d}}{\mid x_i \mid\mid d \mid}\right)$$

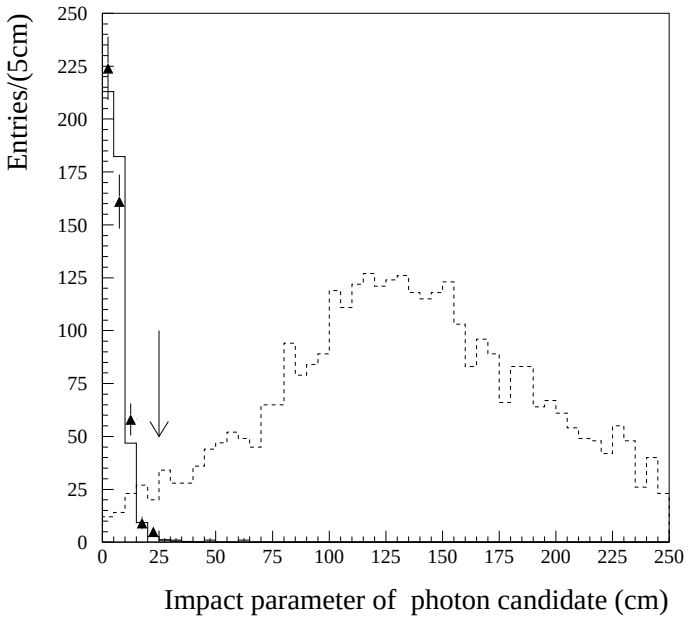

Figure 3.1: *The photon impact parameter of an ECAL object observed in data* $e^+e^\perp \to \gamma\gamma(\gamma)$ *events (triangles), in Monte Carlo* $e^+e^\perp \to \gamma\gamma(\gamma)$ *events (solid histogram) and in cosmic ray events (dashed histogram). The cosmic ray events are selected by requiring events that are not in time with the beam crossing and that have no charged tracks in the ITC and TPC. The Monte Carlo is absolutely normalized to the data; the cosmic ray events are arbitrarily normalized. The cut at 25 cm is indicated by the arrow.*

where $\vec{x_i}$ is the line from the IP to the i^{th} storey, $\vec{d}$ is the line from the IP to the barycenter, E_i is the energy of the i^{th} storey, E_{total} is the total energy of the cluster and N_{st} is the total number of the storeys that make up the cluster. The cluster width is required to be less than $0.85°$. This value for the cluster width cut results in negligible efficiency loss (less than 0.1%) for real photons and eliminates the remaining detector noise events.

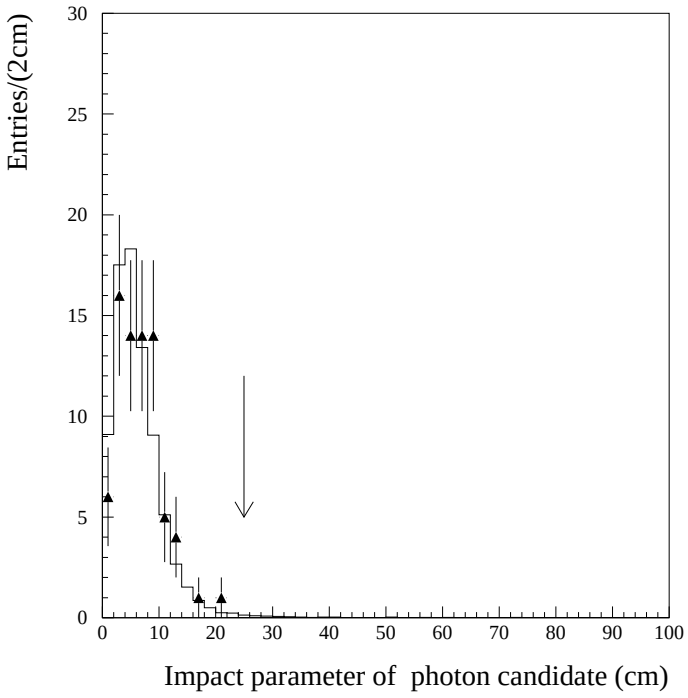

Figure 3.2: *The photon impact parameter of an ECAL object observed in data* $e^+e^\perp \to \nu\bar{\nu}\gamma(\gamma)$ *events (triangles) and in Monte Carlo* $e^+e^\perp \to \nu\bar{\nu}\gamma(\gamma)$ *events (solid histogram). The Monte Carlo is absolutely normalized to the data. The cut at 25 cm is indicated by the arrow.*

Finally, as both cosmic ray and detector noise events do not originate from the beam collision, their time of occurrence should not coincide with the beam crossing, except by pure coincidence. The interaction time relative to the beam crossing t_0 is taken from the ECAL modules. In order to optimize the t_0 performance for this analysis and to correct for the slower amplifiers in the 3rd stack, a sample of Bhabha events from the 1995 Z peak running was studied. Using this sample of events each module's t_0 is corrected to have zero offset. The modules in the barrel are all corrected by an 8 ns overall shift plus 80 ns times the fraction of total energy in the third stack

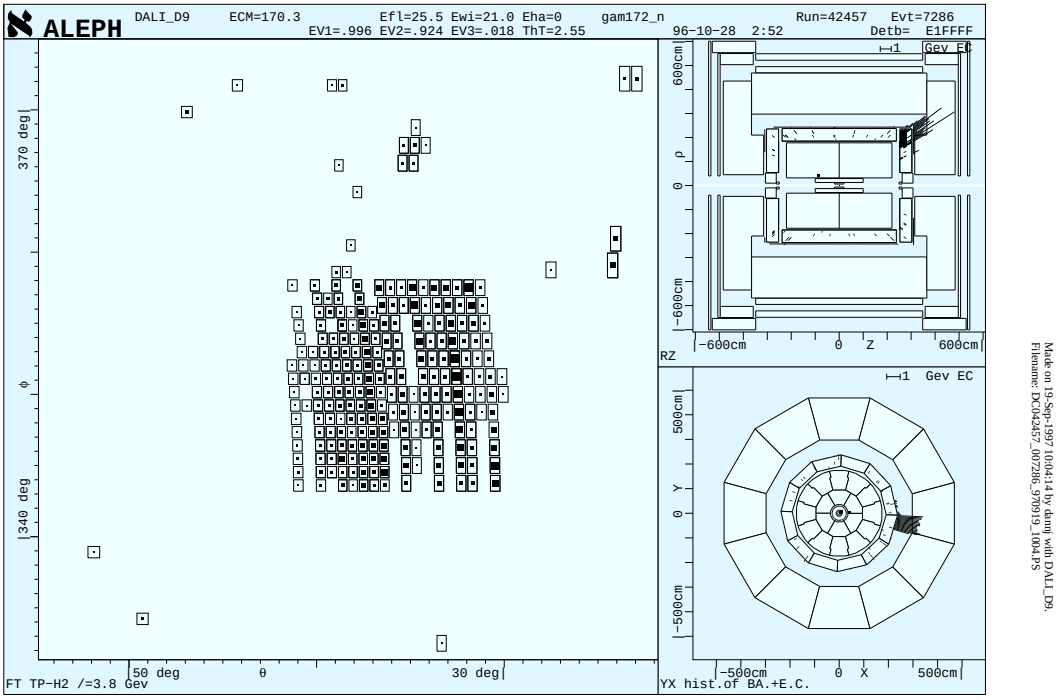

Figure 3.3: *A typical ECAL noise cluster (θ-ϕ view). The cluster is extremely wide and the energy is evenly dispersed among many storeys. Each cell represents an ECAL tower of at least 20 MeV in energy. The amount of energy deposited in each tower is indicated by how much it is filled in. On the right are the r-z (upper) and x-y (lower) views of the detector.*

of the ECAL. The corresponding corrections for the endcap modules amounts to an overall shift of 16 ns plus 60 ns times the fraction of energy in the third stack. The t_0 for the event is then found by taking the energy weighted average of the corrected t_0 's from all modules. A cut at $\pm$ 40 ns is applied (as shown in Figure 3.4). Note that in 1996, LEP sometimes ran in 'two bunch mode'. The beam of electrons and positrons sometimes had two bunches of particles at each point of collision. The second bunch was spaced 320 ns after the first.

The acceptance is a region of phase space (energy and polar angle) for which the detector efficiency is well-understood and well-modeled. The detector does not have full 4π coverage. At high $|\cos\theta|$ (low polar angle) there are no detectors (in order to allow the beam particles through) and, thus, no information. The cross section for the EW process is severely peaked at low energy and high $|\cos\theta|$. Therefore calculating the efficiency over the whole 4π (and obtaining a ridiculously small number over the polar angular range of the detector) is not interesting. A detector acceptance is defined for which the efficiency and cross section are well-understood. The polar angle acceptance is the range of polar angles for which the cross section is defined. For example, if the acceptance is $|\cos\theta| < 0.95$ then only photons in this angular range are counted in the calculation of the cross section. The cross section is thus defined as the production rate of $e^+e^\perp \to \nu\bar{\nu}\gamma(\gamma)$ events inside the polar angle acceptance of $|\cos\theta| < 0.95$. The detector cannot accurately measure infinitely small energies, so an energy acceptance is also defined for the measurement of the cross section. Both energy and polar angle acceptances are defined for the measurement of the EW cross

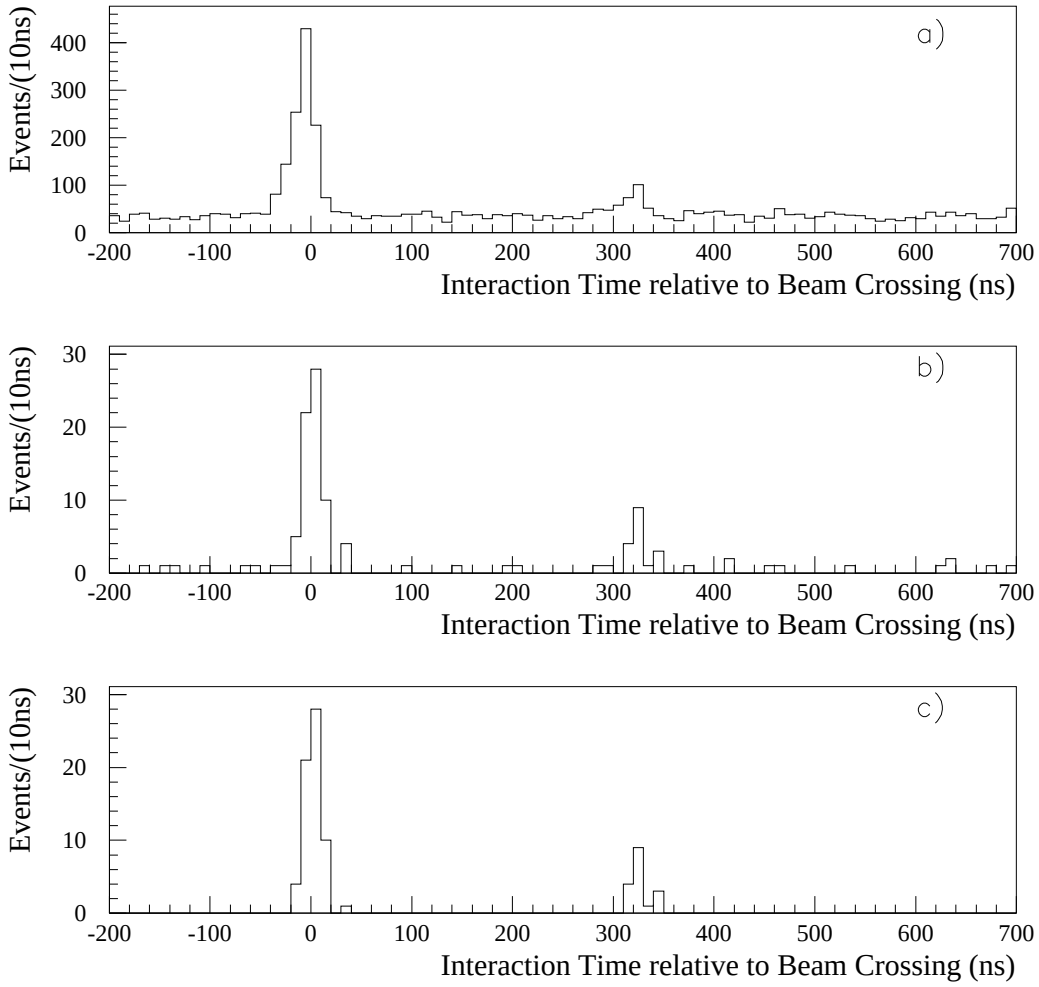

Figure 3.4: *The interaction time t_0 (in ns) relative to the beam crossing is plotted at three stages of the analysis. a) The t_0 is plotted for the 161 GeV and 172 GeV data with all EW selection criteria applied except the cosmic ray and detector noise cuts; the flat cosmic background is evident. b) Same as a) but including all the cosmic ray and detector noise cuts except the photon impact parameter and cluster width cuts. c) The t_0 is plotted with all cuts applied. The remaining events are all in time with the beam and, as verified from scanning the events, are all signal events. The second bunch centered at 320 ns is evident.*

section.

The photon acceptance for $\cos\theta$ and energy are $|\cos\theta| < 0.95$ and E > 1 GeV, respectively. In addition, a $p_\perp$ (the momentum transverse to the beam axis) requirement sufficient to reduce contamination from radiating events down the beam axis (for example, $e^+e^\perp \to e^+e^\perp(\gamma)$ where the electron and positron escape undetected down the beam axis) is included in the acceptance. The requirement $p_\perp > 0.0375\sqrt{s}$ is sufficient to force at least one of the beam particles into the detector [1]. These events are then eliminated by requiring that there be no charged tracks in the tracking chambers and the following cut. The event is rejected if the total energy (excluding photons) in the detector is more than 1 GeV or if there is any energy within 14° of the beam axis [2]. This requirement reduces the efficiency for $e^+e^\perp \to \nu\bar{\nu}\gamma(\gamma)$ by 7% due to additional bremsstrahlung photons at low angles. In addition, to compensate for gaps in the LCAL at azimuthal angles around 90° and 270° (Figure 3.5), a $p_\perp$ cut of $0.145\sqrt{s}$ is applied to events that have missing $p_\perp$ pointing to within ±17° of 90° or 270° in azimuthal angle (ϕ). This additional requirement on the $p_\perp$ of the photon is sufficient to force at least one of the beam particles into the HCAL [3].

The EW process with two or more photons occurs when the initial state particles bremsstrahlung additional photons. The corresponding cross section is reduced by

[1] It is assumed that, at most, the $p_\perp$ of the photon is shared by two particles. The active region for the detector extends down to 34 mrads from the beam axis. Applying momentum conservation to the worst case scenario where the $p_\perp$ of the radiated photon is shared equally by the two particles and accounting for energy resolution, the $p_\perp$ cut is set at $p_\perp > 0.0375\sqrt{s}$.

[2] 'Any energy within 14° of beam axis' really implies that no energy above the detector thresholds is recorded. The threshold used is 300 MeV for the LCAL and SiCAL and 40 MeV for the HCAL.

[3] Again, it is assumed that, at most, the $p_\perp$ is shared by two beam particles.

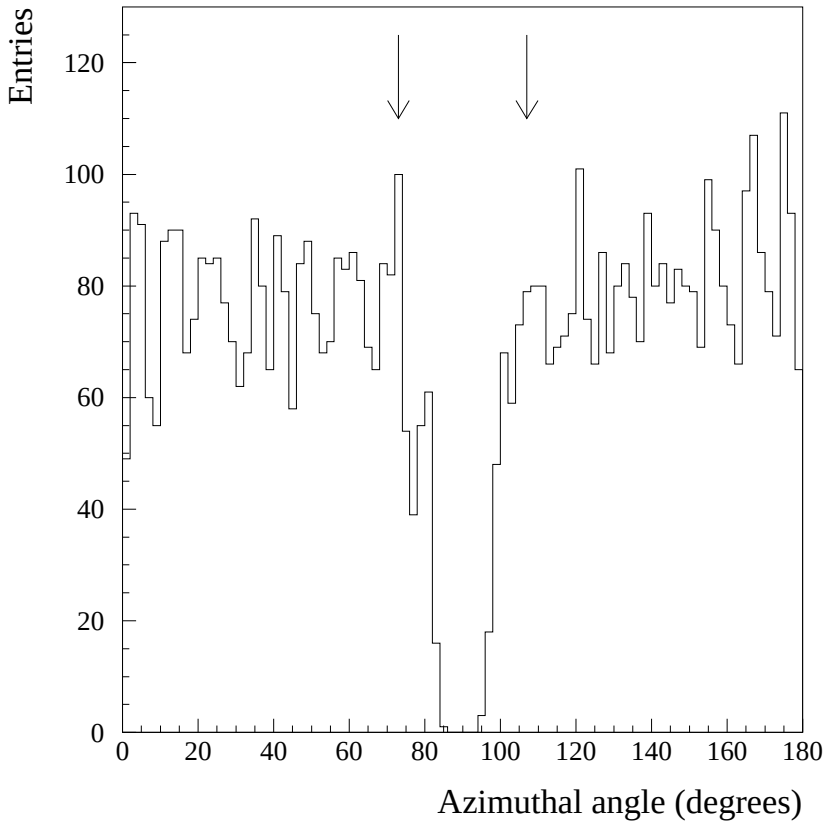

Figure 3.5: *Data obtained from the LCAL during the 161 GeV and 172 GeV runs is plotted. The sole selection criteria is that the object be of energy greater than 30 GeV. The considered range of the LCAL gap, centered at 90 degrees, is indicated by the arrows.*

an order α^n, where n is the number of additional photons. In order to eliminate contamination from the QED process (to be discussed in Chapter 5), predominately two back-to-back photons with the beam energy, additional cuts are applied. If there are two photons in the event the acoplanarity is required to be less than 170°. If there are more than two photons in the event the missing energy must be greater than $0.4\sqrt{s}$ in order for the event to be selected. The acoplanarity and missing energy distributions for both simulated EW and QED events are shown in Figure 3.6. The EW analysis proceeds as follows:

Acceptance:

- All photons are required to have $\mid \cos\theta \mid < 0.95$ and E > 1 GeV
- At least one photon is required to have $p_\perp > 0.0375\sqrt{s}$

Selection cuts:

- No charged tracks in the event that do not come from a conversion
- At least one photon is required to have $p_\perp > 0.145\sqrt{s}$ when the missing $p_\perp$ points to the LCAL crack
- The total additional visible energy must be less than 1 GeV
- No energy within 14° of the beam axis
- For two-photon events the acoplanarity is required to be less than 170°

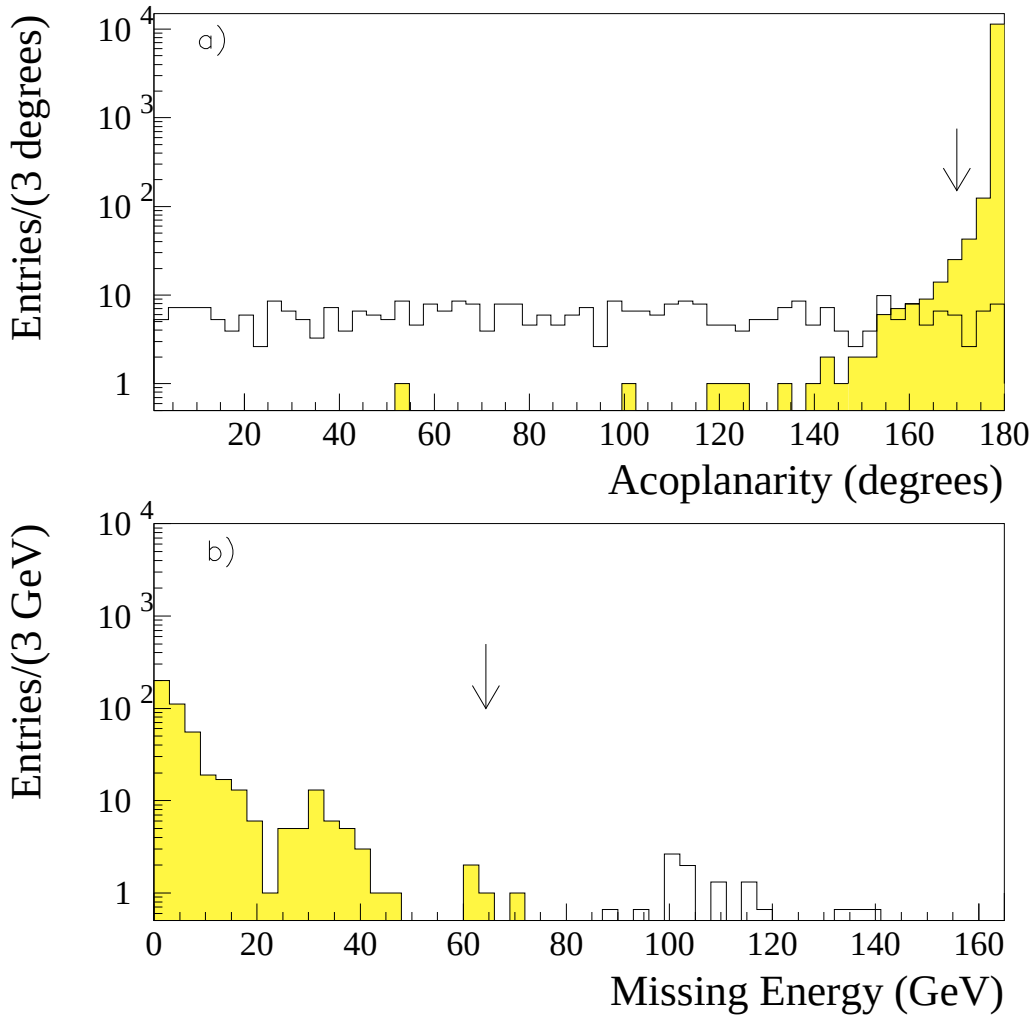

Figure 3.6: *The acoplanarity and missing energy distributions are plotted for simulated EW (solid histogram) and QED (hatched histogram) events at* $\sqrt{s} = 161\,\mathrm{GeV}$. *In a) the simulated events are plotted after the energy requirement for events with exactly two photons in the acceptance. In b) three or more photon events which pass the energy requirement are plotted. They are absolutely normalized to 1306* $\mathrm{pb}^{\perp 1}$. *The arrow indicates where the cut is made.*

Selection	Efficiency(%)	
	161 GeV	172 GeV
$N_\gamma \geq 1$ and $N_{ch} = 0$	94	94
$p_\perp > 0.145\sqrt{s}$ if $\phi_{pmiss} = 90 \pm 17$ or 270 ± 17	87	87
Additional energy < 1 GeV	80	80
No energy within 14° of the beam axis	79	79
Uncorrelated noise	76	77
All other cuts	75	76

Table 3.1: *The cumulative efficiency for the* $e^+e^\perp \to \nu\bar{\nu}\gamma(\gamma)$ *process inside the acceptance cuts.*

- Events with three or more photons are required to have a missing energy greater than $0.4\sqrt{s}$

Cosmic ray and detector noise cuts:

- The total number of HCAL fired layers in the 10 outermost layers of any given module is less than 4
- The photon impact parameter is within 25 cm of the IP
- The cluster width of the photon is less than 0.85°
- The measured t_0 from the ECAL wires is within 40 ns of the beam crossing

Residual cosmic ray and detector noise backgrounds are measured by selecting events slightly out of time with respect to the beam crossing but which pass all other cuts. No such events are found in a displaced time window of 740 ns width. Events with a radiated photon in the acceptance and the final state particles escaping undetected along the beam axis are studied using Monte Carlo for the $e^+e^\perp \to e^+e^\perp(\gamma)$

and $e^+e^\perp \to \gamma\gamma(\gamma)$ processes. The equivalent of 60 data sets of these Standard Model background processes was generated and passed through the full detector simulation. No events from these samples survive the selection.

3.2 Measurement of the $e^+e^- \to \nu\bar{\nu}\gamma(\gamma)$ cross section

The efficiency for the EW process $e^+e^\perp \to \nu\bar{\nu}\gamma(\gamma)$ is estimated using the KORALZ Monte Carlo, as shown in Table 3.1. The efficiency of the cosmic ray and detector noise cuts are checked using the QED two-photon sample. The efficiencies for the data and Monte Carlo QED events are in good agreement.

Efficiency for signal detection can also be lost by uncorrelated noise in the detector. For example, if a HCAL tube spuriously fires giving a reading of more than 1 GeV, the event is lost due to the requirement that the total energy excluding photons must be less than 1 GeV. This type of efficiency loss is not simulated in the Monte Carlo, so it must be found in another way. At random beam crossings the detector is turned on and the event recorded. These are called random trigger events. The percentage of these events that do not pass the additional energy less than 1 GeV and the no energy recorded within 14° of beam axis cuts give an estimate of the efficiency loss due to uncorrelated noise in the detector. In the 161 GeV data it is found that uncorrelated noise accounts for a 4% efficiency loss. For 172 GeV, the efficiency loss is 2%.

After all cuts, 41 one-photon events and two two-photon events are found at $\sqrt{s} =$ 161 GeV where 45 one-photon events and three two-photon events are expected from the Standard Model (calculated from the KORALZ Monte Carlo). At $\sqrt{s} = 172$ GeV, 36 one-photon events and one two-photon event are found where 37 one-photon events and two two-photon events are expected. No EW event of three or more photons is found in either data set. Inside the acceptance the corresponding cross-sections are

$$\sigma(\mathrm{e^+e^-} \to \nu\bar{\nu}\gamma(\gamma)) = 5.2 \pm 0.8 \pm 0.2\,\mathrm{pb} \quad \text{at} \quad \sqrt{\mathrm{s}} = 161 \quad \mathrm{GeV}$$

$$\sigma(\mathrm{e^+e^-} \to \nu\bar{\nu}\gamma(\gamma)) = 4.6 \pm 0.8 \pm 0.2\,\mathrm{pb} \quad \text{at} \quad \sqrt{\mathrm{s}} = 172 \quad \mathrm{GeV}.$$

These results are consistent with the Standard Model predictions of 5.8 ± 0.1 pb at 161 GeV and 4.9 ± 0.1 pb at 172 GeV. The missing mass and $\cos\theta$ distributions are shown in Figure 3.7. The goodness of fit for the $\cos\theta$ distribution is checked by doubling the bin size and calculating the χ^2. The χ^2 is found to be 4.5 for 10 degrees of freedom. The energy distribution is shown in Figure 3.8.

Estimates of the systematic uncertainty in these cross sections are shown in Table 3.2. The ability of the Monte Carlo to accurately simulate the selection efficiency for energetic photons is checked with a sample of Bhabha events selected using only tracking and muon chamber information. The tracking information was masked from these events and the photon reconstruction redone. The efficiency to reconstruct a photon in these events is found to be consistent within the available statistics between

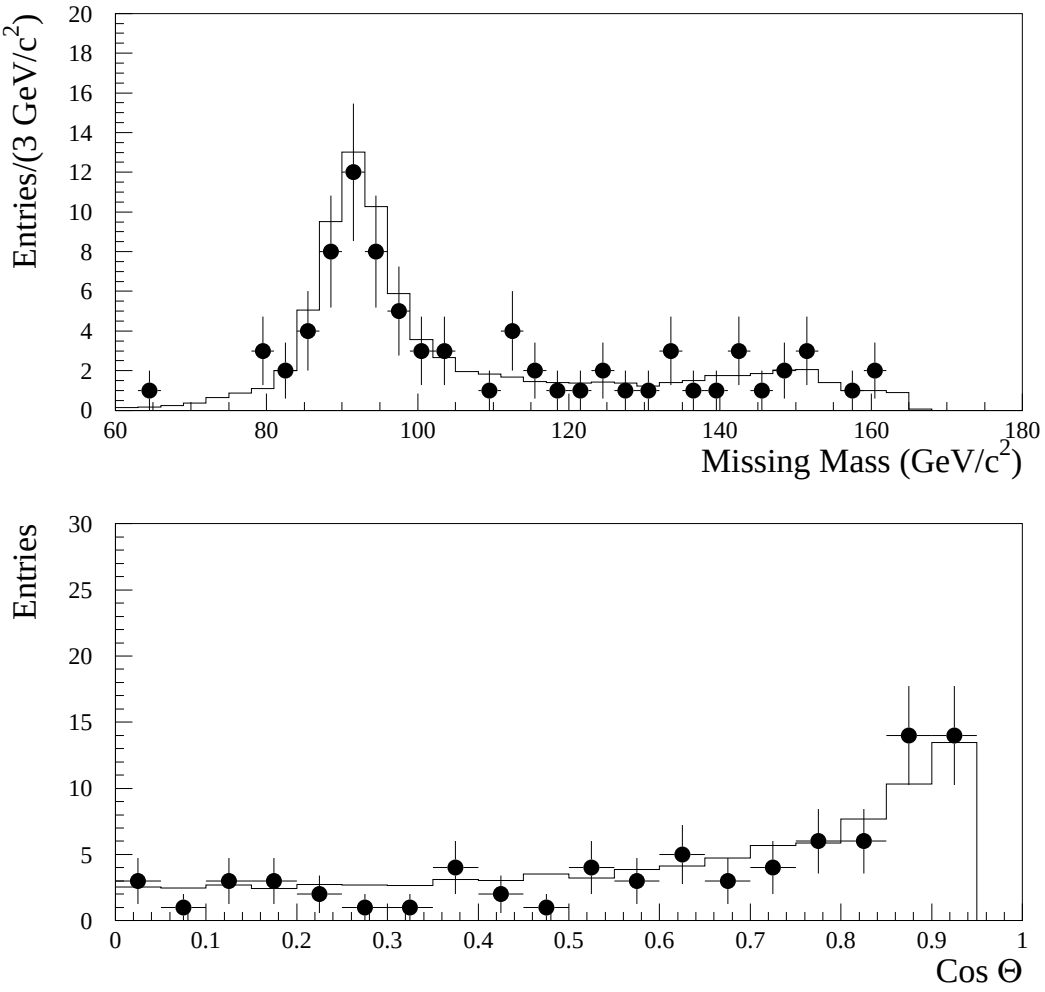

Figure 3.7: *a) The invariant mass distribution of the system recoiling against the photon(s) candidate is shown for both the data (with error bars) and Monte Carlo (histogram). b) The corresponding plot of the polar angle distribution of the photon candidate. The highest energy photon is taken for events with two or more photons. In both a) and b) the data and Monte Carlo from $\sqrt{s}$ = 161 GeV and 172 GeV are combined. The Monte Carlo is absolutely normalized to the data.*

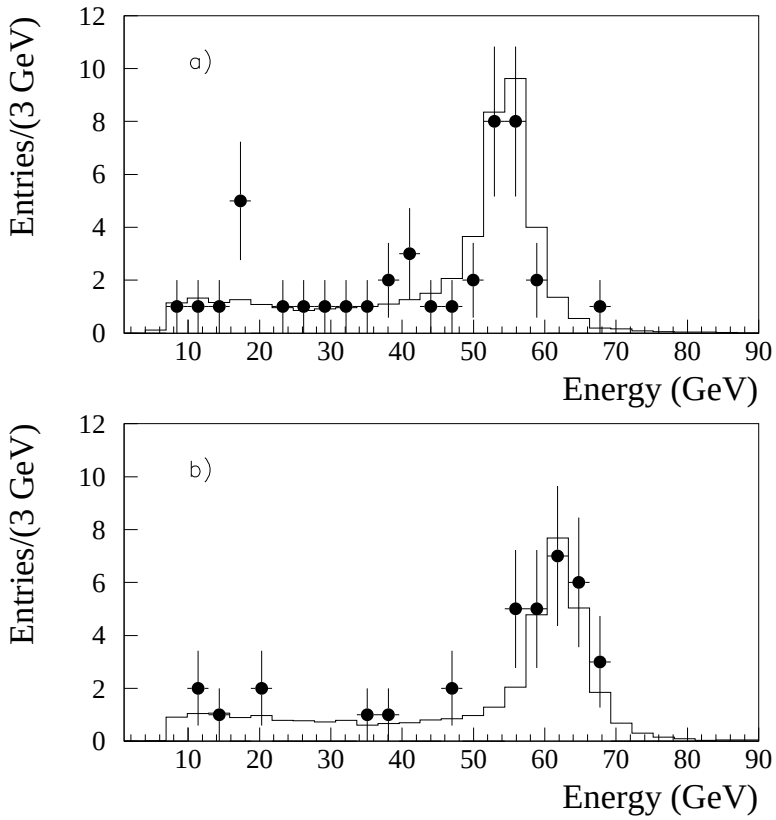

Figure 3.8: *The energy distribution of the photon candidate is shown for both the data (with error bars) and Monte Carlo (histogram). In a) the results after all cuts are shown for $\sqrt{s} = 161$ GeV. The data from $\sqrt{s} = 172$ GeV is shown in b). The Monte Carlo is absolutely normalized to the data. For events with two or more photons there is an entry for each photon in the event.*

Source	Error(%)
Photon selection	3
Converted photon selection	0.3
Energy calibration	0.2
Background	<1
Integrated luminosity	0.7
Monte Carlo theoretical	1
Monte Carlo statistical	0.4
Total (in quadrature)	4

Table 3.2: *Systematic uncertainties for the EW process.*

data and Monte Carlo simulation at the 3% level. The uncertainty in the number of simulated pair conversions is estimated in an approximate manner by adjusting the material thickness that is input into the detector simulation program by 50%. The efficiency is recalculated given the change in the number of simulated pairs. A 0.3% change is found in the overall efficiency. To account for the uncertainty in the energy calibration between data and Monte Carlo the photon energy is shifted by 2% in the Monte Carlo and the efficiency recalculated. The difference in the efficiency is found to be 0.2%. The error on the luminosity given by the LCAL is 0.7%. The efficiency estimate given by the KORALZ Monte Carlo program is checked by comparing to the NUNUGG Monte Carlo program. The efficiency estimates from the respective Monte Carlos agree within errors to 1%. Total systematic error is obtained by adding in quadrature the individual contributions.

3.3 Search for New Physics in the EW data

The total number of EW photon events agree with the total number expected from the Standard Model. The missing mass and polar angle distributions agree with the expected distributions. Thus, there is no evidence for new physics. In this section the EW data is used to set limits on the production of new physics. The topology of the new physics being searched for is a single photon and missing energy. Specific models relating to Supersymmetry (as discussed in Chapter 1) are used to set upper limits on the cross section. The upper limits on the cross section, however, are quite general and can be applied to other models with a similar topology.

Signal events from $e^+e^\perp \to \chi_1^0\tilde{G} \to \tilde{G}\tilde{G}\gamma$ are not easily separated from the EW events. Therefore a background subtraction procedure is applied. A simple subtraction of the total number expected from the total number observed in the data (using a proper statistical method) can be done to derive an upper limit. However, this crude method does not utilize all of the information. For example, the difference in the missing mass distribution between $e^+e^\perp \to \nu\bar{\nu}\gamma(\gamma)$ and $e^+e^\perp \to \chi_1^0\tilde{G} \to \tilde{G}\tilde{G}\gamma$ events can be exploited to improve the sensitivity of the experiment. A powerful method in determining how well one distribution agrees with an expected distribution is the likelihood function. In this case, the likelihood function is the conditional p.d.f. (probability distribution function) for a total number of signal events S, the

expected background $\vec{b} = (b_1, ..., b_n)$ and the data $\vec{x} = (x_1, ..., x_n)$, and is written [4].

$$\mathrm{L}(S|\vec{x}) = \prod_{i=1}^{\mathrm{N_{bins}}} \frac{\nu_i^{x_i}}{x_i!} e^{\perp \nu_i} \tag{3.2}$$

where

$$\nu_i = b_i + s_i \tag{3.3}$$

with

$$\sum_{i=1}^{\mathrm{N}_{bins}} s_i = S; \tag{3.4}$$

x_i is the number of entries in the i^{th} bin of the missing mass distribution for the data, b_i is the corresponding number of EW events expected in the i^{th} bin, and s_i is the corresponding number of signal events expected in the i^{th} bin assuming a total of S signal events. The value s_i is found by normalizing the missing mass distribution for signal events to the total number of signal events S. The likelihood as a function of S can be plotted by repeating the calculation of equation 3.2 for many different values of S.

The confidence level (C.L.) for the upper limit on the total number of signal events contained in the data can be obtained in many ways. The simplest and most direct method is the classical method. From the likelihood one can determine the number of signal events N_S such that the probability is 95% that the number of signal events S in the data is less than N_S (or conversely, at 95% C.L. the number of signal events in the data is less than N_S) by simply integrating the p.d.f.

$$0.95 = \frac{\int_{\perp\infty}^{S=N_S} \mathrm{L}(S|\vec{x})\mathrm{d}S}{\int_{\perp\infty}^{\infty} \mathrm{L}(S|\vec{x})\mathrm{d}S} \tag{3.5}$$

[4] Note that the overall normalization is automatically taken into account by this equation. This is often referred to as the extended likelihood.

The classical method has the problem that we are integrating the likelihood function (or p.d.f.) over negative values of S when we know a priori that $S \geq 0$. When the number of events in the data is less than the expected background the upper limit calculated from the above equation is unphysically optimistic. Another alternative is to report a Bayesian upper limit [52, 53, 54] given by (for 95% C.L.)

$$0.95 = \frac{\int_{\perp\infty}^{S=N_S} \mathrm{L}(S|\vec{x})\Pi(S)\mathrm{d}S}{\int_{\perp\infty}^{\infty} \mathrm{L}(S|\vec{x})\Pi(S)\mathrm{d}S}. \tag{3.6}$$

where $\Pi(S)$ is the prior density function. Here one has the advantage that prior knowledge of S can be incorporated into $\Pi(S)$. There is no unique way to specify $\Pi(S)$. We choose

$$\Pi(S) = \begin{cases} 0 & \text{if } S < 0 \\ \\ 1 & \text{if } S \geq 0 \end{cases} . \tag{3.7}$$

This choice is recommended by the Particle Data Group [PDG96]. It can be seen that, for this choice of $\Pi(S)$, the integrals begin at 0 and, therefore, negative, unphysical values of S are not integrated over. The Bayesian upper limit is found for the Supersymmetry processes $\mathrm{e^+e^{\perp}} \rightarrow \chi_1^0\tilde{\mathrm{G}} \rightarrow \tilde{\mathrm{G}}\tilde{\mathrm{G}}\gamma$ and $\mathrm{e^+e^{\perp}} \rightarrow \chi_2^0\chi_1^0 \rightarrow \chi_1^0\chi_1^0\gamma$.

3.3.1 Upper Limit on the Production $\mathrm{e^+e^-} \rightarrow \chi_1^0\tilde{\mathrm{G}}$

In gravitino LSP theories, if the gravitino mass is light enough ($\mathrm{M}_{\tilde{G}} < 10^{\perp 4}\,\mathrm{eV}/c^2$), the reaction $\mathrm{e^+e^{\perp}} \rightarrow \chi_1^0\tilde{\mathrm{G}} \rightarrow \tilde{\mathrm{G}}\tilde{\mathrm{G}}\gamma$ becomes accessible at LEP2 [24]. The hypothesis that there is a mixture of signal and EW events in the data is made. The method discussed in the previous section is then used to determine the upper limit (at 95%

C.L.) on the number of signal events contained in the one-photon data sample obtained with the EW selection criteria. This is then converted into an upper limit on the $e^+e^\perp \to \chi_1^0\tilde{G}$ cross section.

Events from the $e^+e^\perp \to \nu\bar{\nu}\gamma(\gamma)$ process and the $e^+e^\perp \to \chi_1^0\tilde{G} \to \tilde{G}\tilde{G}\gamma$ process have very different distributions in missing mass, as explained in Chapter 1 and illustrated in Figure 3.9. The likelihood that the data missing mass distribution agrees with the composite missing mass distribution of the Monte Carlo $e^+e^\perp \to \nu\bar{\nu}\gamma(\gamma)$ and the signal $e^+e^\perp \to \chi_1^0\tilde{G} \to \tilde{G}\tilde{G}\gamma$ reactions is calculated using equation 3.2. The likelihood vs. S (the total number of signal events) plot is shown in Figure 3.10. Following the Bayesian method (equations 3.6 and 3.7), the upper limit on the total number of signal events, N_S, is calculated by integrating the likelihood vs. S curve. The number of signal events is increased until the integration from $S = 0$ to $S = N_S$ of the likelihood is 95% of the total area (the integration from $S = 0$ to $S = \infty$), as shown in Figure 3.11. N_S is then the upper limit on the total number of signal events at 95% C.L. This procedure is repeated at each neutralino mass up to 171 GeV/c^2 stepping by 1 GeV/c^2 in mass.

A toy Monte Carlo with the kinematic cuts applied is used to describe the signal shape of the missing mass distribution at each neutralino mass. The SUSYGEN Monte Carlo program is run through the detector simulation program and used to estimate the additional efficiency loss due to ISR and photon reconstruction. The efficiency for a χ_1^0 of mass 80 GeV/c^2 is shown in Table 3.3. The efficiency for the signal process for neutralino masses above 40 GeV/c^2 is better than 70%.

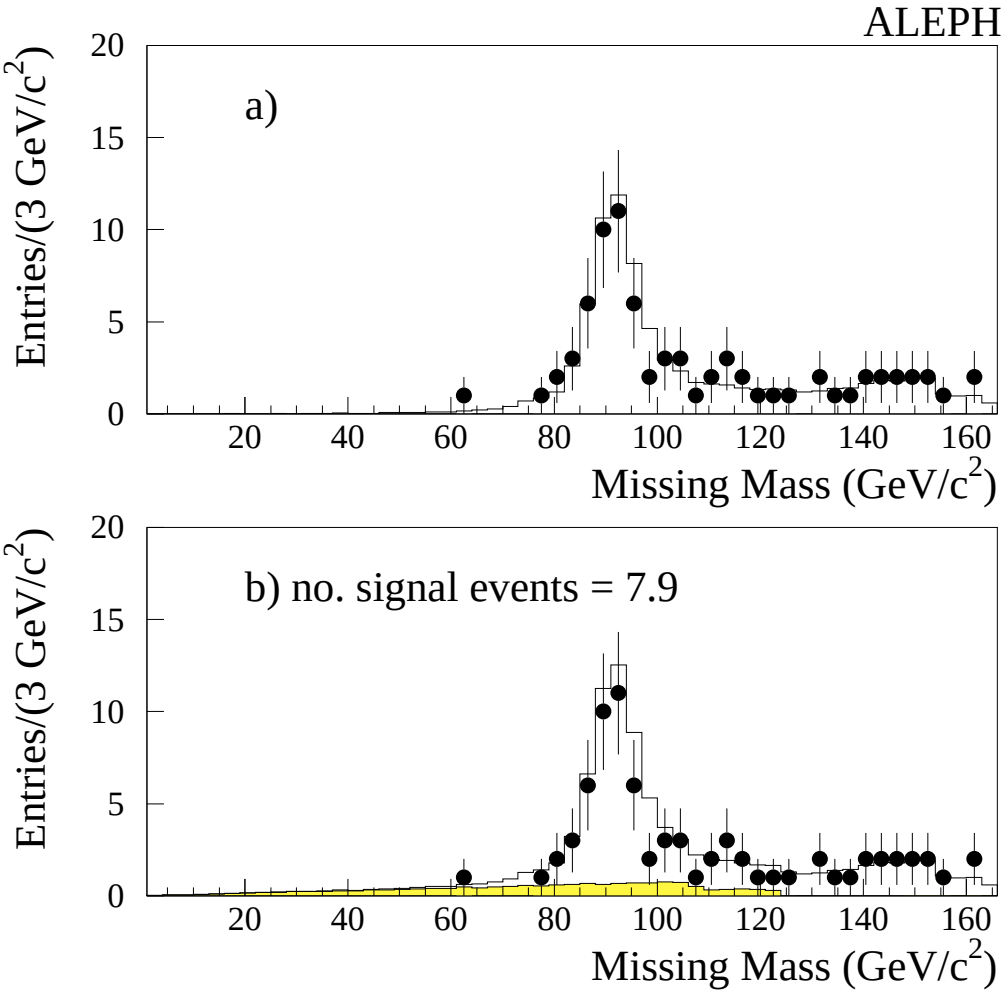

Figure 3.9: *a) The invariant mass distribution of the system recoiling against the photon candidate is shown for both the data (with error bars) and the EW process simulated by Monte Carlo (histogram). b) The invariant mass distribution of the system recoiling against the photon candidate is shown for the data (with error bars), the Monte Carlo simulation of the EW process plus the signal process (histogram) and the signal process (hatched histogram). The signal process* $e^+e^- \to \chi_1^0\tilde{G} \to \tilde{G}\tilde{G}\gamma$ *is plotted for a neutralino mass of 120 GeV. The area of the signal distribution is 7.9 events and the C.L. of the agreement between data and EW plus signal is 5%. Thus the upper limit on the number of signal events for a 120 GeV mass neutralino is 7.9 at 95% C.L.*

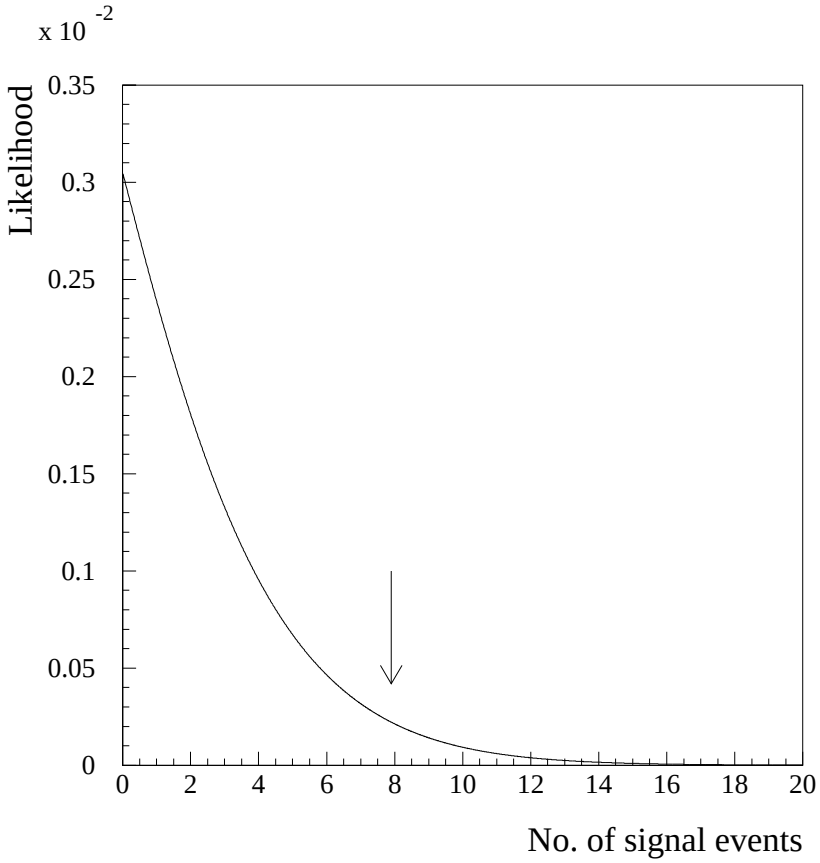

Figure 3.10: *The likelihood function (the p.d.f.) vs. the number of signal events for a 120 GeV mass neutralino. The arrow at 7.9 events indicates the 95% C.L. upper limit found in Figure 3.11.*

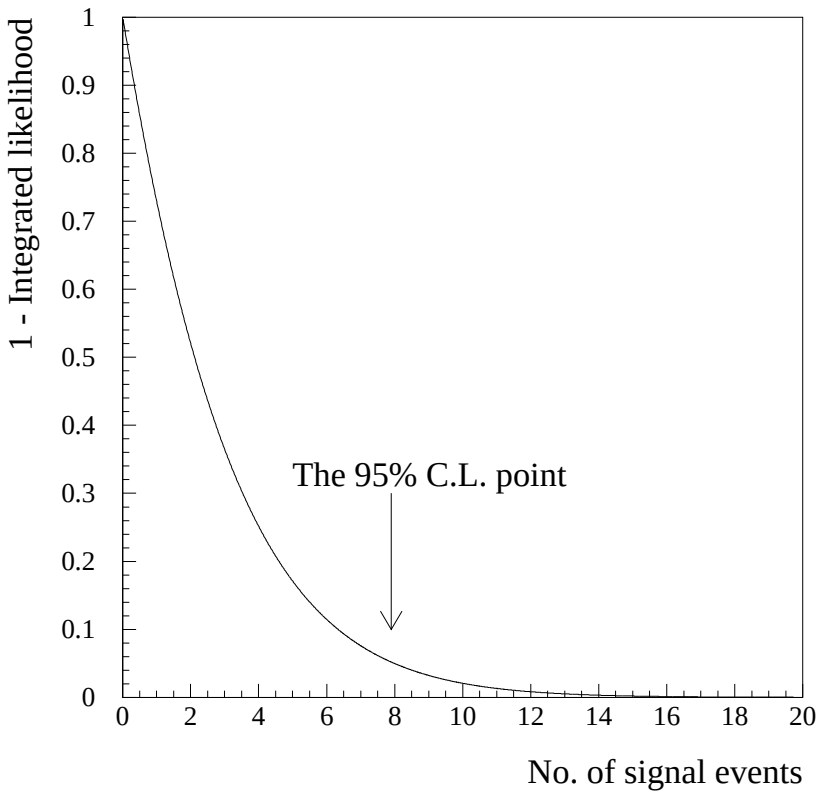

Figure 3.11: *The plot of 1 - the integrated likelihood function vs. the number of signal events for a 120 GeV mass neutralino.*

As reported in the EW section, 77 one-photon events are found in the combined data set of 1996 and 82 are expected from the Monte Carlo. The upper limit on the cross-section at 95% C.L. is given in Figure 3.12. Overlayed is the theoretical cross section for $e^+e^\perp \to \chi_1^0\tilde{G}$ for two different gravitino masses. A negligible neutralino lifetime is assumed. The luminosity of the two data samples is combined assuming β^8/s (with $\beta = \frac{s \perp M_\chi^2}{s+M_\chi^2}$) threshold dependence of the cross section. The systematic uncertainty is taken into account following Ref. [55], which changes the upper limit

Selection	Efficiency(%)
$N_\gamma = 1$ and $N_{ch} = 0$	90
Additional energy < 1 GeV	84
No energy within 14° of the beam axis	83
$\lvert\cos\theta\rvert < 0.95$ and $p_\perp > 0.0375\sqrt{s}$	79
$p_\perp > 0.145\sqrt{s}$ if $\phi_{pmiss} = 90 \pm 17$ or 270 ± 17	76
Uncorrelated noise	73
All other cuts	73

Table 3.3: *The cumulative efficiency for the* $e^+e^\perp \to \chi_1^0\tilde{G} \to \tilde{G}\tilde{G}\gamma$ *process for* χ_1^0 *mass of 80 GeV/*c^2 *at* $\sqrt{s}$*= 161 GeV.*

on the number of signal events by less than 1%.

In the LNZ model [24], for a gravitino mass of $10^{\perp 5}$ eV/c^2, the neutralino mass limit is 100 GeV/c^2. However, the cross section for this process scales as the inverse of the gravitino mass squared, so the limit on the neutralino mass is very sensitive to the assumed gravitino mass. The excluded region of neutralino mass vs. gravitino mass is shown in Figure 3.13.

3.3.2 Upper Limit on the Production $e^+e^- \to \chi_2^0\chi_1^0$

The upper limit for the $e^+e^\perp \to \chi_2^0\chi_1^0 \to \chi_1^0\chi_1^0\gamma$ process is obtained by repeating the procedure of the previous section but allowing for the LSP to have mass. Figure 3.14 shows the contour plot of the cross section multiplied by Branching Ratio upper limit in the χ_2^0,χ_1^0 mass plane. This plot is directly applicable to the generic process $e^+e^\perp \to XY \to \gamma YY$ assuming an isotropic decay for $X \to \gamma Y$ and isotropic production angles. In addition the limits are robust to the 5% level if instead the X and Y particles are produced with a $1 + \cos^2\theta$ polar angle distribution. The two

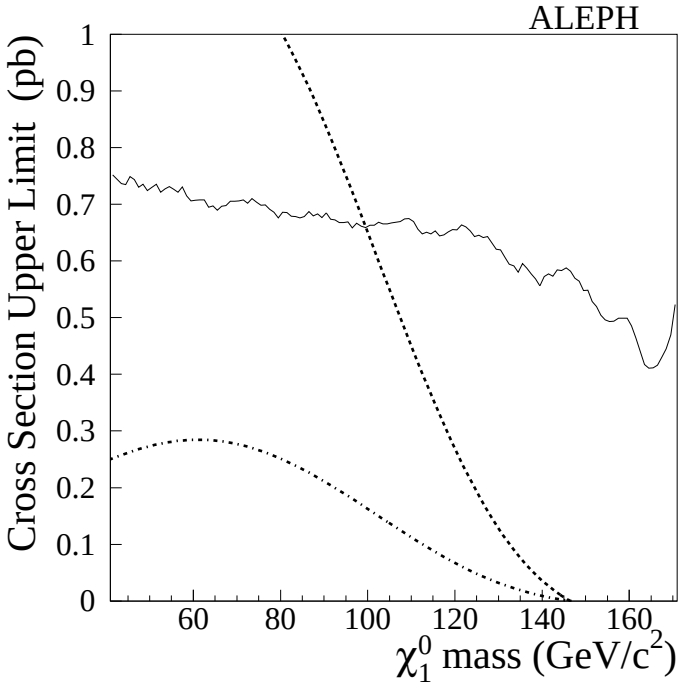

Figure 3.12: *The 95% C.L. upper limit on the production cross-section for* $e^+e^\perp \to \chi_1^0\tilde{G} \to \tilde{G}\tilde{G}\gamma$. *The limit is valid for* $\sqrt{s} = 172$ *GeV assuming* β^8/s *threshold behavior. Overlayed are the predicted cross sections from the LNZ model for* $e^+e^\perp \to \chi_1^0\tilde{G}$ *given a gravitino mass of* $10^{\perp 5}$eV/c^2 *(upper curve) and* $2 \times 10^{\perp 5}$eV/c^2 *(lower curve).*

center-of-mass energies are combined assuming β/s threshold dependence. The systematic errors are exactly the same as in the previous section and have negligible effect on the results.

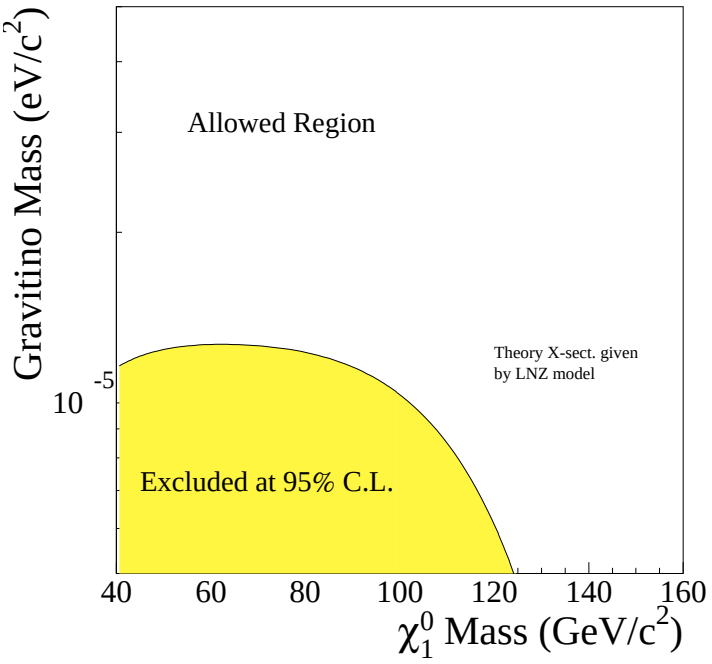

Figure 3.13: *The excluded region in the neutralino mass, gravitino mass plane. The selectron mass and neutralino composition are set according to the LNZ model. Note that the gravitino mass scale is in units of* eV/c^2.

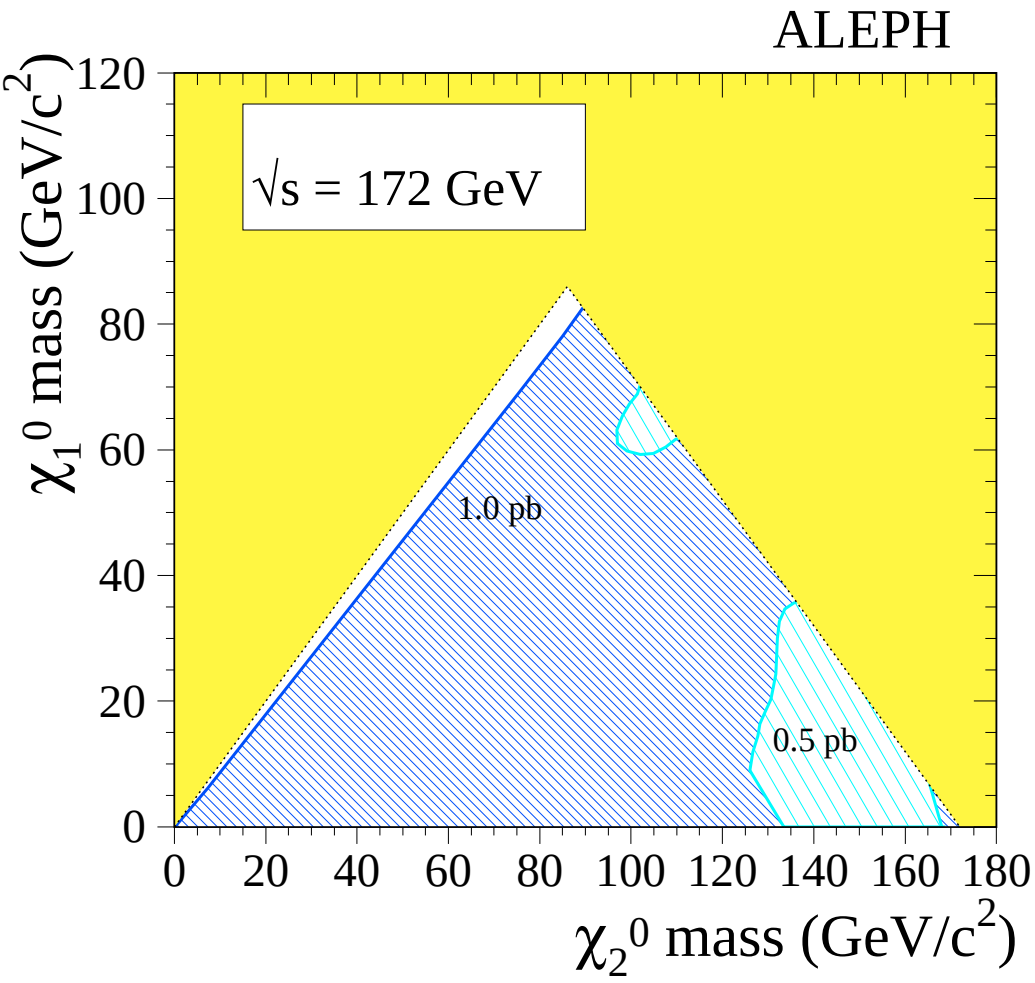

Figure 3.14: *The contour plot of the 95% C.L. upper limit on the production cross section for* $e^+e^\perp \to \chi_2^0\chi_1^0$ *multiplied by the* $BR(\chi_2^0 \to \chi_1^0\gamma)$*. The limit is valid for* $\sqrt{s} = 172\,\mathrm{GeV}$ *assuming* β/s *threshold behavior and isotropic decays.*

Chapter 4

Search for Supersymmetry with Acoplanar Photons

In Chapter 3 the EW events were successfully isolated and the cross section was measured. Then, the Standard Model expectations for the EW process were employed to perform a background subtraction on the EW data sample in order to derive limits on physics beyond the Standard Model.

In this chapter, as we continue the search for physics beyond the Standard Model, the topology of two or more photons and missing transverse energy is studied. Again, the EW and QED events constitute the physics background. The QED events $e^+e^\perp \to \gamma\gamma(\gamma)$ have no missing transverse energy, whereas the signal generally has a large amount of missing transverse energy carried off by the lightest supersymmetric particle (LSP). Supersymmetric events can easily be separated from QED events with a cut on acoplanarity (which is equivalent to a cut on transverse en-

ergy to the beam axis, as explained in Chapter 1). The cross section for the process $e^+e^\perp \to \nu\bar{\nu}\gamma\gamma(\gamma)$ (the EW process with two or more bremsstrahlung photons in the acceptance) is reduced by order α from the cross section discussed in Chapter 3 (the EW process $e^+e^\perp \to \nu\bar{\nu}\gamma(\gamma)$ with one or more bremsstrahlung photons in the acceptance). This background is not large for the given luminosity of 21.7 $pb^{\perp 1}$ and a background-subtraction technique is not utilized. Therefore, the strategy for the search for acoplanar photons is to develop a selection criteria (in addition to the cosmic ray and detector noise cuts of Chapter 3) that eliminates or reduces to a small level the presence of EW and QED events. The data are passed through this selection criteria, the remaining events are counted and this number is used to set an upper limit on the cross section for the Supersymmetric processes that produce acoplanar photons.

Supersymmetry is the reference model for the derived limits, but the cross section limits are much more general and can be used to constrain other models which predict the signature of photons and missing transverse energy (for example, compositeness models that predict an excited neutrino with the decay $\nu^* \to \nu\gamma$). The chapter proceeds as follows: the general selection for acoplanar photons is discussed in Section 1, the search for Supersymmetric models which predict the gravitino to be the LSP are detailed in Section 2 and the search for Supersymmetric models which predict the neutralino to be the LSP is described in Section 3.

4.1 Acoplanar photon preselection

As described in Chapter 1, there are two supersymmetric scenarios which give the signature of acoplanar photons. In gravitino LSP supersymmetric models the process $e^+e^\perp \to \chi_1^0\chi_1^0 \to \tilde{G}\tilde{G}\gamma\gamma$ is a possibility at LEP2. In the neutralino LSP scenario (with the neutralino composition suggested by the CDF event) the process $e^+e^\perp \to \chi_2^0\chi_2^0 \to \chi_1^0\chi_1^0\gamma\gamma$ is possible at LEP2. The signals differ in that the LSP is essentially massless in the first scenario and can have substantial mass in the second scenario. After the common preselection there are two slightly different search criteria for the two scenarios, as described in the sections below.

The preselection is designed to reduce the cosmic ray, detector noise and QED backgrounds to a negligible level. These are the same backgrounds that were studied for the EW signal in Chapter 3 and, hence, the acoplanar preselection contains many of the same selection criteria. The preselection begins by requiring no charged tracks that do not come from a conversion. Due to detector acceptance only photons within $|\cos\theta| < 0.95$ are counted. Since for the acoplanar photon search at least two photons are required, background from cosmic rays and detector noise is less severe, so the impact parameter requirement is not imposed. Dropping the impact parameter cut allows this selection criteria to remain efficient for the scenario where the decay of the NLSP into the LSP and a photon occurs away from the Interaction Point. Events with more than two photons are required to have at least $0.4\sqrt{s}$ of missing energy. As shown in Figure 3.6, this cut reduces significantly three-photon events from the

Acoplanar-photon selection criteria	Cumulative signal eff.(%)	$\nu\bar{\nu}\gamma\gamma(\gamma)$ bkg. σ (pb)	$\gamma\gamma(\gamma)$ bkg. σ (pb)
Acoplanar-photon preselection			
N_γ=2 OR ($N_\gamma \geq 3$ and $E_{missing} > 0.4\sqrt{s}$)	83	0.36	12
Acoplanarity $< 177^\circ$	81	0.35	0.30
Additional energy < 1 GeV	73	0.32	0.008
Total $p_\perp > 0.0375 E_{missing}$	73	0.30	0.002
Cosmic ray and detector noise cuts	73	0.30	0.002
$\tilde{G}$ LSP analysis			
$E_2 \geq 18$ GeV	69	0.043	0.002
χ_1^0 LSP analysis			
$M_{missing} \leq 82$ GeV/c^2 OR	71	0.16	0.002
$M_{missing} \geq 100$ GeV/c^2 OR $E_2 \geq 10$ GeV			
Two photons inside $\lvert\cos\theta\rvert < 0.8$	52	0.063	-

Table 4.1: *The acoplanar-photon selection criteria, and the additional cuts required by the two analyses described in the text. Signal efficiency for the gravitino LSP analysis is given for a 65 GeV/c^2 χ_1^0 at $\sqrt{s} = 161$ GeV. For the χ_1^0 LSP analysis the efficiency numbers are given for a 45 GeV/c^2 χ_2^0 and a 20 GeV/c^2 χ_1^0. Background numbers are given for $\sqrt{s} = 161$ GeV but are similar for 172 GeV.*

QED process. Missing transverse energy is required by imposing an acoplanarity cut at 177° and requiring that the additional total energy be less than 1 GeV. Figure 4.1 shows the acoplanarity distributions for $e^+e^\perp \to \gamma\gamma(\gamma)$ events, $e^+e^\perp \to \chi_1^0\chi_1^0 \to \tilde{G}\tilde{G}\gamma\gamma$ events and $e^+e^\perp \to \chi_2^0\chi_2^0 \to \chi_1^0\chi_1^0\gamma\gamma$ events. When there are three or more photons in the event, the two most energetic photons are used to determine the acoplanarity. The QED background is effectively eliminated after the above selection criteria. The total $p_\perp$ is required to be greater than 3.75% of the missing energy, reducing background from radiating events with final state particles escaping down the beam axis to a negligible level. The selection criteria and cross sections for the surviving background are shown in Table 4.1. After this initial selection the only remaining significant

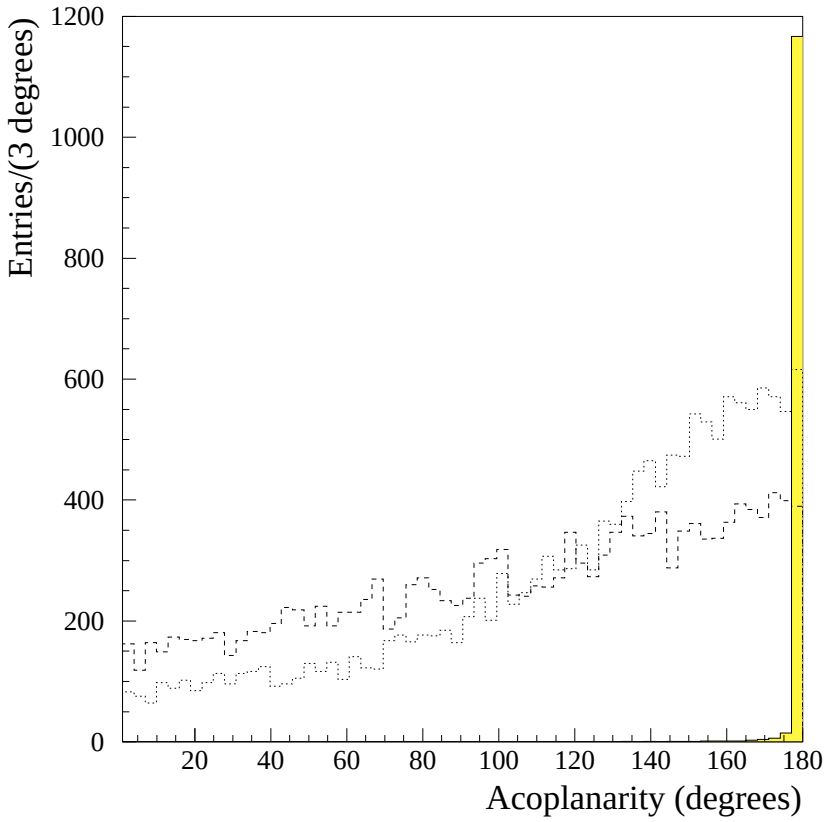

Figure 4.1: *The acoplanarity distribution is plotted for simulated* $e^+e^\perp \to \gamma\gamma(\gamma)$ *events (hatched histogram),* $e^+e^\perp \to \chi_1^0\chi_1^0 \to \tilde{G}\tilde{G}\gamma\gamma$ *events (dashed histogram) and* $e^+e^\perp \to \chi_2^0\chi_2^0 \to \chi_1^0\chi_1^0\gamma\gamma$ *events (dotted histogram) at* $\sqrt{s} = 161\,\mathrm{GeV}$ *after all other acoplanar-photon preselection cuts. They are normalized to the number of events, but the QED events are weighted by .1 (so in the plot each QED event represents 10 events when compared to a supersymmetric event). The* $e^+e^\perp \to \chi_1^0\chi_1^0 \to \tilde{G}\tilde{G}\gamma\gamma$ *events are for a 65 GeV/*c^2 *neutralino and the* $e^+e^\perp \to \chi_2^0\chi_2^0 \to \chi_1^0\chi_1^0\gamma\gamma$ *events are for a* χ_2^0 *mass of 45 GeV/*c^2 *and a* χ_1^0 *mass of 20 GeV/*c^2*. Note that the* $e^+e^\perp \to \chi_2^0\chi_2^0 \to \chi_1^0\chi_1^0\gamma\gamma$ *events are more peaked at high acoplanarity than the* $e^+e^\perp \to \chi_1^0\chi_1^0 \to \tilde{G}\tilde{G}\gamma\gamma$ *events due to the lighter mass of the NLSP. The cut is made on the very last bin at* 177°.

run #	event #	$M_{missing}$ (GeV/c^2)	E_1 (GeV)	E_2 (GeV)	$\cos\theta_1$	$\cos\theta_2$
41604	1172	95.3	50.6	2.9	-0.30	-0.63
41869	2325	133.6	23.4	2.4	0.72	0.87
42453	3636	123.8	27.8	15.3	0.63	0.16

Table 4.2: *The properties of the events selected by the acoplanar preselection. The first two events are from the 161 GeV data and the last event is from the 172 GeV data.*

background is from EW events. Two events are selected at 161 GeV while 2.7 are expected from $e^+e^\perp \to \nu\bar{\nu}\gamma\gamma(\gamma)$ events. At 172 GeV, one event is selected while 2.3 are expected. Table 4.2 lists the three data events and their properties.

4.2 Acoplanar photon search: $\tilde{G}$ LSP scenario

For the gravitino LSP search, an additional cut is placed on the energy of the second most energetic photon (E_2) to reduce substantially the remaining background from the EW process. The energy distribution of the second most energetic photon is peaked near zero for EW events (as shown in Figure 4.2), whereas for signal events both photons have a flat distribution in an interval depending on the neutralino mass and $\sqrt{s}$, as given by equations (1.11 - 1.14). Plugging in 65 GeV/c^2 for the neutralino mass at $\sqrt{s}$ = 161 GeV, the corresponding range of photon energy is 16.5 GeV to 64.0 GeV. Thus, with a cut at 15 GeV, the background can be significantly reduced with no cost in efficiency for a 65 GeV/c^2 neutralino.

The energy cut for the second most energetic photon is determined by an optimization procedure [56] which consists in minimizing $\overline{\sigma}_{95} = \overline{N}_{95}/L$, the average value

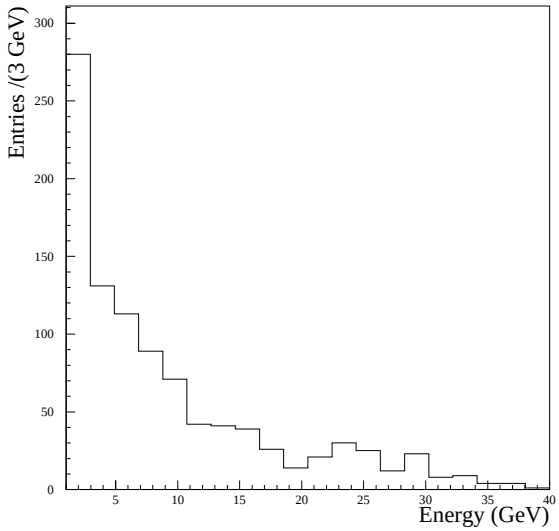

Figure 4.2: *Energy of the second most energetic photon from simulated* $e^+e^\perp \to \nu\bar{\nu}\gamma\gamma(\gamma)$ *events (arbitrarily normalized) passing the acoplanar-photon preselection. For signal events, the energy of each photon has a flat distribution in a range dependent on* $\sqrt{s}$ *and the* χ_1^0 *mass.*

of the 95% C.L. upper limit on the signal production cross section, with L equal to the integrated luminosity and

$$\overline{\mathrm{N}}_{95} = \frac{e^{\perp b(x)}}{\varepsilon(x)}(3.00 + 4.74\frac{b(x)}{1!} + 6.30\frac{b^2(x)}{2!} + 7.75\frac{b^3(x)}{3!} + \cdots) \tag{4.1}$$

as obtained with a large number of random experiments in the absence of any signal contribution. Here, $\varepsilon(x)$ is the signal efficiency and $b(x)$ is the remaining number of expected background events after all cuts, with the energy cut set to x. Large samples of Monte Carlo are used to find both $\varepsilon(x)$ and $b(x)$. Note that $e^{\perp b(x)}\frac{b^n(x)}{n!}$ are the Poisson probabilities for seeing $n = 0, 1, 2, \ldots$ events when $b(x)$ are expected for the integrated luminosity L. The factors $3.00, 4.74, 6.30, \ldots$ are the corresponding

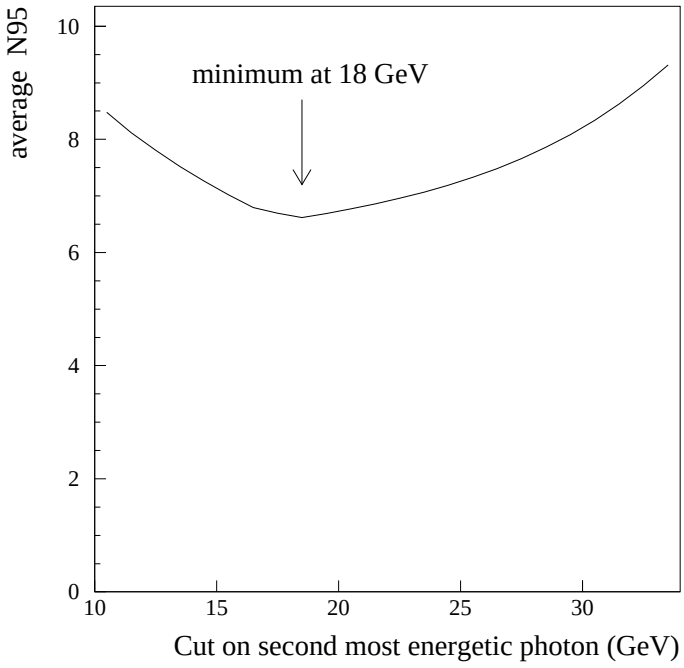

Figure 4.3: *The average expectation for the upper limit on the number of events excluded at 95% confidence level ($\overline{N}_{95}$) vs. the cut on the second most energetic photon. The χ_1^0 mass is 67 GeV/c^2.*

95% C.L. upper limits without background subtraction. An optimal cut is found by minimizing $\overline{N}_{95}$ with respect to the cut value.

Using the theoretical cross-section for neutralino production (with neutralino composition set to pure B-ino), the efficiency, the expected background and the luminosity are used to estimate the expected exclusion at 95% C.L. on the neutralino mass. Then, for this mass neutralino, the energy cut is varied and the minimum of $\overline{N}_{95}$ is found in order to choose an optimized energy cut (as shown in Figure 4.3). For 11.1 $pb^{\perp 1}$ of data at 161 GeV and 10.6 $pb^{\perp 1}$ of data at 172 GeV, the optimal cut is 18 GeV for a

neutralino mass of 67 GeV/c^2. With the requirement that the second most energetic photon must have E $\geq$ 18 GeV, the background is reduced to 0.045 pb (essentially all from the $e^+e^\perp \to \nu\bar{\nu}\gamma\gamma(\gamma)$ process), while the efficiency remains high at 69% for a neutralino of 65 GeV/c^2 mass produced at $\sqrt{s}$ = 161 GeV. For neutralino masses greater than 70 GeV/c^2 the photon energy is constrained (for $\sqrt{s} \leq 172$ GeV) by the kinematics to be above 18 GeV and the efficiency loss due to the E_2 cut is negligible (a fraction of a percent is lost due to energy mismeasurement).

The efficiency was estimated using the SUSYGEN Monte Carlo program and setting the parameters so that the χ_1^0 is pure B-ino and then adding a new decay (with 100% Branching Ratio) $\chi_1^0 \to \tilde{G}\gamma$.

After the $\tilde{G}$ LSP selection criteria no events are found where 0.92 events are expected from background sources. Figure 4.4 shows the upper limit on the cross section compared to two theoretical predictions. The neutralino is taken to be pure B-ino and the right-selectron mass is set to 1.5 times the neutralino mass. The integrated luminosity taken at $\sqrt{s}$ = 161 GeV is scaled by the ratio of cross sections to those at 172 GeV. The upper limit on the cross section is not strongly dependent on the above choice. Scaling the luminosity at 161 GeV by the threshold dependence β^3/s (with $\beta = \sqrt{1 - \frac{4M_\chi^2}{s}}$) changes the cross section limit by less than 5%. The mass

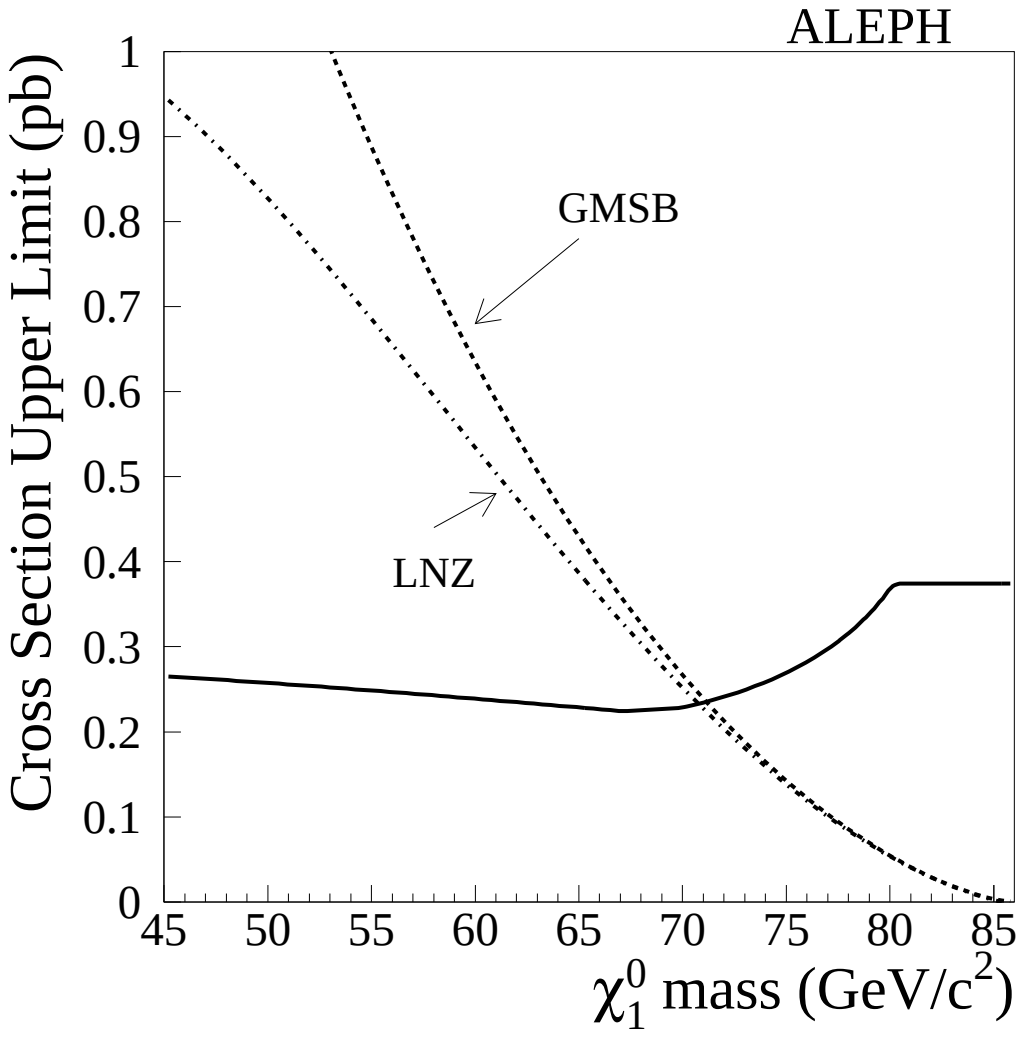

Figure 4.4: *The 95% C.L. upper limit on the production cross section for* $e^+e^\perp \to \chi_1^0\chi_1^0 \to \tilde{G}\tilde{G}\gamma\gamma$ *when* χ_1^0 *has a lifetime less than 3 ns. The limit is valid for* $\sqrt{s} = 172$ *GeV. The data from 161 GeV are included by scaling the luminosity by the ratio of the cross section at that energy to the cross section at 172 GeV. Two different theories are compared to the experimental limit. The right selectron mass is taken to be 1.5 that of the neutralino mass for the GMSB Theory.*

limits obtained are:

$$M_{\chi_1^0} \geq 71.0\,\mathrm{GeV}/c^2 \text{ at } 95\%\,\mathrm{C.L.}$$

for a pure B-ino neutralino with $\tau_{\chi_1^0} \leq 3$ ns [1] (applicable to Gauge-Mediated Supersymmetric Breaking models, the selectron mass is taken to be 1.5 times the neutralino mass) and

$$M_{\chi_1^0} \geq 70.7\,\mathrm{GeV}/c^2 \text{ at } 95\%\,\mathrm{C.L.}$$

(for the LNZ No-Scale Super Gravity model).

The systematic error for this analysis is less than 6%, dominated by photon reconstruction. The effect of this uncertainty on the cross section upper limits is less than 1% following the method of Ref. [55]. The effect on the mass limit is completely negligible.

As discussed in Chapter 1, the neutralino in GMSB models can have a non-negligible lifetime. The neutralino lifetime is given in equation 1.15. The efficiency for a neutralino with lifetime was estimated by taking 100% reconstruction efficiency within a distance l from the IP and 0% reconstruction efficiency outside l. The average reconstruction distance l was found empirically by generating several Monte Carlo samples with various neutralino lifetimes and performing a χ^2 fit to the formula below, leaving the distance to reconstruct as a free parameter (as shown in Figure 4.5). The efficiency loss due to lifetime ϵ_τ is given by

[1] There is almost no efficiency loss for lifetimes below 3 ns. For longer lifetimes the efficiency is reduced, as will be discussed in the next paragraph.

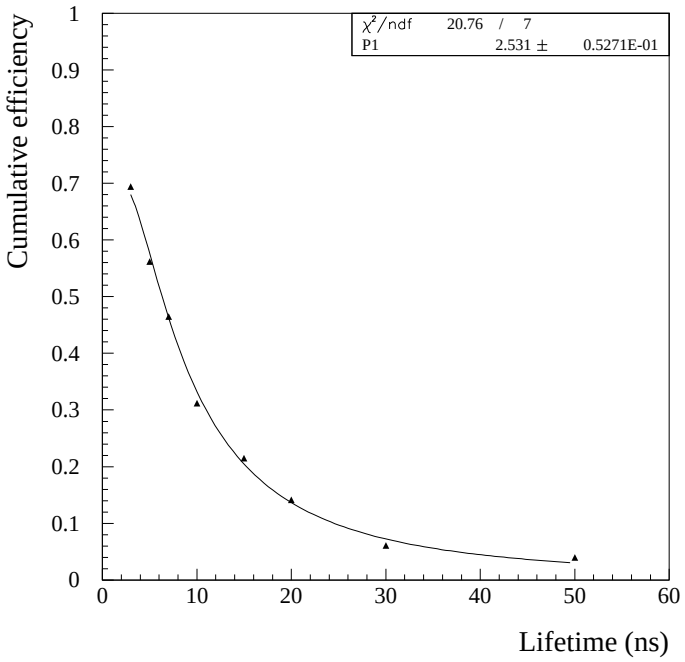

Figure 4.5: *The efficiency of all cuts for a 65 GeV/c^2 χ_1^0 with lifetime. The fitted parameter P1 refers to l, the average reconstruction distance.*

$$\epsilon_\tau \simeq [1 - e^{\perp(\frac{M*l}{P*c\tau})}]^2 \tag{4.2}$$

where M and P are the mass and momentum of the neutralino. The average reconstruction distance was found to be 2.5 m. This value for l agrees with what one might expect because in order to reconstruct the photon there must be energy in the second stack of the ECAL, which is on average about 2.5 m from the IP. The efficiency was checked at other mass values and found to be in good agreement with the above formula with $l = 2.5$ m. Figure 4.6 shows the 95% C.L. exclusion limit in the $\sqrt{F}$, $M_{\chi_1^0}$ plane.

At LEP2 the production of neutralinos would proceed via the t-channel exchange

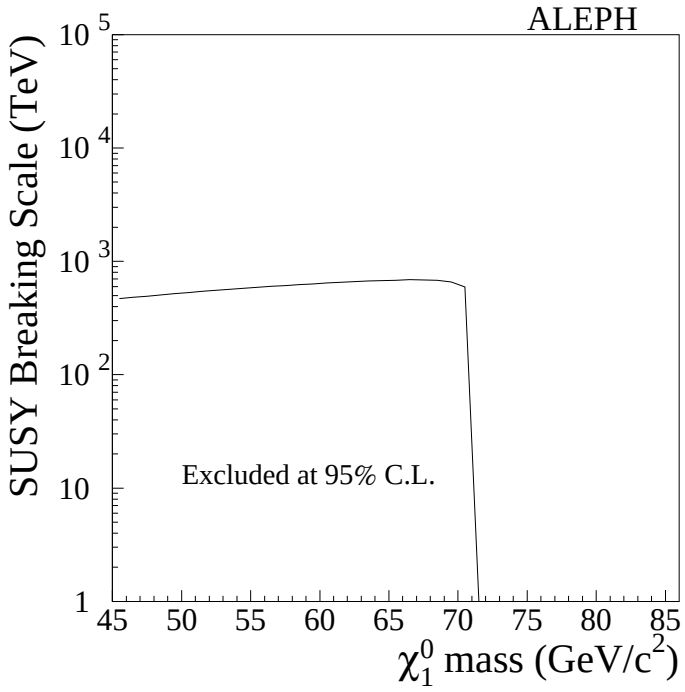

Figure 4.6: *The excluded region in the neutralino mass, $\sqrt{F}$ plane, where the selectron mass is set to 1.5 times the neutralino mass. There is a cosmological upper bound on $\sqrt{F}$ at 10^5 TeV from nuclear synthesis [57].*

of a selectron. The cross section for $e^+e^\perp \to \chi_1^0\chi_1^0$ depends strongly on the right-selectron mass and weakly on the left-selectron mass (as shown in equation 1.10). In order to obtain the dependence of the neutralino mass limit on the selectron mass, right-selectron masses are scanned from 1 GeV to 250 GeV (in steps of 100 MeV) and neutralino masses from 1 GeV to 86 GeV (in steps of 100 MeV). The number of events expected from theory for 11.1 $pb^{\perp 1}$ at $\sqrt{s}$ = 161 GeV and 10.6 $pb^{\perp 1}$ at $\sqrt{s}$ = 172 GeV are derived and compared to the experimental limit at each $M_{\tilde{e}_R}$, $M_{\chi_1^0}$ mass point to obtain the neutralino mass limit as a function of right-selectron mass.

The neutralino mass limits were also checked for various left-selectron masses. The result is found to be robust at the ± 1 GeV level for left-selectron masses ranging from $M_{\tilde{e}_L} = M_{\tilde{e}_R}$ to $M_{\tilde{e}_L} \gg M_{\tilde{e}_R}$.

The experimentally excluded region in the neutralino, selectron mass plane is shown in Figure 4.7. Overlayed is the 'CDF region', the area in the neutralino, selectron mass plane where the properties of the CDF $ee\gamma\gamma + E^T_{MISS}$ event are compatible with the process $q\bar{q} \to \tilde{e}\tilde{e} \to ee\chi_1^0\chi_1^0 \to ee\tilde{G}\tilde{G}\gamma\gamma$. Half of the CDF region is excluded at 95% C.L. by this analysis.

4.3 Acoplanar Photon Search: χ_1^0 LSP Scenario

For the neutralino LSP scenario, a straight energy cut is not optimal since the χ_1^0 can be massive and the photons from the $\chi_2^0 \to \chi_1^0\gamma$ decay can have low energy. Here the fact that the $\nu\bar{\nu}\gamma\gamma(\gamma)$ background peaks at high $|\cos\theta|$ and missing mass at the Z

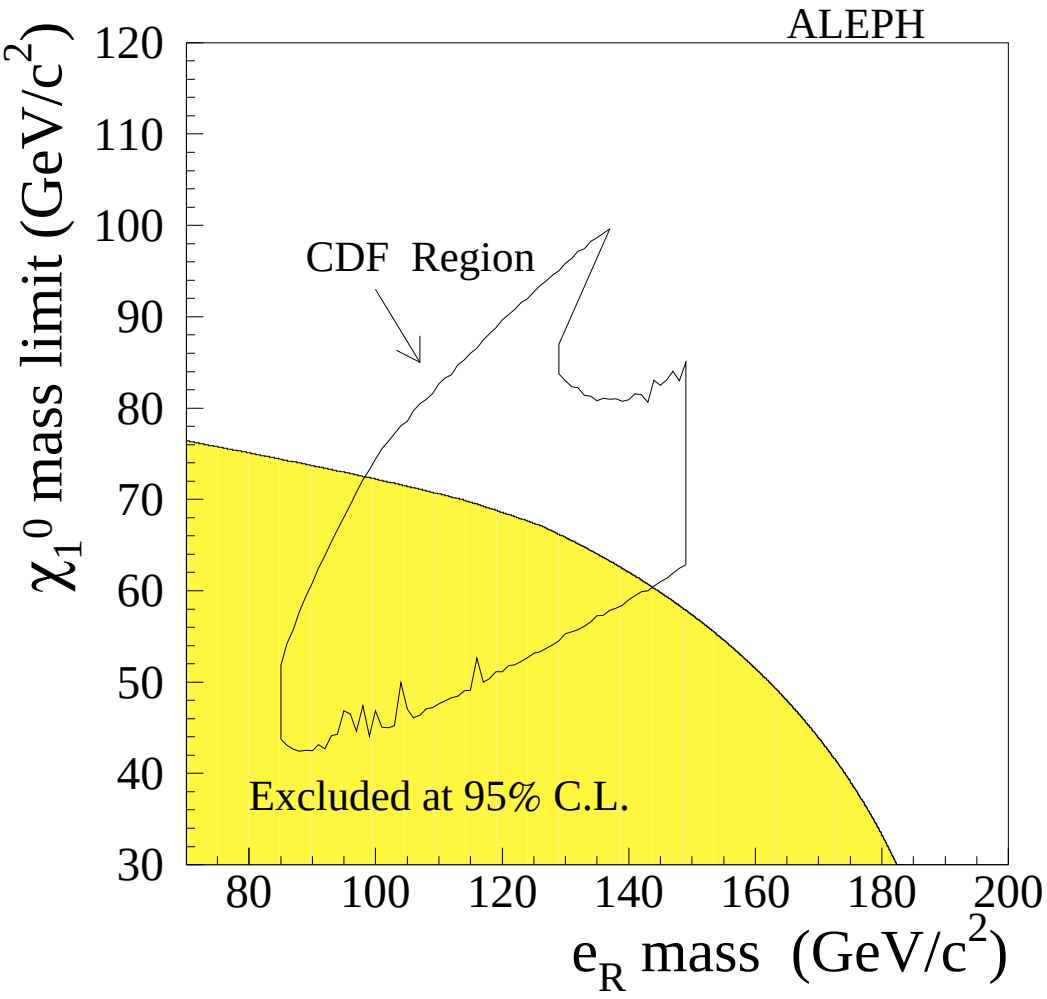

Figure 4.7: *The excluded region in the neutralino, selectron mass plane at 95% C.L. for a pure B-ino neutralino (shaded area). Overlayed is the CDF region [23] determined from the properties of the CDF event assuming the reaction* $q\bar{q} \to \tilde{e}\tilde{e} \to ee\chi_1^0\chi_1^0 \to ee\tilde{G}\tilde{G}\gamma\gamma$*; the region has been cutoff (vertical line) where the prediction rate becomes uninterestingly small.*

mass is utilized. Events that have missing mass between 82 GeV/c^2 and 100 GeV/c^2, and the energy of the second most energetic photon less than 10 GeV are cut, as shown in Figure 4.8. The $\cos\theta$ cut is optimized using the $\overline{\mathrm{N}}_{95}$ procedure as described in the previous section. In this analysis, the efficiency does not depend strongly on the mass of χ_2^0 and is approximately constant for $\Delta M_{\chi_2^0 \perp \chi_1^0} \geq 20$ GeV/c^2. The $\cos\theta$ cut is optimized once for the $\Delta M_{\chi_2^0 \perp \chi_1^0} \geq 20$ GeV/c^2 area of the $\mathrm{M}_{\chi_2^0}$,$\mathrm{M}_{\chi_1^0}$ mass plane (this requirement on the χ_2^0, χ_1^0 mass difference is suggested by the kinematics of the CDF event given the neutralino LSP interpretation). The predicted $\cos\theta$ distribution for the signal and the Monte Carlo $\cos\theta$ distribution for the $\nu\bar{\nu}\gamma\gamma(\gamma)$ background are used for the optimization. The $\overline{\mathrm{N}}_{95}$ optimization for 11.1 pb$^{\perp 1}$ at 161 GeV and 10.6 pb$^{\perp 1}$ at 172 GeV is $|\cos\theta| < 0.8$ (as shown in Figure 4.9). The final selection criteria and cross sections for the remaining background are given in Table 4.1.

The efficiency is estimated using a large sample of the SUSYGEN Monte Carlo at both 161 and 172 GeV. In total, 42 files were generated (five of which were fully reconstructed) at $\sqrt{s} = 161$ GeV covering the χ_2^0, χ_1^0 mass plane. The efficiency is obtained from the generation level files (corrected for reconstruction and conversions by comparing with the fully reconstructed files). Five files at selected χ_2^0 and χ_1^0 mass points were generated at $\sqrt{s} = 172$ GeV. The efficiencies matched (within error) those at 161 GeV. The efficiency for various χ_2^0 and χ_1^0 masses is shown in Table 4.3. At low χ_2^0 masses the efficiency drops due to the acoplanarity cut.

In the χ_1^0 LSP analysis one event is found in the data where 1.3 events are expected from background. The candidate event has a missing mass of 123.8 GeV and photon

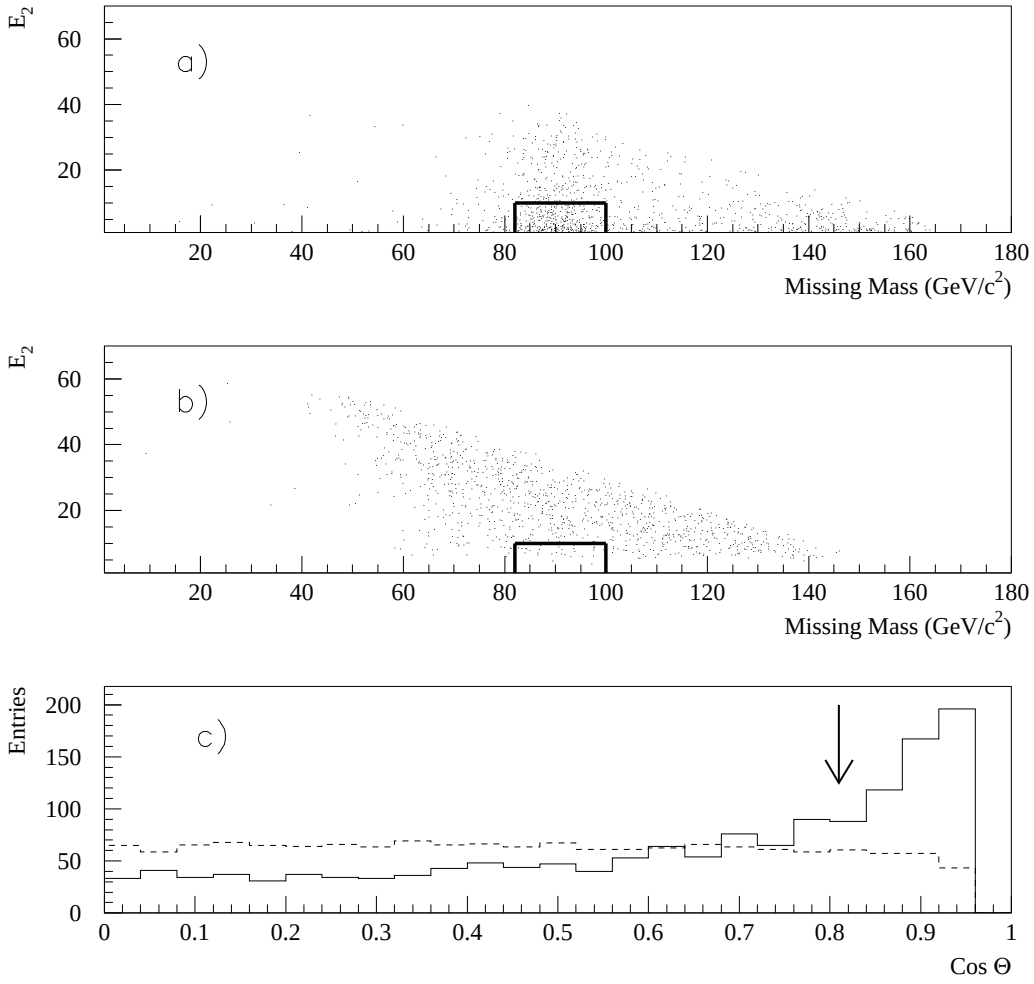

Figure 4.8: *a) The scatter plot of the energy of the second most energetic photon vs. the missing mass distribution for simulated* $e^+e^\perp \to \nu\bar{\nu}\gamma\gamma(\gamma)$ *events. The events inside the box are cut. b) The same plot as a) but for signal* $e^+e^\perp \to \chi_2^0\chi_2^0 \to \chi_1^0\chi_1^0\gamma\gamma$ *Monte Carlo events. c) The inclusive* $|\cos\theta|$ *plot after the missing mass and* E_2 *cuts. The solid histogram is* $e^+e^\perp \to \nu\bar{\nu}\gamma(\gamma)$ *events and the dashed histogram is* $e^+e^\perp \to \chi_2^0\chi_2^0 \to \chi_1^0\chi_1^0\gamma\gamma$ *events. In all plots the histograms are normalized to the number of events passing the acoplanar-photon preselection. The* $e^+e^\perp \to \chi_2^0\chi_2^0 \to \chi_1^0\chi_1^0\gamma\gamma$ *events are for a* χ_2^0 *mass of 45 GeV/*c^2 *and a* χ_1^0 *mass of 20 GeV/*c^2 *at* $\sqrt{s} = 161$ *GeV.*

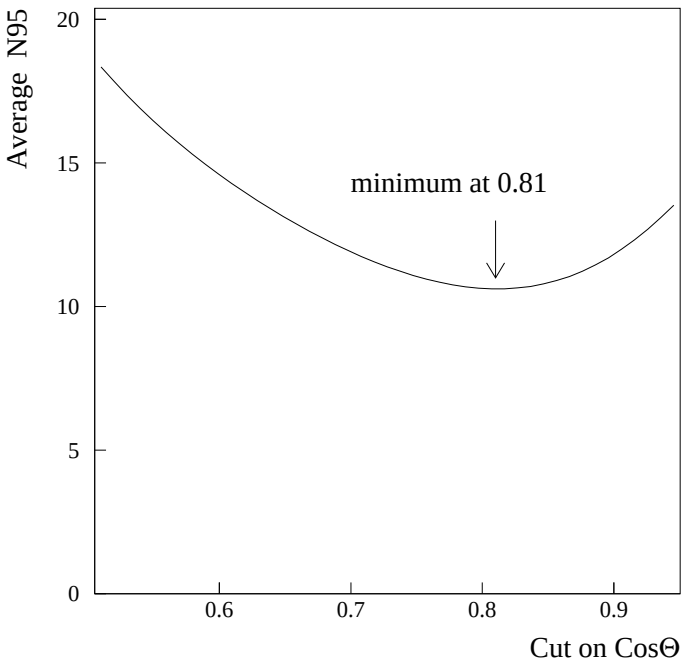

Figure 4.9: *The average expectation for the upper limit on the number of events excluded at 95% confidence level ($\overline{N}_{95}$) vs. the cut on the cosine of the polar angle.*

energies of 28 and 15 GeV; the event is shown in Figure 4.10. The upper limits on the cross section multiplied by Branching Ratio in the χ_1^0, χ_2^0 mass plane are shown in Figure 4.11. The systematic uncertainties for this analysis are the same as for the gravitino LSP scenario and the effect on the upper limit is again less than 1%.

The χ_1^0 LSP interpretation of the CDF event (along with the non-observation of other supersymmetric signatures at Fermilab) suggests a high Branching Ratio for $\chi_2^0 \rightarrow \chi_1^0\gamma$. In order for both the mass difference and Branching Ratio to be large, the χ_2^0 composition must be dominantly photino and the χ_1^0 must be dominantly higgsino, or vice versa. In the scenario that χ_2^0 is pure photino and χ_1^0 is pure higgsino, the

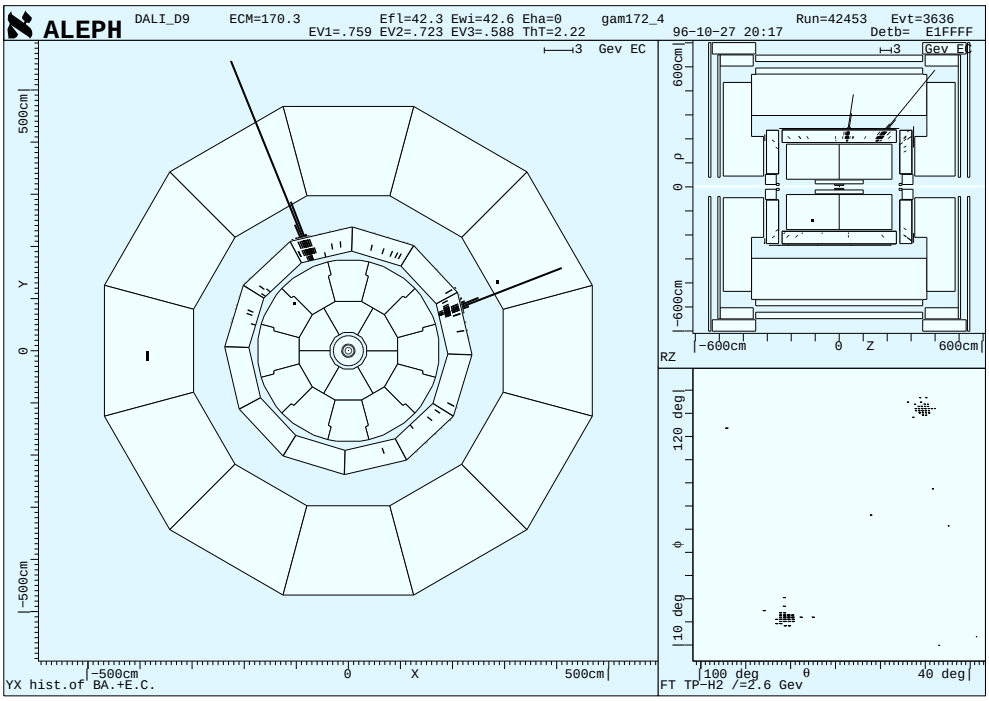

Figure 4.10: *The candidate event, x-y view, for the neutralino LSP analysis. Both photons are contained in the barrel of the ECAL as shown in the r-z view (upper right). The photon clusters are shown in the $\theta - \phi$ view (lower right).*

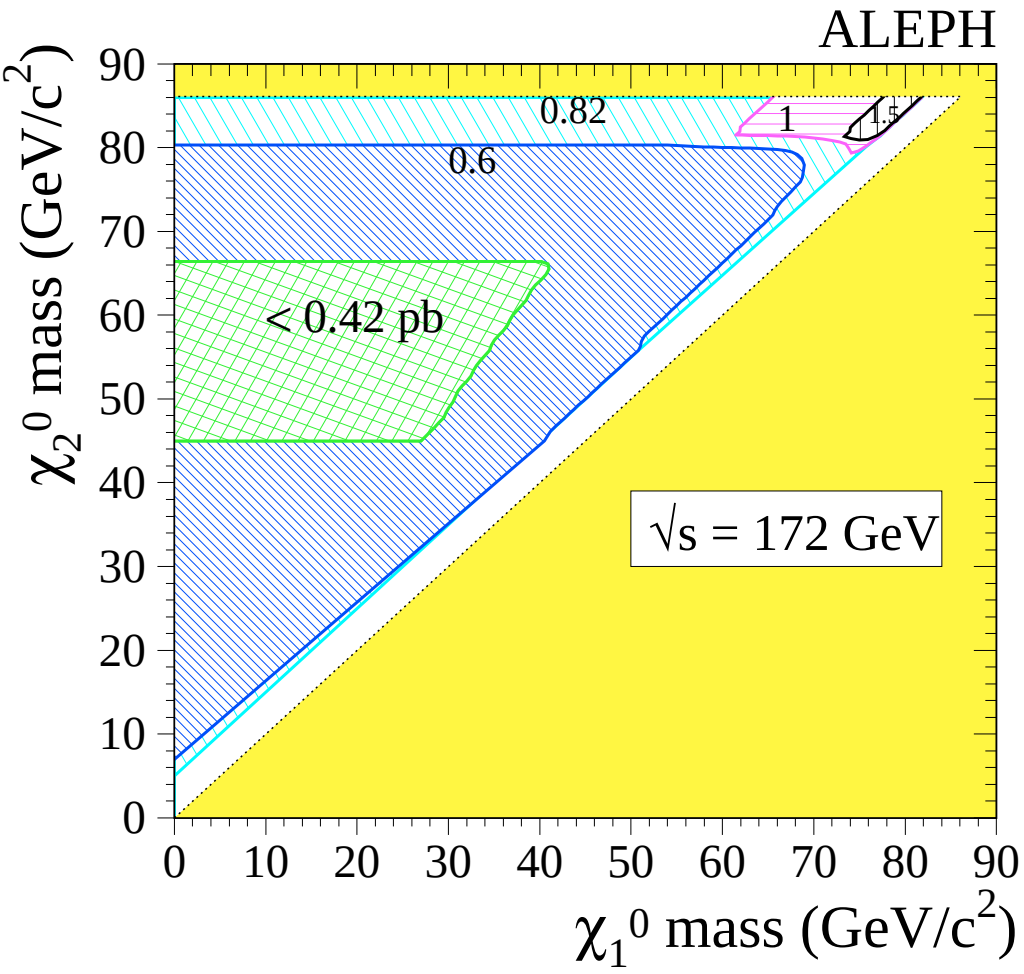

Figure 4.11: *The 95% C.L. upper limit on the production cross section for* $e^+e^\perp \to \chi_2^0\chi_2^0 \to \chi_1^0\chi_1^0\gamma\gamma$ *multiplied by the* $BR(\chi_2^0 \to \chi_1^0\gamma)$ *squared. The limit is valid for* $\sqrt{s} = 172$ *GeV assuming* β/s *threshold behavior and isotropic decays.*

$M_{\chi_2^0}$ (GeV/c^2)	$M_{\chi_2^0 \perp \chi_1^0}$ (GeV/c^2)			
	5	10	20	40
5	33			
10	41	45		
40	40	51	51	52
80	34	47	55	57

Table 4.3: *The efficiency(%) for the* $e^+e^\perp \to \chi_2^0\chi_2^0 \to \chi_1^0\chi_1^0\gamma\gamma$ *process at* $\sqrt{s} = 161\,\mathrm{GeV}$. *The efficiencies at 172 GeV are equal (within errors) to those at 161 GeV.*

Branching Ratio for $\chi_2^0 \to \chi_1^0\gamma$ is 100% [2]. Assuming this scenario, the lower mass limit of χ_2^0 as a function of the selectron mass is calculated and compared to the region compatible with the CDF event. In Figure 4.12 two scenarios $M_{\tilde{e}_L} = M_{\tilde{e}_R}$ and $M_{\tilde{e}_L} \gg M_{\tilde{e}_R}$ are shown. These results exclude a significant portion of the region compatible with the kinematics of the CDF event [3] given by the neutralino LSP interpretation.

[2]This happens when the Supersymmetry parameters $\tan\beta$, $|\ \mu\ |$, M_1 and M_2 are set as follows $\tan\beta = 1$, $|\ \mu\ | < 0$, and $M_1 = M_2$.

[3]This is obviously an optimistic scenario, since the cross section limit goes up proportional to one over the square of the Branching Ratio.

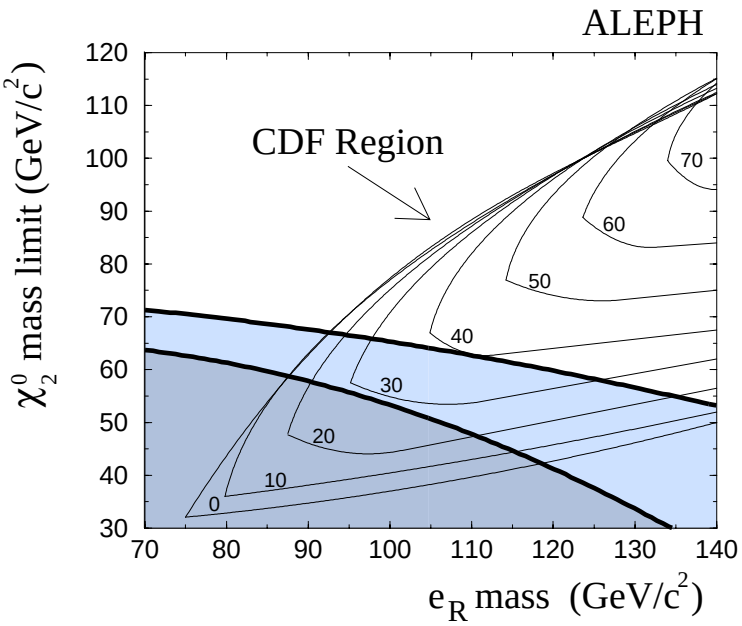

Figure 4.12: *The CDF region [12] labeled by the mass of* χ_1^0 *in* GeV/c^2. *This is the area determined from the properties of the CDF event assuming the reaction* $q\bar{q} \to \tilde{e}\tilde{e} \to ee\chi_2^0\chi_2^0 \to ee\chi_1^0\chi_1^0\gamma\gamma$. *The hatched area is the experimental exclusion region at 95% C.L. for a pure photino* χ_2^0 *and a pure higgsino* χ_1^0 *(corresponding to the choice of parameters* $M_{\tilde{e}_L} = M_{\tilde{e}_R}$, $tan\beta = 1.0$, $M_1 = M_2$ *and* $\mid \mu \mid < 0$*). The lower line refers to the excluded region for* $M_{\tilde{e}_L} >> M_{\tilde{e}_R}$. *The excluded region is based on the assumption that the* $BR(\chi_2^0 \to \chi_1^0\gamma) = 1$. *The mass limit is independent of the* χ_1^0 *mass as long as* $\Delta M_{\chi_2 \perp \chi_1} \geq 20$ GeV/c^2.

Chapter 5

The Photonic QED process

$e^+e^- \to \gamma\gamma(\gamma)$

Electron-positron annihilation into two photons is the only pure Quantum Electrodynamics (QED) process at LEP2. That is, the electroweak corrections to this process are negligible. Thus, the $e^+e^\perp \to \gamma\gamma(\gamma)$ cross section can be calculated solely from the QED diagrams. The signal topology is dramatic, generally consisting of two photons in the final state, each with the beam energy. The only known physics background that mimics the signal topology are Bhabha events ($e^+e^\perp \to e^+e^\perp$). These events are separated from the signal events by requiring no charged tracks in the tracking chamber and allowing at most one converted photon per event. Cosmic ray events which can sometimes fake the final state topology are reduced to a negligible level by imposing the cosmic ray and detector noise cuts developed in Chapter 3. The QED chapter proceeds as follows. In Section 1 the analysis to isolate the QED

events is presented. In Section 2 the measurement of the $e^+e^\perp \to \gamma\gamma(\gamma)$ cross section is detailed. Finally, in Section 3, using the QED event sample, the total number of events and polar angle distribution are studied and compositeness limits are derived.

5.1 QED Event Selection

The signal topology of two back-to-back photons with the beam energy is very easy to isolate from other processes. An event display of such an event is shown in Figure 5.1. Events with no charged tracks and at least two reconstructed photons (as defined in Section 2.12) are selected. The cosmic ray and detector noise cuts are applied. The only events to survive this initial selection are assumed to be EW events with two or more radiated photons and the QED events [1]. The QED events are separated from the EW events by considering the properties of the two processes. The energy distribution of EW events has the property that the second most energetic photon peaks at low values (as shown in Figure 4.2) whereas in QED events both photons are very energetic (as shown in Figure 5.2). Two photons are, therefore, required to carry significant energy $E_\gamma > 0.2\sqrt{s}$. In the EW events there is always missing energy carried off by the neutrinos and normally missing transverse momentum as well. Events with exactly two photons in the acceptance are required to have acoplanarity $> 170°$. The cut is made on acoplanarity as opposed to acolinearity in order to accept events where a third photon escapes undetected down the beam

[1] The background from Bhabha events is measured to be less than 1%

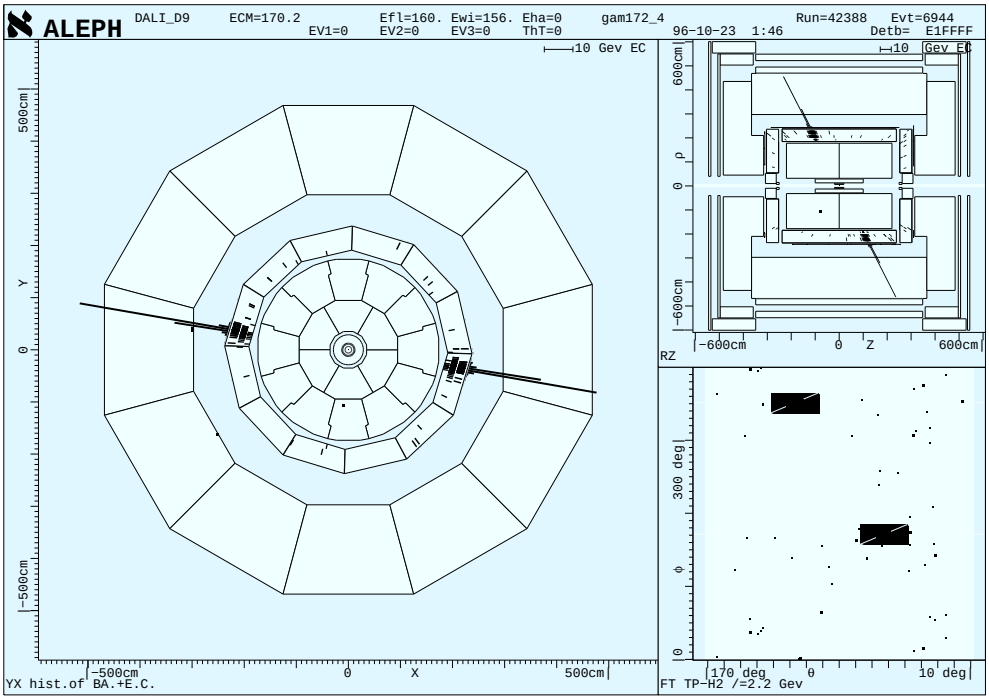

Figure 5.1: *A typical QED two-photon event in the x-y view (left). The photons are back-to-back and each one has energy equal to the beam energy. On the right are the r-z (upper right) and θ-ϕ (lower right) views of the detector.*

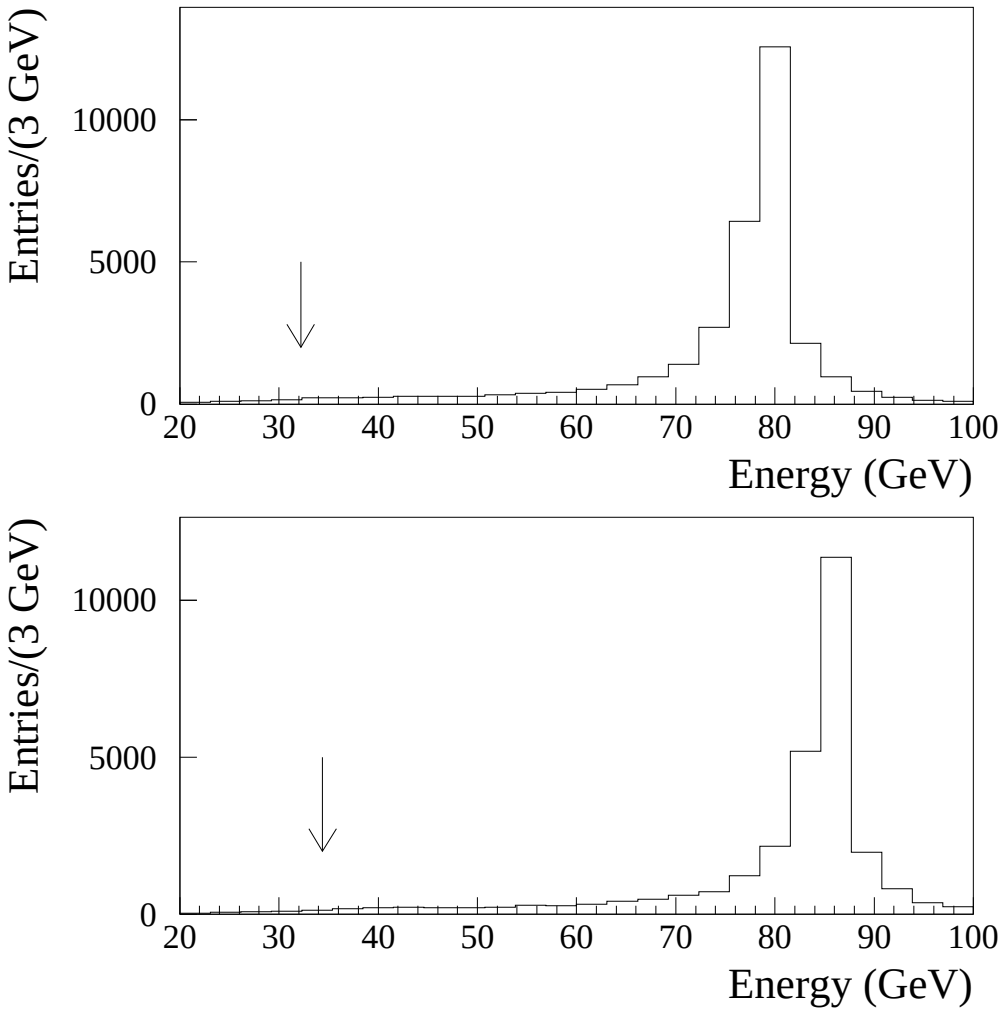

Figure 5.2: *The energy distribution for simulated* $e^+e^- \to \gamma\gamma(\gamma)$ *events. Some events have energy greater than the beam energy due to detector resolution. The cuts on the energy are indicated by an arrow for both 161 GeV (upper plot) and 172 GeV (lower plot).*

axis (the preferred direction for bremsstrahlung photons). Events with three or more photons are required to have less than $0.4\sqrt{s}$ of missing energy. After this selection criteria the total contamination from the EW process is negligible, as verified by studying the KORALZ Monte Carlo. The selection criteria can be summarized as follows:

Acceptance:

- All photons are required to have $\mid \cos\theta \mid < 0.95$ and E > 1 GeV

Selection cuts:

- There must be no charged tracks in the event that do not come from a conversion
- At least two photons, each with energy greater than $0.2\sqrt{s}$, are required
- For two photon events the acoplanarity is required to be greater than 170°
- Events with three or more photons are required to have a missing energy less than $0.4\sqrt{s}$
- The event must pass the cosmic ray selection criteria

5.2 Measurement of the $e^+e^- \to \gamma\gamma(\gamma)$ cross section

The efficiency inside the acceptance is 82.3% at 161 GeV and 83.0% at 172 GeV, estimated using the QED Monte Carlo. After all cuts, 117 two-photon events, 7 three-photon events and no events with four or more photons were found at $\sqrt{s} = 161$ GeV

while 127 two-photon events and 7 three-photon events are expected from the Monte Carlo. At $\sqrt{s} = 172$ GeV, 104 two-photon events , no three-photon events and one four-photon event were found, while 108 two-photon events and 6 three-photon events are expected. The only background expected is from $e^+e^\perp \to e^+e^\perp$ events where a hard photon is radiated and the $e^+e^\perp$ in the final state is reconstructed as a photon conversion. The background estimation from this process is about one event for each center-of-mass energy. Inside the acceptance the corresponding cross-sections are

$$\sigma(\mathrm{e^+e^- \to \gamma\gamma(\gamma)}) = 13.5 \pm 1.2 \pm 0.6\,\mathrm{pb} \quad \text{at} \quad \sqrt{\mathrm{s}} = 161 \quad \mathrm{GeV}$$

$$\sigma(\mathrm{e^+e^- \to \gamma\gamma(\gamma)}) = 11.8 \pm 1.2 \pm 0.5\,\mathrm{pb} \quad \text{at} \quad \sqrt{\mathrm{s}} = 172 \quad \mathrm{GeV}$$

These results are consistent with the Standard Model predictions from the Monte Carlo, of 14.7 ± 0.1 pb at 161 GeV and 13.1 ± 0.2 pb at 172 GeV.

The sources of systematic uncertainty, shown in Table 5.1, are the same as for the EW process except for the background from radiating events down the beam axis which is negligible. Background from Bhabha events is estimated from the Monte Carlo and found to contribute less than 1% to the event sample. The total systematic error is obtained by adding in quadrature the individual contributions.

5.3 $\cos\theta^*$ Definition

Due to initial state radiation the polar angle as seen in the detector is often quite different from the angle in the center-of-mass frame of the observed photons.

Photon Selection	4%
Converted photon selection	0.6%
Background	<1%
Integrated Luminosity	0.7%
Monte Carlo theoretical	< 1%
Monte Carlo statistical	0.6%
Total (in quadrature)	4%

Table 5.1: *Systematic errors on the cross-section for the QED process.*

Figure 5.3 shows a QED event with an unobserved third photon down the beam axis. In order to extract compositeness limits and compare data to Monte Carlo it is useful to plot the variation of observed and predicted number of events as a function of the polar angle in the center-of-mass system $\cos\theta^*$. We define $\cos\theta^*$ as:

$$\cos\theta^* = \frac{\cos\frac{1}{2}(\theta_1 + \pi - \theta_2)}{\cos\frac{1}{2}(\theta_1 - \pi + \theta_2)} \tag{5.1}$$

where θ_1 and θ_2 are the polar angles of the two photons. The missing energy is obtained from the angular information where the assumption has been made that all the missing momentum points along the beam axis. The polar angles of the photons are then boosted in the beam axis direction to obtain $\cos\theta^*$, the polar angle in the center-of-mass frame. For two-photon events where the third photon is emitted along the beam axis (most of them) this definition is exact. This definition is not used for events with three or more photons in the acceptance. The use of $\cos\theta^*$ reduces the difference in the $\cos\theta$ distribution between the Born level calculation and the full calculation including radiative corrections. As we will see in a following section this is especially desirable for compositeness models.

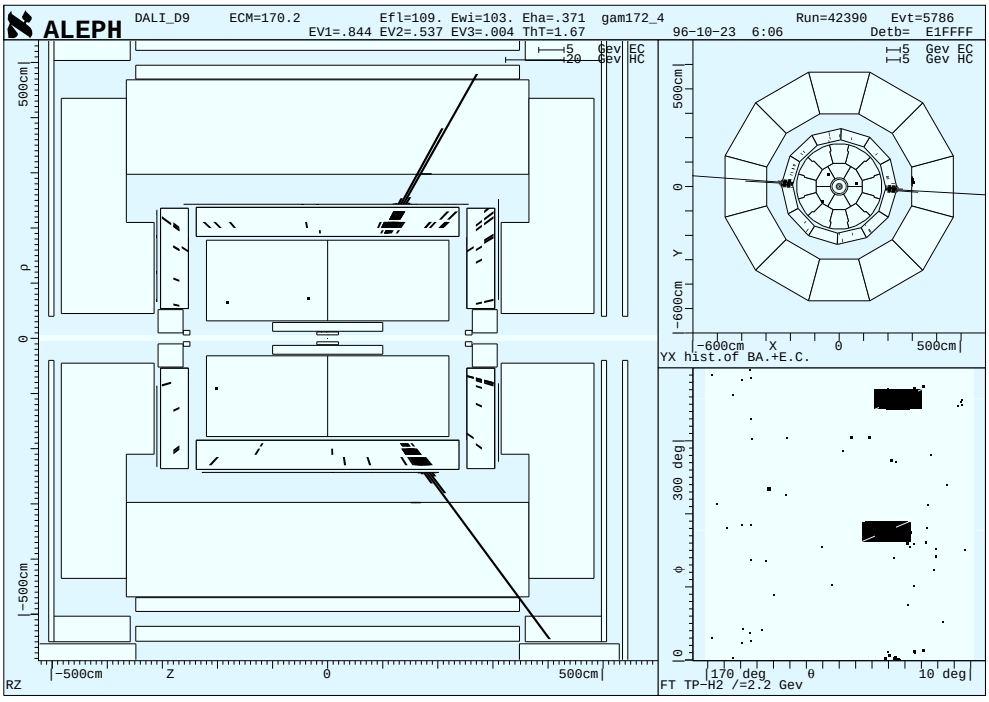

Figure 5.3: *A QED event in the r-z view where an unobserved third photon goes down the beam axis. The photons are back-to-back in acoplanarity because all the missing energy is in the z direction (i.e. no missing transverse energy), as shown in the x-y view (upper right). The r-z view clearly shows the missing energy and the distortion of the* $\cos\theta$*. The* θ*-*ϕ *view is shown in the lower right box.*

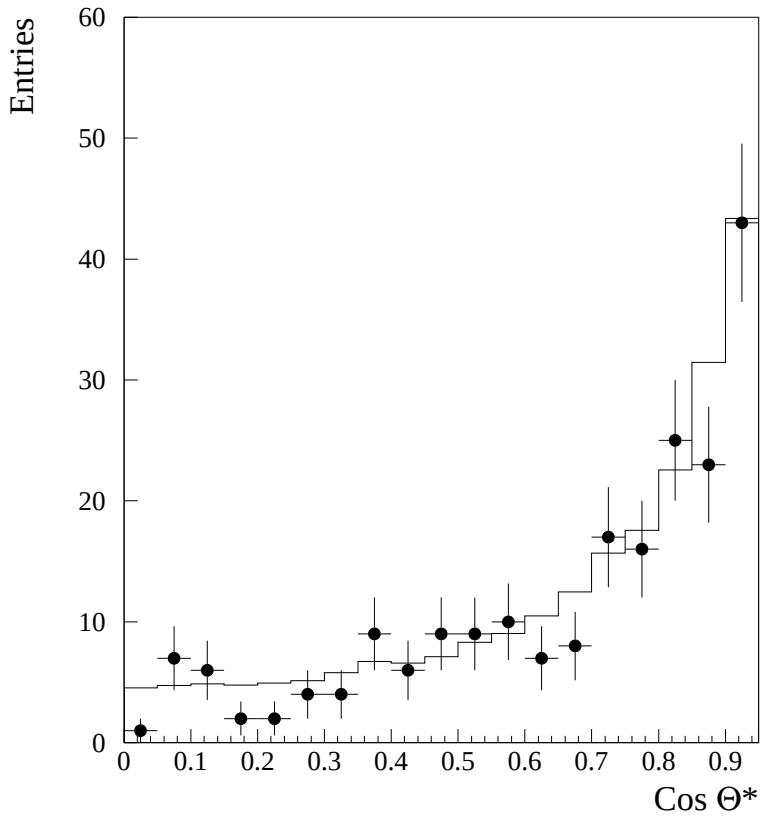

Figure 5.4: *Cosine theta distribution in the center-of-mass reference frame for the QED process (two photon events only). The Monte Carlo is absolutely normalized to the data.*

The $\cos\theta^*$ distribution is in good agreement between the data and QED expectations ($\chi^2/NDF = 15.3/19$) as shown in Figure 5.4. There is no evidence for new physics, thus we are left with the task of setting limits. In this case, a lower limit on a compositeness energy scale and a lower limit on the mass of an excited electron will be found.

5.4 Limits on the Composite Structure of the Electron

Two additional requirements are imposed designed to simplify the procedure of setting limits and raise the average effective center-of-mass energy. Only two-photon events are included in the sample and the effective center-of-mass energy $\sqrt{s'}$ is required to be greater than $0.6\sqrt{s}$. The $\sqrt{s'}$ is calculated relying solely on the measured angles of the two photons. The assumption is made that any missing energy points directly down the beam axis. The $\sqrt{s'}$ is calculated to be

$$\sqrt{s'} = \sqrt{s} - \frac{\sqrt{s}\,|\sin\theta_1 + \sin\theta_2|}{\sin\theta_1 + \sin\theta_2 + |\sin\theta_1 + \sin\theta_2|}. \tag{5.2}$$

The distribution for $\sqrt{s'}$ of the data and QED Monte Carlo is shown in Figure 5.5. The efficiency is reduced to 75% with these two additional cuts. After the requirements of $\sqrt{s'} > 0.6\sqrt{s}$, the average $\sqrt{s'}$ is 157.8 GeV for the $\sqrt{s} = 161$ GeV data and 166.3 GeV for the 172 GeV data. The efficiency for all cuts vs. $\cos\theta^*$ is plotted in Figure 5.6. The efficiency drops slightly at high $\cos\theta^*$ because there are slightly larger cracks in the ECAL endcap modules and more matter in the detector at low angles causing more conversions. Efficiency for conversion reconstruction is only about 60%, averaged over all polar angles inside $|\cos\theta| < 0.95$.

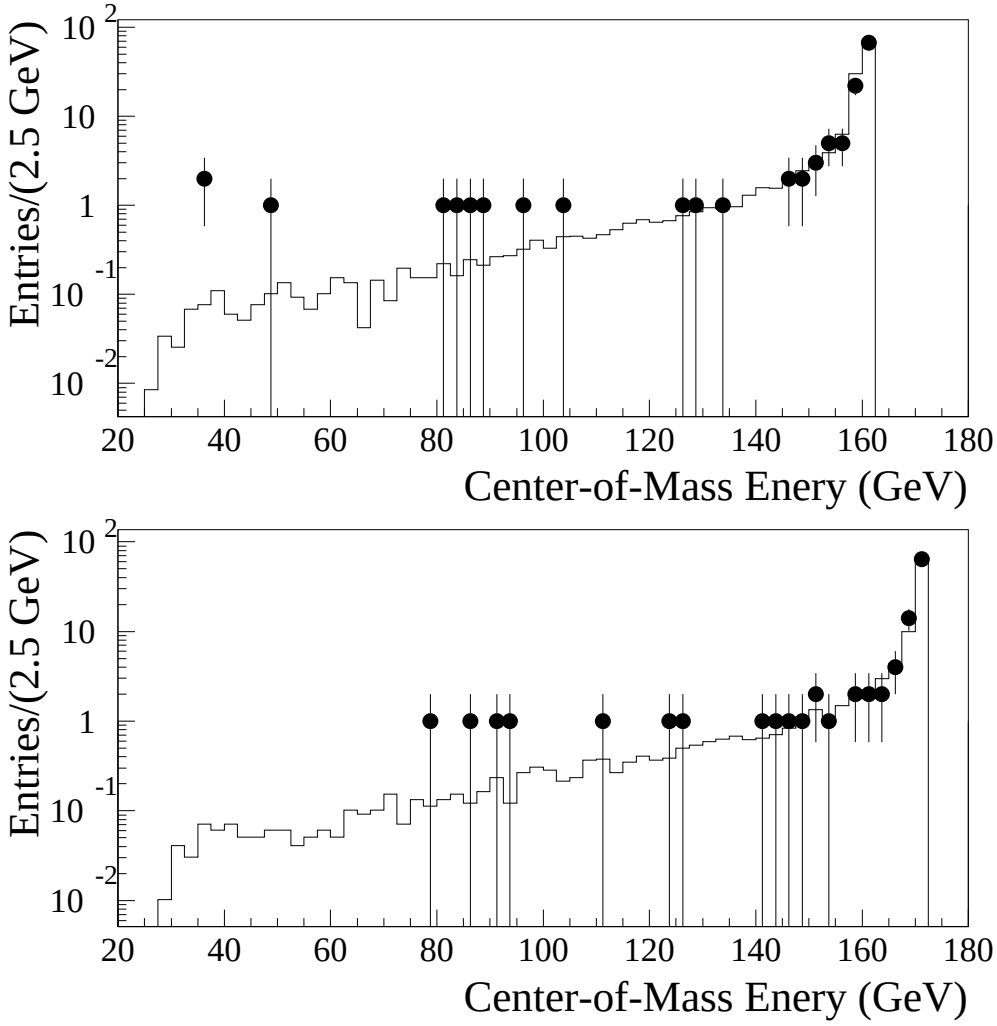

Figure 5.5: *The true center-of-mass energy $\sqrt{s'}$ as calculated from the angles of the photons for both 161 GeV (upper plot) and 172 GeV (lower plot).*

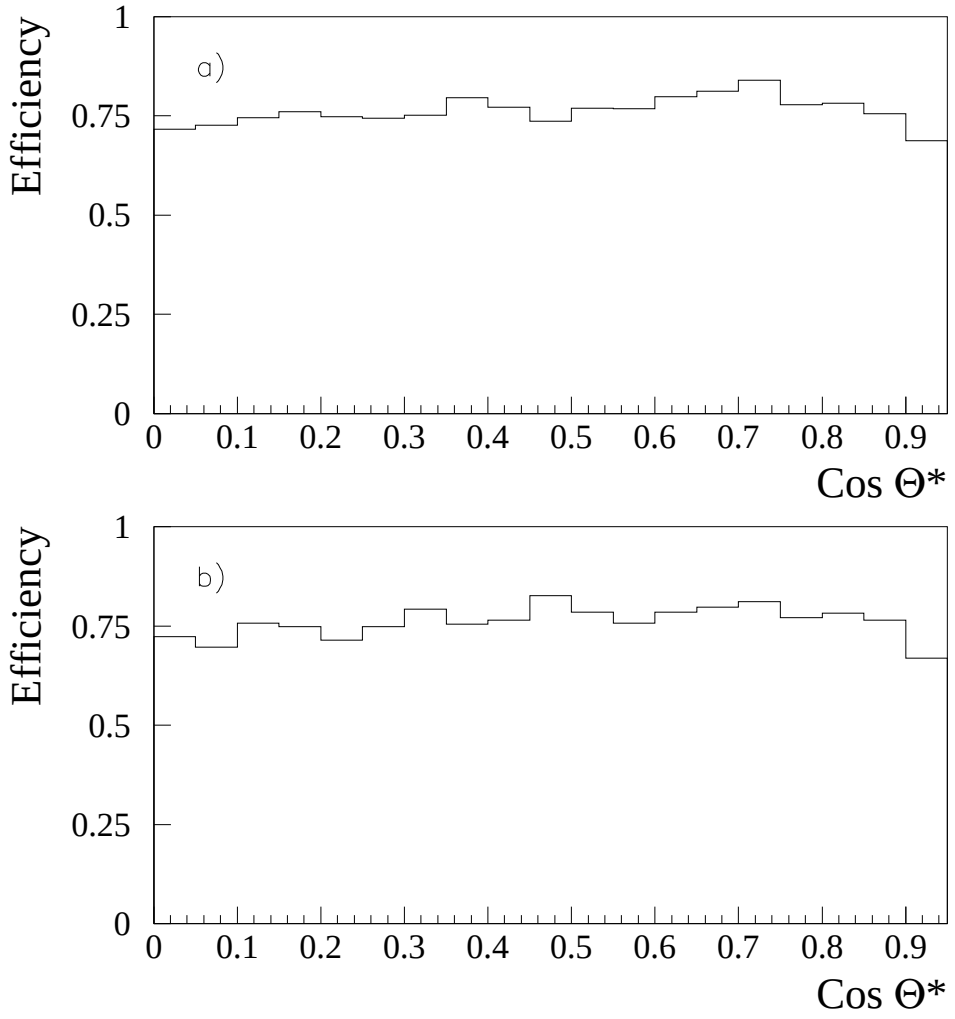

Figure 5.6: *The efficiency as a function of* $\cos\theta^*$ *after all cuts have been applied. The upper plot is for* $\sqrt{s} = 161$ *GeV and the lower plot is for* $\sqrt{s} = 172$ *GeV.*

5.4.1 Radiative corrections

Compositeness theories are non-renormalizable theories. The cross sections for these theories can only be calculated at the Born level. The differential composite cross section at the Born level can be decomposed into the sum of the QED cross section and a QED-breakdown part. The QED-breakdown part is a function of the compositeness energy scale Λ, the polar angle θ and the center-of-mass energy $\sqrt{s}$. The differential composite cross section at the Born level can be written as

$$\left(\frac{d\sigma}{d\Omega}\right)^{Born} = \left(\frac{d\sigma}{d\Omega}\right)^{Born}_{QED} (1 + f(\Lambda_{\pm}, s, \theta)) \,, \tag{5.3}$$

where

$$f(\Lambda_{\pm}, s, \theta) = \pm\frac{s^2}{2\Lambda_{\pm}^4}(1 - \cos^2\theta) + \frac{s^4}{16\Lambda_{\pm}^8}(1 - \cos^2\theta)^2 .$$

A perfect description of the data would include radiative corrections out to all orders in α. The QED Monte Carlo is calculated out to order α^3 which is found to be sufficient to describe the data given our statistics. The question arises how should one account for radiative corrections in the compositeness cross-section calculation. Traditionally, experiments have used the ratio of the order α^3 Monte Carlo QED cross section to the order α^2 Monte Carlo QED cross section to correct the compositeness contribution. The QED differential cross section including compositeness is then rewritten as

$$\left(\frac{d\sigma}{d\Omega}\right)^{\vartheta(\alpha^3)} = \left(\frac{d\sigma}{d\Omega}\right)^{\vartheta(\alpha^3)}_{QED} (1 + f(\Lambda_{\pm}, s, \theta)) \,. \tag{5.4}$$

The scale of the QED radiative corrections defined as

$$\text{Correction factor} = \frac{\left(\frac{d\sigma}{d\Omega}\right)_{QED}^{\vartheta(\alpha^3)}}{\left(\frac{d\sigma}{d\Omega}\right)_{QED}^{Born}} \tag{5.5}$$

is shown in Figure 5.7.

However, this assumes that the order α^3 radiative corrections to the compositeness contribution are exactly the same as for normal QED. It is not obvious that this assumption will give the correct answer. Another method (and more conservative in terms of setting limits) is to compare the data to compositeness theory including radiative corrections only in the QED part. Hence the differential cross section is written as

$$\left(\frac{d\sigma}{d\Omega}\right)^{\vartheta(\alpha^3)} = \left(\frac{d\sigma}{d\Omega}\right)_{QED}^{\vartheta(\alpha^3)} + \left(\frac{d\sigma}{d\Omega}\right)_{QED}^{Born} \left(f(\Lambda_{\pm}, s, \theta)\right). \tag{5.6}$$

In this paper the limits are derived for both scenarios: adjusting the compositeness contribution by the QED radiative corrections and not including radiative corrections in the compositeness contribution.

5.4.2 Setting Limits on Compositeness

The search for compositeness is not a search for new particles but rather a search for a new interaction. That is, the cross section for $e^+e^\perp \to \gamma\gamma(\gamma)$ would be modified due to the particles (called preons) that make up the electron. If these particles exist, the manner in which the electron interacts would be modified. There would be additional Feynman diagram(s) that contribute to the process and the predicted number of events and photon polar angle distribution from $e^+e^\perp \to \gamma\gamma(\gamma)$ would

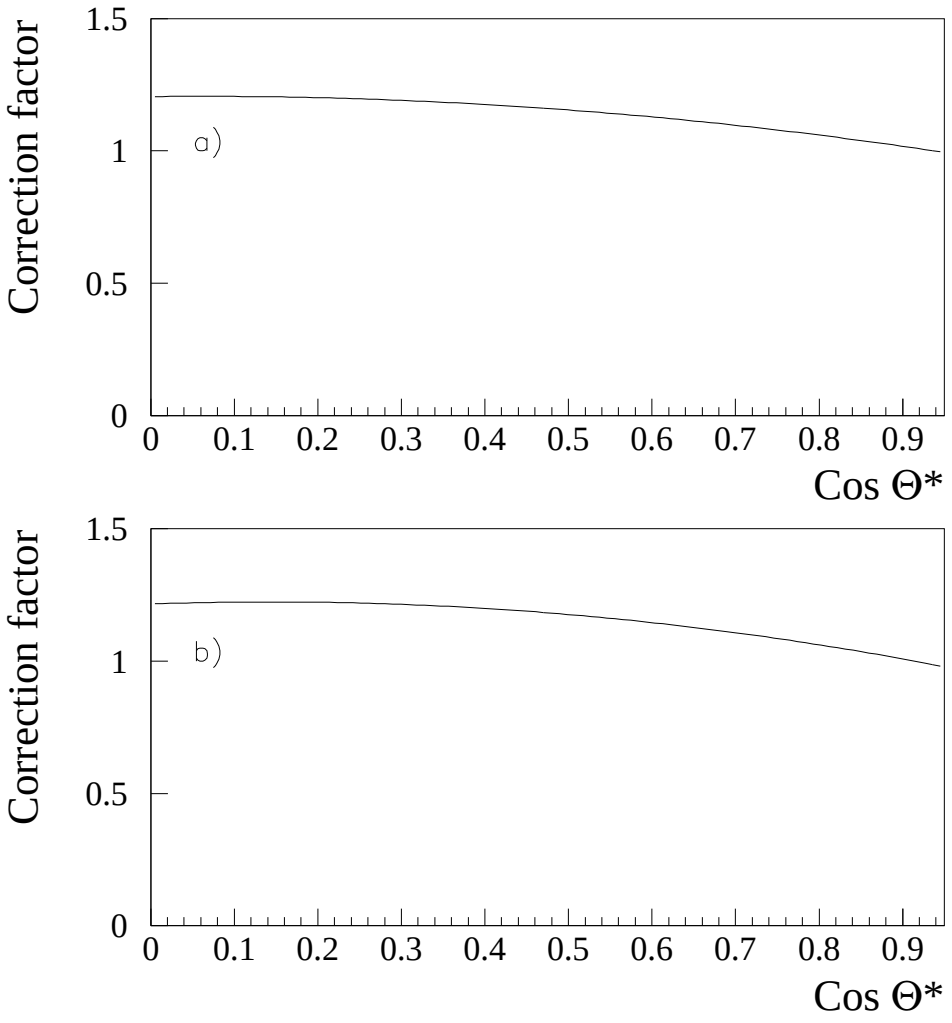

Figure 5.7: *The QED radiative correction factor as a function of* $\cos\theta^*$ *for both 161 GeV (upper plot) and 172 GeV (lower plot).*

change. Normally the interference term between the compositeness diagram and the QED diagrams dominates. The search for compositeness consists of searching for an excess (or deficit) of events as well as a different $\cos\theta^*$ distribution from the pure QED reaction. Similar to the procedure described in Section 3.3 the likelihood method is used on the $\cos\theta^*$ distribution to set limits on compositeness for two scenarios. In one the interference term is positive (which gives rise to an excess of events) and in the other the interference term is negative (deficit of events).

The likelihood function is given by

$$\mathrm{L}(S|\vec{x}) = \prod_{i=1}^{\mathrm{N_{bins}}} \frac{\nu_i^{x_i}}{x_i!} e^{-\nu_i}$$

where x_i is the number of data events in the i^{th} bin of the $\cos\theta^*$ distribution and ν_i is the number predicted in the i^{th} bin. The predicted number of events is the QED Monte Carlo prediction plus (minus) the number of events expected from compositeness for a given cut-off energy Λ_+ ($\Lambda_\perp$). For convenience the cut-off energy is varied in steps of $(200\,\mathrm{GeV}/\Lambda)^4$ and the likelihood function of the data $\cos\theta^*$ distribution and the predicted distribution for the given Λ is calculated at each step. Figure 5.8 shows the likelihood vs. $(200\,\mathrm{GeV}/\Lambda)^4$ curve. The 95% C.L. limit on Λ_+ ($\Lambda_\perp$) is obtained by integrating the likelihood curve over the physically allowed region.

The procedure is done twice each for Λ_+ and $\Lambda_\perp$, including and not including QED radiative corrections in the calculation of the compositeness contribution to the predicted number of events. The results are reported in Table 5.2.

In addition two minor effects which have been traditionally ignored by experiments

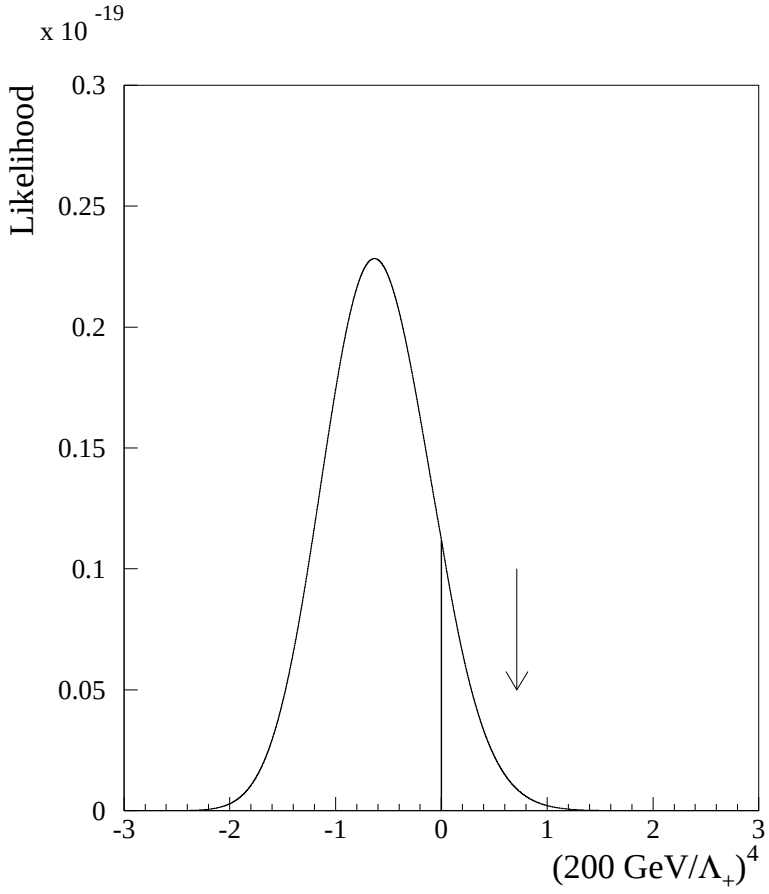

Figure 5.8: *The likelihood function vs.* $(200/\Lambda_+)^4$ *where the 95% C.L. point for* Λ_+ *is indicated by the arrow. The likelihood curve for* $\Lambda_\perp$ *is almost exactly the mirror image.*

in the past are included in the derivation of the limits. The first one is the inclusion of the order $1/\Lambda^8$ term in the compositeness calculation. This term contributes at the 2% level and is always positive irrespective of whether the interference term is positive (Λ_+) or negative ($\Lambda_\perp$). Thus, slightly asymmetric limits are expected.

The second effect concerns the true sensitivity of the experiment. The beam energy might be exactly 80.5 GeV but the center-of-mass energy is never exactly 161

Parameter (GeV)	Λ_+	$\Lambda_\perp$	M_{e^*}
Limit with radiative corrections	217.5	182.9	208.4
Limit without radiative corrections	210.3	175.0	200.6

Table 5.2: *Compositeness limits are given with radiative corrections (equation 5.4) and without radiative corrections (equation 5.6).*

GeV. Due to ISR the energy is always less than 161 GeV and sometimes significantly less (as shown in Figure 5.5). Using the beam energy to calculate the compositeness contribution (as has been traditionally done) overestimates the predicted change in the number of events and the derived limits come out higher than they really are by approximately 2%. The average $\sqrt{s'}$ after the selection criteria (including the cut $\sqrt{s'} > 0.6\ \sqrt{s}$) is 157.8 for the 161 GeV data and 166.3 for the 172 GeV data. The final cut-off energy limits are $\Lambda_+ > 217.5$ GeV and $\Lambda_\perp > 182.9$ GeV at 95% C.L.

The $\cos\theta^*$ distribution compared to the QED prediction is shown in Figure 5.9. Also indicated, as dotted lines, are the 95% C.L. lower limits on Λ_+ and $\Lambda_\perp$. The asymmetric limits are explained by the one sigma deficit of events in the data. The deficit is even more apparent at large angles accentuating the effect.

5.4.3 Excited Electron Exchange

In the previous section, the search for electron compositeness was based on searching indirectly for the constituent particles of the electron. If the electron is a composite object it is expected to have excited states in the same manner as mesons and baryons. Electron compositeness may be discovered through the existence of excited

electron states that couple to the electron and photon.

In a separate analysis [58] ALEPH has searched for the direct production of electron excited states. However these searches can never find (and therefore never exclude) an e^* with a mass greater than the available center-of-mass energy of the experiment. By considering the $e^+e^\perp \to \gamma\gamma(\gamma)$ process, the e^* mass reach can be extended well beyond the center-of-mass energy threshold available to the experiment. The existence of an electron excited state would modify the $\cos\theta^*$ distribution and the total number of events from the $e^+e^\perp \to \gamma\gamma(\gamma)$ reaction. The additional contribution to the photon pair production due to e^* exchange depends on the e^* mass and the $ee^*\gamma$ coupling. The lower limit on the e^* mass and upper limit on the $ee^*\gamma$ coupling are derived using the same procedure as for the cut-off energy limits. The ν_i in the likelihood function is now equal to the QED prediction plus the additional contribution from the existence of an e^* state with mass M_{e^*} and $ee^*\gamma$ magnetic coupling term $\frac{e\lambda}{2M_{e^*}}\overline{\Psi}_{e^*}\sigma_{\mu\nu}\Psi_e F^{\mu\nu} + h.c.$. Calculating the e^* exchange contribution at each M_{e^*} point ranging from 80 GeV/c^2 to 250 GeV/c^2 and for a λ ranging from 0 to 1.4, the 95% C.L. limits are found in the M_{e^*}, λ plane by integrating the likelihood functions. Figure 5.10 shows the results. For the case $\lambda = 1$ the mass of the e^* is excluded below 208.4 GeV/c^2 at 95% C.L.

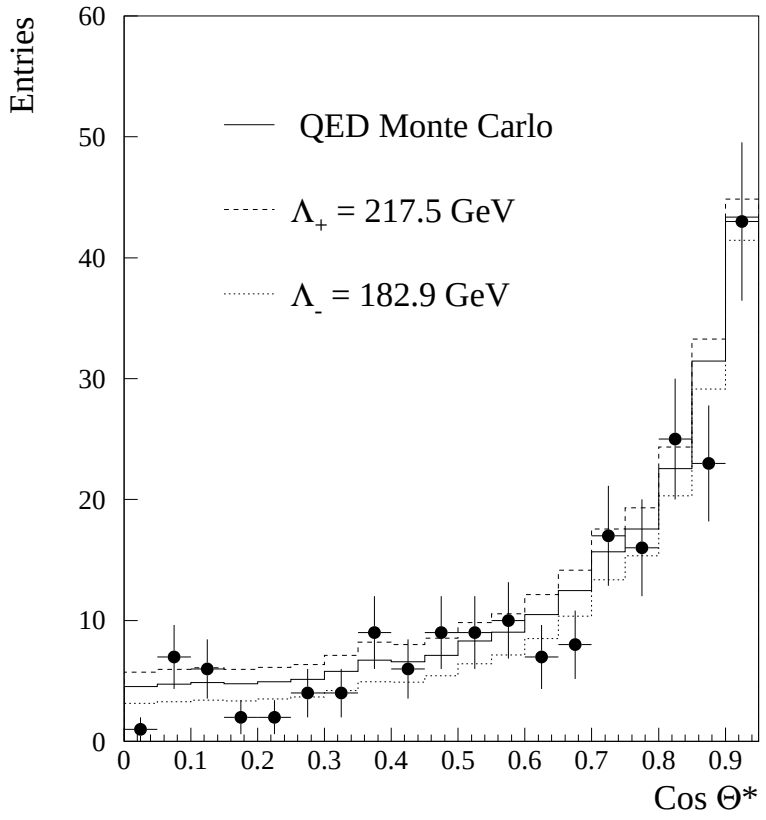

Figure 5.9: *The* $\cos\theta^*$ *distribution in the center-of-mass energy reference frame for the* $e^+e^\perp \to \gamma\gamma(\gamma)$ *process. The QED Monte Carlo is absolutely normalized to the data. Also shown are the compositeness model expectations with the QED cut-off energies* Λ_+ *and* $\Lambda_\perp$ *set to their 95% C.L. lower limits (dotted histograms).*

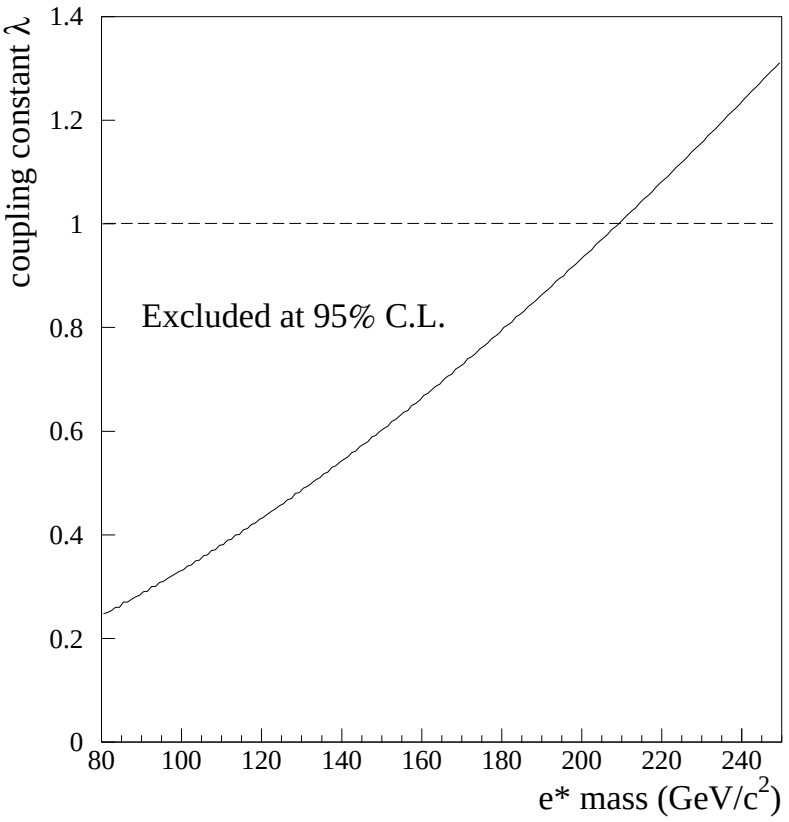

Figure 5.10: *The exclusion line in the e^* mass, λ plane where everything above the solid line is excluded at 95% C.L. The dotted line corresponds to the coupling $\lambda = 1$.*

Chapter 6

Conclusion

Data recorded with the ALEPH detector at LEP center-of-mass energies of 161 GeV and 172 GeV show no signs of new physics in the single and multi-photon events. The cross sections for $e^+e^\perp \to \nu\bar{\nu}\gamma(\gamma)$ and $e^+e^\perp \to \gamma\gamma(\gamma)$ are measured and found to be

$$\sigma(e^+e^- \to \nu\bar{\nu}\gamma(\gamma)) = 5.2 \pm 0.8 \pm 0.2\,\text{pb} \quad \text{at} \quad \sqrt{s} = 161 \quad \text{GeV}$$

$$\sigma(e^+e^- \to \nu\bar{\nu}\gamma(\gamma)) = 4.6 \pm 0.8 \pm 0.2\,\text{pb} \quad \text{at} \quad \sqrt{s} = 172 \quad \text{GeV}$$

$$\sigma(e^+e^- \to \gamma\gamma(\gamma)) = 13.5 \pm 1.2 \pm 0.6\,\text{pb} \quad \text{at} \quad \sqrt{s} = 161 \quad \text{GeV}$$

$$\sigma(e^+e^- \to \gamma\gamma(\gamma)) = 11.8 \pm 1.2 \pm 0.5\,\text{pb} \quad \text{at} \quad \sqrt{s} = 172 \quad \text{GeV}.$$

These values are in agreement with Standard Model expectations. The respective polar angle distributions are also compared to Standard Model expectations and

found to be in good agreement.

The experimental 95% C.L. upper limits on the cross sections are derived for the following supersymmetric processes $e^+e^\perp \to \chi_2^0\chi_2^0 \to \chi_1^0\chi_1^0\gamma\gamma$, $e^+e^\perp \to \chi_1^0\chi_1^0 \to \tilde{G}\tilde{G}\gamma\gamma$, $e^+e^\perp \to \chi_2^0\chi_1^0 \to \chi_1^0\chi_1^0\gamma$ and $e^+e^\perp \to \chi_1^0\tilde{G} \to \tilde{G}\tilde{G}\gamma$. These cross section limits are actually more general and can be applied to the reactions: $e^+e^\perp \to XX \to YY\gamma\gamma$ and $e^+e^\perp \to XY \to YY\gamma$ where Y is massless or has mass. The 95% C.L. limit on the χ_1^0 mass is found to be 71 GeV/c^2 ($\tau_{\chi_1^0} \leq 3$ ns) for gravitino LSP Supersymmetry models with $M_{\tilde{e}_R} = 1.5M_{\chi_1^0}$. The excluded region of the Supersymmetry Breaking Scale as a function of neutralino mass is derived. The lower limit on the χ_1^0 (χ_2^0) mass as a function of selectron mass is determined and compared to the region compatible with the CDF event for the gravitino (neutralino) LSP scenario.

Possible deviations from QED have been parameterized in the context of compositeness models. A fundamental parameter in these models is the cut-off energy scale Λ, which gives the minimum energy 'to see' a preon (the supposed sub-component of the 'fundamental particles'). The lower limits on this energy scale for electron compositeness are derived and found to be 217.5 GeV for Λ_+ and 182.9 GeV for $\Lambda_\perp$ at 95% C.L. Using the de Broglie relation these correspond to the 95% C.L. upper limit on the radius of the 'preons' of $r_+ < 5.7 \times 10^{\perp 18}$ m and $r_\perp < 6.8 \times 10^{\perp 18}$ m. Another possible consequence of compositeness is the existence of electron excited states. The effect of excited electron exchange depends on both the mass and the coupling constant. In the simplest case of $\lambda = 1$ (for magnetic coupling constant $\frac{e\lambda}{2M_{e^*}^*}$), the mass of the e^* is excluded below 208.4 GeV/c^2 at 95% C.L.

Experiment	$M_{\chi_1^0}$ (GeV)	Λ_+ (GeV)	$\Lambda_\perp$ (GeV)	M_{e^*} (GeV)
ALEPH	71	218	183	208
OPAL	61	195	210	194
L3	65	207	205	210
Previous ALEPH	-	173	150	162

Table 6.1: *A comparison of upper limits at 95% C.L. is given for the LEP experiments (DELPHI has not published limits). The data sample is that taken in the summer of 1996. The luminosity for the other two experiments is about equal to that taken by ALEPH. The mass limit on* χ_1^0 *is for the gravitino LSP scenario and for* $M_{\tilde{e}_R} = 1.5 M_{\chi_1^0}$ *and* $\tau_{\chi_1^0} \leq 3\,\mathrm{ns}$.

Many of the searches described in this document were also performed by the other experiments at LEP [34, 59]. Table 6.1 shows a comparison of the limits obtained by the other experiments, as well as the ALEPH results from the LEP data taken at the Z peak. A condensed version of Chapters 3 and 4 is published in Physics Letters [60].

Appendix A

The LEP Supersymmetry Working Group

Each LEP experiment has studied the production of acoplanar-photon events at LEP2 energies. No anomaly with respect to Standard Model predictions has been observed. In this section the data from the four experiments is combined and the upper limit on the $e^+e^\perp \to \chi_1^0\chi_1^0 \to \tilde{G}\tilde{G}\gamma\gamma$ process is derived. The constraint that the combined results place on the CDF Region is a significant improvement over the ALEPH results alone.

The upper limit on the cross section for $e^+e^\perp \to \chi_1^0\chi_1^0 \to \tilde{G}\tilde{G}\gamma\gamma$ is found by combining the four experiments and the different centre-of-mass energies using the multi-channel Bayesian method [61]. The multi-channel method is used for the combination because the four LEP experiments have varying degrees of sensitivity (i.e. efficiency and luminosity) to the signal process. The cross section limits are valid

for $\sqrt{s} = 172\,\mathrm{GeV}$. The effective luminosities at center-of-mass energies below 172 GeV are scaled according to the cross section for $e^+e^\perp \to \chi_1^0\chi_1^0$, where the neutralino is pure B-ino in composition. In $e^+e^\perp$ collisions the production of neutralinos would proceed via t-channel selectron exchange. Right-selectron exchange dominates over left-selectron exchange. Therefore the scaling is done for two choices of right-selectron mass, $M_{\tilde{e}_R} = 1.5M_{\chi_1^0}$ and $M_{\tilde{e}_R} = M_{\chi_1^0}$. The upper limit on the cross section is not strongly dependent on the above choices. Scaling the luminosity by the threshold dependence β^3/s changes the cross section limit by less than 5%.

In Figure A.1 the combined LEP limit is compared to two gravitino LSP models, Gauge-Mediated SUSY Breaking (GMSB) and the so-called ' No-Scale Super Gravity' (LNZ model). For GMSB two values for the right-selectron mass, $M_{\tilde{e}_R} = 1.5M_{\chi_1^0}$ and $M_{\tilde{e}_R} = M_{\chi_1^0}$, are plotted. In the LNZ model the right-selectron mass is tied to the neutralino mass, but is generally about $M_{\tilde{e}_R} = 1.5M_{\chi_1^0}$.

In order to define an exclusion region in the $M_{\tilde{e}_R}, M_{\chi_1^0}$ plane the theoretical cross section for $e^+e^\perp \to \chi_1^0\chi_1^0$ is calculated at each $M_{\tilde{e}_R}$, $M_{\chi_1^0}$ mass point for right-selectron masses ranging from 70 GeV/c^2 to 180 GeV/c^2 and neutralino masses ranging from 30 GeV/c^2 to 86 GeV/c^2 and compared to the combined LEP limit to obtain the excluded region.

The neutralino mass limits were also checked for various left-selectron masses. The result is found to be robust at the ± 1 GeV/c^2 level for left-selectron masses ranging from $M_{\tilde{e}_L} = M_{\tilde{e}_R}$ to $M_{\tilde{e}_L} >> M_{\tilde{e}_R}$.

The excluded region in the neutralino, right-selectron mass plane is shown in

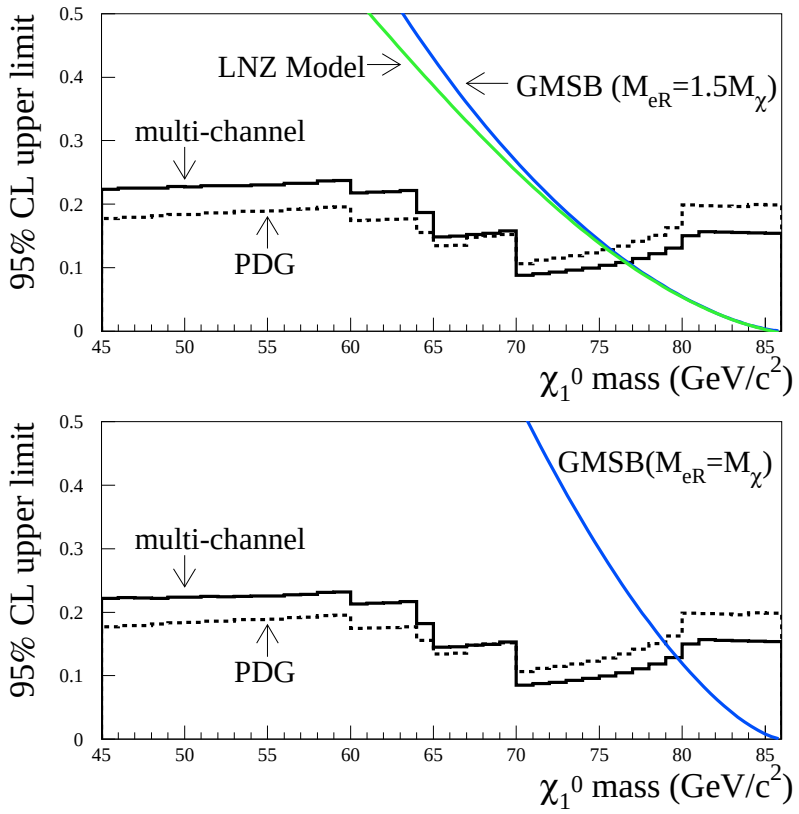

Figure A.1: The upper limits on the cross section for the process $e^+e^\perp \to \chi_1^0\chi_1^0$ derived from the combined LEP data. The limits are valid for $\sqrt{s} = 172\,\mathrm{GeV}$, pure B-ino neutralino composition and negligible neutralino lifetime. The data has been combined using the Bayesian multi-channel method. The one-channel combination is also shown (dotted histogram) and labeled PDG for comparison.

Figure A.2. Overlayed is the 'CDF region', corresponding to the region in which the properties of the CDF $ee\gamma\gamma + E^T_{MISS}$ event are compatible with the process $q\bar{q} \to \tilde{e}\tilde{e} \to ee\chi^0_1\chi^0_1 \to ee\tilde{G}\tilde{G}\gamma\gamma$. Three quarters of the CDF region is already excluded at 95% C.L. by the combined results.

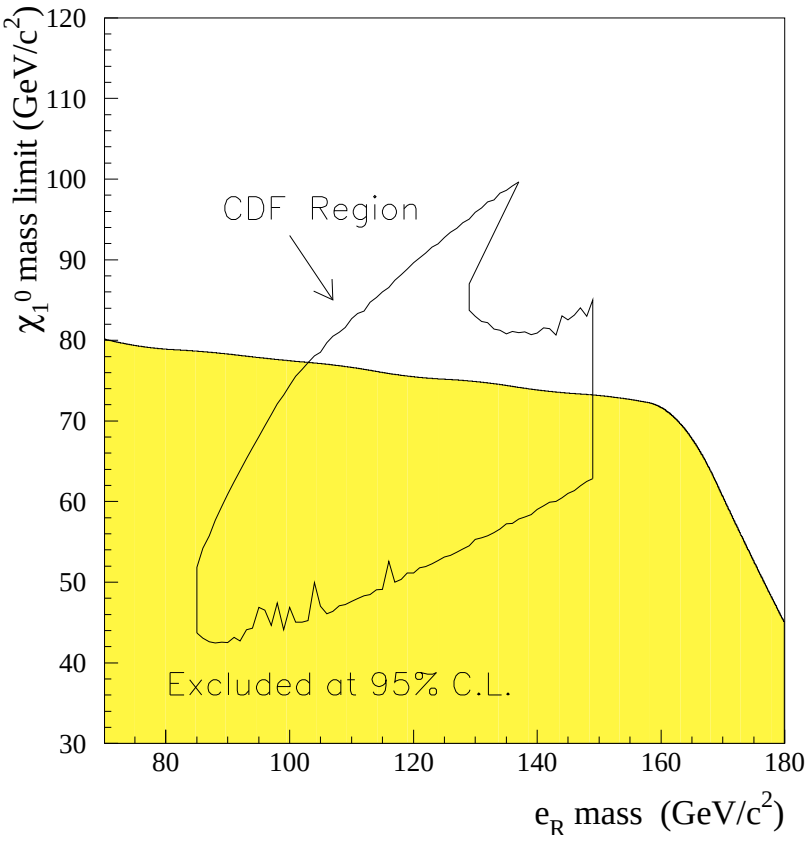

Figure A.2: The indicated CDF region determined from the properties of the CDF event assuming the reaction $q\bar{q} \to \tilde{e}\tilde{e} \to ee\chi_1^0\chi_1^0 \to ee\tilde{G}\tilde{G}\gamma\gamma$; the region has been cutoff (vertical line) where the prediction rate becomes uninterestingly small. Overlayed is the excluded mass region at 95% C.L. for a pure bino neutralino (hatched area).

Bibliography

[1] S. Weinberg, *Gravitation and Cosmology*, John Wiley and Sons (1972).

[2] G. Börner, *The Early Universe: Facts and Fiction*, Springer-Verlag (1988).

[3] S. Weinberg, *Scientific American*, June, 1981.

[4] J.F. Gunion, *et al.*, *The Higgs Hunter's Guide* (Addison-Westley, Redwood City, CA, 1990).

[5] H.P. Nilles, Phys. Reports **110**, (1984) 1.

[6] P. Nath, *et al. Applied N = 1 Supergravity* (World Scientific, Singapore, 1984).

[7] S. Weinberg, Phys. Rev. Lett. **19**, (1967) 1264;

A. Salam, in "Elementary Particle Theory", W. Svartholm, ed., Almquist and Wiksell, Stockholm (1968);

S.L. Glashow, *et al.*, Phys. Rev. **D2**, (1970) 1285.

[8] E. Ma and J. Okada, Phys. Rev. Lett. **41**, (1978) 287.

[9] H.E. Haber and G.L. Kane, Phys. Reports **117**, (1985) 75.

[10] JADE Collaboration, Phys. Lett. **139B** (1984) 327;

CELLO Collaboration, Z. Phys. **C35** (1987) 181;

VENUS Collaboration, Z. Phys **C45** (1989) 175;

ALEPH Collaboration, Phys. Lett. **B384** (1996) 333;

DELPHI Collaboration, Phys. Lett. **B380** (1996) 471;

L3 Collaboration, Phys. Lett. **B384** (1996) 323;

OPAL Collaboration, Phys. Lett. **B377** (1996) 222.

[11] S. Katsanevas and S. Melachroinos, in *Physics at LEP2*, Eds. G. Altarelli, T. Sjöstrand, F. Zwirner, CERN Report 96-01, Volume 1 (1996);

ALEPH Collaboration, Phys. Reports **216**, (1992) 253.

[12] S. Ambrosanio, *et al.*, Phys. Rev. **D55** (1997) 1372-1398.

[13] J. Ellis and J.S. Hagelin, Phys. Lett. **122B** (1983) 303.

[14] H. Haber and D. Wyler, Nuclear Physics **B323** (1989) 267.

[15] P. Fayet, Phys. Lett. **B69** (1977) 489;

P. Fayet, Phys. Lett. **B70** (1977) 461.

[16] M. Dine, W.Fischler, and M. Srednichi, Nucl. Phys. **B189** (1981) 575.

[17] M. Dine, *et al.*, Phys. Rev. **D51** (1995).

[18] S. Dimopoulos, M. Dine, S. Raby and S. Thomas, Phys. Rev. Lett. **76** (1996) 3494-3497.

[19] S. Dimopoulos, S. Thomas and J. D. Wells, Nucl. Phys. **B488** (1997) 39.

[20] G.F. Guidice and R. Rattazzi, CERN-TH/97-380, hep-ph/9801271.

[21] private communication, Scott Thomas.

[22] J. Lopez, *et al.*, Phys. Rev. Lett. **77** (1996) 5168.

[23] J. Lopez and D. Nanopoulos, Phys. Rev. **D55** (1997) 4450.

[24] J. Lopez and D. Nanopoulos, Phys. Rev. **D55** (1997) 5813.

[25] J. Lopez, hep-ph/9601208.

[26] P. Fayet, Phys. Lett. **B175** (1986) 471.

[27] S. Park, in Proceedings of the 10th Topical Workshop on Proton-Antiproton Collider Physics, Fermilab, 1995, edited by R. Raja and J.Yoh (AIP,New York,1995),p 62.

[28] CDF Collaboration, hep-ex/9801019.

[29] Anomalous effects in $e^+e^\perp$ annihilation into boson pairs, II. $e^+e^\perp \to ZZ, \gamma Z, \gamma\gamma$, P. Mery, M. Perrotttet, and F. Renard, Zeitschrift fur Physik **C38** (1988) 579.

[30] A. Litke, Experiments with electron-positron colliding beams, Ph.D. Thesis, Harvard University (1970).

[31] ALEPH Collaboration, Zeitschrift für Physik **C59** (1993) 215.

[32] F.E. Low, Phys. Rev. Lett. **14** (1965) 238.

[33] PLUTO Collaboration, Phys. Lett. **B59** (1980) 87;

JADE Collaboration, Z. Phys. **C19** (1983) 197;

MARKJ Collaboration, Phys. Rev. Lett. **53** (1984) 134;

TASSO Collaboration, Z. Phys. **C26** (1984) 337;

CELLO Collaboration, Phys. Lett. **B168** (1986) 420;

HRS Collaboration, Phys. Rev. **D34** (1986) 3286;

MAC Collaboration, Phys. Rev. **D35** (1987) 1;

VENUS Collaboration, Phys. Z. **C45** (1989) 175;

TOPAZ Collaboration, Phys. Lett. **B284** (1992) 144;

DELPHI Collaboration, Phys. Lett. **B327** (1994) 386;

ALEPH Collaboration, Phys. Lett. **B384** (1996) 333.

[34] L3 Collaboration, Phys. Lett. **B413** (1997) 159;

OPAL Collaboration, Eur. Phys. J. **C1** (1998) 21.

[35] S. Myers; " LEP Status and Plans", Proceedings of the U.S. particle Accelerator Conference and the 16th International Conference on High Energy Accelerators, Dallas USA (1995).

[36] S. Myers; " LEP2: Present and Future Performance and Limitations", CERN, Geneva, Switzerland (1997)

[37] B. Zotter: CERN-SL 92-29 p193.

[38] D. Brandt: CERN SL/94-06(DI) (1994) 149.

[39] ALEPH Collaboration, Nucl. Instrum. Methods **A360** (1995) 481.

[40] J.C. Brient, S. Orteu, A. Rouge, and M. Verderi, 'A Method for Photon Reconstruction', ALEPH 93-107, PHYSICS 93-88.

[41] ALEPH Collaboration, Nucl. Instrum. Methods **A294** (1990) 121.

[42] M. McNeil, *Search for B_c and Υ in Hadronic Z Decays*, UC Santa Cruz, (1996).

[43] S. Jadach, B.F.L. Ward, and Z. Was, Comp. Phys. Commun. **79** (1994) 503.

[44] R. Miquel, C.Mana and M. Martinez, Z. Phys. **C48** (1990) 309.

[45] E. Boss et al., hep-ph/9503280.

[46] DELPHI Collaboration, Proceedings of HEP'97 Conference, Jerusalem, 1997.

[47] F.A. Berends and R. Kleiss, Nucl. Phys. **B186** (1981) 22.

[48] ALEPH internal note ALEPH 96-064, unpublished;
L.M. Elisabetta Barberio, *A study of the reaction* $e^+e^\perp \to \gamma\gamma(\gamma)$ *at the LEP storage rang with the ALEPH detector*, Siegen, (1993).

[49] H. Anlauf *et al.*, Comp. Phys. Commun. **79** (1994) 466.

[50] S. Jadach, W. Placzek, and B. F. L. Ward, preprint The University of Tennessee UTHEP-95-1001 (unpublished).

[51] S. Katsanevas and S. Melachroinos, in *Physics at LEP2*, Eds. G. Altarelli, T. Sjöstrand, F. Zwirner, CERN Report 96-01, Volume 2 (1996) 328.

[52] T. Bayes, *An essay towards solving a problem in the doctrine of chances*, Philosophical Transactions of the Royal Society, 53 (1763) 370. Reprinted in Biometrika, 45 (1958) 159.

[53] Glen D. Cowan, Statistical Data Analysis in Particle Physics, to be published by Oxford University Press.

[54] V. Innocente and L. Lista, Nucl. Instrum. Methods **A340** (1994) 396.

[55] R. D. Cousins, V. L. Highland, Nucl. Instrum. Methods **A320** (1992) 331.

[56] ALEPH Collaboration, Phys. Lett. **B384** (1996) 427.

[57] Gian Giudice, CERN Theory seminar, CERN 1996.

[58] ALEPH collaboration, CERN-PPE/98-022, submitted to Eur. Phys. J. **C**.

[59] L3 Collaboration, Phys. Lett. **B415** (1997) 299;
DELPHI Collaboration, Phys. J. **C1** (1998) 1;
OPAL Collaboration, CERN-PPE/97-132, submitted to Z. Phys. C.

[60] ALEPH Collaboration, Phys. Lett. **B420** (1998) 127.

[61] V. F. Obraztsov, Nucl. Instr. and Meth. **316** (1992) 388.